

Structures of Bimetallic Nanoparticles and the Effect of Adsorption: a DFT Study

by

PAUL STEPHEN WEST



A thesis submitted to
The University of Birmingham
for the examination of
DOCTOR OF PHILOSOPHY

School of Chemistry
College of Engineering and Physical Sciences
University of Birmingham
March 2012

UNIVERSITY OF
BIRMINGHAM

University of Birmingham Research Archive

e-theses repository

This unpublished thesis/dissertation is copyright of the author and/or third parties. The intellectual property rights of the author or third parties in respect of this work are as defined by The Copyright Designs and Patents Act 1988 or as modified by any successor legislation.

Any use made of information contained in this thesis/dissertation must be in accordance with that legislation and must be properly acknowledged. Further distribution or reproduction in any format is prohibited without the permission of the copyright holder.

Abstract

This thesis is focused on the study of bimetallic nanoparticles, their structure and evolution as small molecules and reactive species interact with them. Initially we describe Density Functional Theory (DFT), which will be used to find the energies of the nanoparticles and other properties with reasonable computational efficiency.

Chapter three focuses on the structural properties of RhPd nanoparticles, including a search of low energy isomers. This is too expensive to be performed at the DFT level, so the Gupta potential was used along with the Birmingham Cluster Genetic Algorithm (BCGA) and Basin Hopping algorithm to conduct the search.

Studies were performed on small gold, palladium and gold-palladium bimetallic clusters, with CO adsorption also investigated to see how the structure of the cluster was affected by CO adsorption. This work was then expanded to larger clusters. The 38 atom Truncated Octahedron (TO) was used as a model system to research how CO molecules, atomic hydrogen and atomic oxygen effected the structure of bimetallic nanoparticles. Four separate bimetallic systems were studied: RhPd, PdPt, CuPt and AuPd. The last part of this thesis focuses on AuPt with an emphasis on charge effects and the energy of the d-band.

Call on me in prayer and I will answer you. I will show you great and mysterious things you did not know before.

Jeremiah 33:3 (NET)

Acknowledgements

There are many people I would like to thank for making this thesis possible. First and foremost is my supervisor Professor Roy Johnston, for his help, support, near-infinite patience and the most certainly infinite supply of red ink to correct the various papers and drafts of this thesis. I would also like to thank my second supervisor Melanie Britton, for the occasional push when it was required. My Ph.D. would not have been nearly as fun without the members of the Johnston group, past and present, for the good time and for making life bearable though the harder periods. Oliver Paz-Borbon deserves a special mention for teaching the various programs and explaining the basics that I should have known about in my undergraduate years. In addition, I would also thank Andy Bennett, Paul Jennings, Ramli Ismail, Andy Logsdail, Chris Heard, Mark Oakley and Lewis Smeeton. Visiting students and project students have also taught me that you do learn stuff during a Ph.D. and don't remain a mindless code monkey, so thanks also to Michael, Joe, Samara, Louise, Alina, Josephat and Ali. Special thanks to Sven Heiles who helped with some of the more complex topics on density functional theory and his wisdom was appreciated.

Some of this work was performed in Italy under the guidance of Professor Alessandro Fortunelli and Giovanni Barcaro. I would also like to thank the members of Alessandro's group out there- Lucca, Iori, Fabio and Ilaria for enjoyable times in Pisa.

This work could not have been achieved without funding and computer time. Special thanks go to the Engineering and Physical Science Research Council (EPSRC) and the University of Birmingham for my Ph.D. scholarship. Also to HPC-Europa2 for funding trips to Italy and for funding to attend a lovely conference in Helsinki. Additional thanks go to CECAM and to the COST nanoalloys framework for funding to attend conferences in Lausanne and Barcelona, respectively.

Computational time has been provided by the University of Birmingham's BlueBEAR machine, and I am very grateful for the support of Paul Hatton and the rest of the team for help fixing various programs when our group slowed the machine down to a crawl. Other CPU time was provided through the HPC-Europa2 grant and the HECTOR Materials Chemistry Consortium.

I would like to thank my parents, Richard and Anne West, for their support in my Ph.D., along with my brother Mark and my loving girlfriend Catherine. Finally I would like to thank all the people at Selly Oak Elim Church for their prayers and support.

This thesis and the work described in it are entirely my own, except where I have acknowledged either help from a named person or a reference is given to a published source or a thesis. Text taken from another source will be enclosed in quotation marks and a reference will be given.

Contents

Chapter 1-	Introduction.....	1
1.1	History	1
1.2	Bimetallic Nanoparticles.....	3
1.3	Synthesis of Nanoparticles.....	4
1.3.1	Molecular Beams	5
1.3.2	Colloidal methods.....	5
1.4	Uses of Nanoparticles	6
Chapter 2-	Density Functional Theory	7
2.1	Basic Quantum Mechanics	7
2.1.1	Variational principle	9
2.1.2	Limits of ‘true’ quantum mechanical methods	10
2.2	Density Functional Theory (DFT)	11
2.2.1	Early Attempts- The Thomas-Fermi Model	11
2.2.2	The Hohenberg-Kohn Theorems	12
2.2.3	The Kohn-Sham Equations.....	14
2.2.4	Basis Sets.....	16
2.2.5	Solving the Kohn Sham Equations.....	18
2.2.6	Effective Core Potentials (ECP’s)	20
2.3	The Exchange Correlation Function	21
2.3.1	The LDA and LSDA.....	21
2.3.2	GGAs	22
2.3.3	Hybrid functionals	23
2.4	Relativistic DFT (RDFT).....	23
2.5	DFT Programs.....	25
2.5.1	Quantum Espresso	25
2.5.2	NWChem.....	26
2.6	Conclusions.....	27
Chapter 3-	The Structure of RhPd Nanoparticles	28
3.1	Introduction.....	28
3.1.1	Rhodium and Palladium Nanoparticles	28
3.1.2	Rhodium-Palladium Bimetallic Nanoparticles	29

3.2	Searching the Potential Energy (PES) Landscape	29
3.2.1	The Gupta Potential	29
3.2.2	Genetic Algorithm	30
3.2.3	Basin Hopping	31
3.2.4	High Symmetry Searches	32
3.3	Methodology	33
3.3.1	Potentials	33
3.3.2	Genetic Algorithm	35
3.3.3	Basin Hopping	36
3.3.4	DFT Calculations	36
3.3.5	Energy Analysis	37
3.4	Results	38
3.4.1	34 Atom Clusters	38
3.4.2	38 Atom Clusters	40
3.4.3	55 Atom Clusters	43
3.4.4	98 Atom clusters	45
3.5	Conclusions	50
Chapter 4-	Chemisorption on Bimetallic Nanoparticles	52
4.1	Introduction	52
4.2	Methodology	53
4.2.1	Cluster Geometry	53
4.2.2	Adsorption structures	55
4.2.3	DFT Calculations	57
4.2.4	Energy calculations	58
4.3	Results	59
4.3.1	Bare clusters	59
4.3.2	Clusters Bound To Single H, CO and O Ligands	63
4.3.3	Multiple Adsorption	69
4.3.4	AuPd	69
4.3.5	PdPt	71
4.3.6	CuPt	72
4.3.7	RhPd	75
4.3.8	Summary- Multiple Adsorption	75
4.4	Conclusions	76
Chapter 5-	Structure and CO Adsorption of Small AuPd Clusters	78
5.1	Introduction	78

5.1.1	Previous work on small gold, palladium and AuPd clusters	79
5.2	Methodology	81
5.2.1	Structures	81
5.2.2	DFT Calculations	84
5.2.3	Calculations	84
5.3	Results	85
5.3.1	Bare Clusters	85
5.3.2	CO bound clusters	89
5.4	Conclusions and Future Work	93
5.5	Appendix- Relative Energies and Vibration Frequencies	95
5.5.1	Dimers	95
5.5.2	Trimers	97
5.5.3	Tetramers	101
Chapter 6-	The Electronic Structure of AuPt Clusters	105
6.1	Introduction	105
6.1.1	Electron Shell Closure in Gold	107
6.2	Methodology	107
6.3	Results	109
6.3.1	Bare Clusters	109
6.4	Conclusions and Future Work	114
Chapter 7-	Future Work	116
References	119

List of Figures

Figure 1-1 Schematic representation of some of the different mixing patterns available for bimetallic nanoparticles. Top row from left: a segregated nanoparticle, a ball and cup arrangement and a core-shell nanoparticle. Bottom row from left: a mixed nanoparticle with random ordering, known as a solid solution, a nanoparticle with ordered mixing, and a layered onion structure with alternating atomic layers from the center of the cluster. Based on figure 1 in reference (1).....	3
Figure 3-1 (Left) The different symmetry equivalent sites for the 38 atom TO cluster. Core sites are shown in red, and surface and vertex sites are shown in yellow and blue, respectively. The 98 atom Leary Tetrahedron, with each symmetry equivalent site shown in a different colour.	33
Figure 3-2 The different structures found for 34 atom RhPd clusters for each of the three potentials. Different colours denote the different structures. Yellow- decahedra, magenta- icosahedra, cyan- face centered cubic- hexagonal closed pack (FCC-HCP), green- decahedral- icosahedral mixed structure (Dh-Ih) and red- C3 tetrahedra.	38
Figure 3-3 The different structures found by the BCGA for the 34 atom clusters. Borders indicate the colours in the composition diagram (figure 3-2). From left: C3 Tetrahedra, Decahedra, decahedra-icosaahedra (Dh-Ih), FCC-hcp structure, icosahedra.....	38
Figure 3-4 (Left) The excess energy of the three different potentials for the 34 atom structures across the composition range from pure Palladium (left) to pure Rhodium (right). (Right) the second difference energy of the three different potentials across the composition range.	39
Figure 3-5 The different structures found for 38 atom RhPd clusters for each of the three potentials. Different colours denote the different structures. Yellow- Truncated Octahedron (TO), red- decahedral-icosahedral mixed structure (Dh-Ih), green- icosahedra and cyan- deahedra.....	40
Figure 3-6 (Left) The excess energy of the three different potentials for the 38 atom structures across the composition range. (Right) the second difference energies of the three different potentials across the composition range.	41
Figure 3-7 (Left) Difference between Ex for each potential and DFT calculations. (Right) Difference between Eb for each potential and the DFT calculations.	42
Figure 3-8 Different structures across the composition range for the 55 atom clusters for each	

potential, with colour's referring to different structures. Green- icosahedra, red- FCC-HCP, yellow- FCC fragment (FCC), blue- decahedra, cyan- poly-decahedra, pink FCC/HCP/icosahedral mixed cluster and grey poly-icosahedra.	43
Figure 3-9 Variation in energy of the 55 atom clusters across the composition range. Left- excess energy, right- second difference energy.	44
Figure 3-10 Structures corresponding to minima for the second difference energy with the geometric potential (figure 3-9).....	45
Figure 3-11 Different structures across the composition range for the 98 atom clusters for each potential, found using the Genetic Algorithm. Yellow- decahedra, magenta- icosahedra, cyan- FCC, blue- FCC-HCP, light green- Leary Tetrahedra (LT) and dark green- incomplete tetrahedral.	45
Figure 3-12 Excess energies of the structures generated with the GA (solid lines) compared with the all high symmetry LT structures. Each colour corresponds to a different potential. ...	46
Figure 3-13 The five structures used for the BH algorithm. From left to right: Decahedra (1), Decahedra (2), FCC, icosahedra, leary tetrahedra.....	47
Figure 3-14 Different structures across the composition range for the 98 atom clusters for each potential, found using the basin hopping algorithm. Blue- pure clusters (FCC for Pd ₉₈ and LT for Rh ₉₈), cyan- FCC, magenta- icosahedra, yellow- decahedra and green LT.....	47
Figure 3-15 Different structures across the composition range for the 98 atom clusters for each potential, using symmetry searches, basin hopping and the genetic algorithm. Yellow- decahedra, magenta- icosahedra, cyan- FCC, blue- FCC-HCP, light green- Leary Tetrahedra (LT) and dark green- incomplete tetrahedral.	49
Figure 3-16 The excess energies for the lowest energy structures of the 98 atom clusters for all three potentials, using the lowest energy structure from the BCGA, BH and symmetry search methods.....	50
Figure 4-1 (Top) the three different structures studied. From left to right- core, centroid (cent) and hex. (Bottom) The eight centroid sites make up a cube, and the three different homotops of these structures are shown. The symmetry point group of the respective cubes are given in brackets.....	53
Figure 4-2 Adsorption sites studied in this work, with carbon and oxygen shown in black and red, respectively. Atomic hydrogen and oxygen are adsorbed to the same sites. The point group of each cluster is shown in brackets.	56

Figure 4-3 the adsorption sites studied for the multiple ligand clusters, with the point group for each structure shown in brackets.	57
Figure 4-4 A diagram showing how the relative energies were calculated for the multiple adsorption clusters. The left hand diagram shows the relative energies, as calculated using equation 4-1, of different homotops with different numbers of ligands (x axis) on them. A straight line is fitted to the core-shell structure (thin black line fitted to the red line). All the points are then shifted relative to this line, resulting in the diagram on the right.	59
Figure 4-5 Relative energies in eV of different homotops for the bare A_6B_{32} and B_6A_{32} clusters. Gray lines separate different bimetallic compositions.	60
Figure 4-6 Relative energies of Au_6Pd_{32} (left) and Pd_6Au_{32} (right) clusters with and without ligands. The far left and right columns show the relative energies of the bare Au_6Pd_{32} and Pd_6Au_{32} clusters, respectively. The 6 central columns show the relative energies of the cluster with (from centre) H, CO and O ligands bound to it. The Au_6Pd_{32} “Cent Au” energy is not shown, as this structure was not a local minima.	64
Figure 4-7 Relative energies of Pd_6Pt_{32} (left) and Pt_6Pd_{32} (right) clusters with and without ligands. The far left and right columns show the relative energies of the bare Pd_6Pt_{32} and Pd_6Au_{32} clusters, respectively. The 6 central columns show the relative energies of the cluster with (from centre) H, CO and O ligands bound to it.	65
Figure 4-8 Relative energies of Cu_6Pt_{32} (left) and Pt_6Cu_{32} (right) clusters with and without ligands. The far left and right columns show the relative energies of the bare Cu_6Pt_{32} and Pt_6Cu_{32} clusters, respectively. The 6 central columns show the relative energies of the cluster with (from centre) H, CO and O ligands bound to it.	66
Figure 4-9 Relative energies of Rh_6Pd_{32} (left) and Pd_6Rh_{32} (right) clusters with and without ligands. The far left and right columns show the relative energies of the bare Rh_6Pd_{32} and Pd_6Rh_{32} clusters, respectively. The 6 central columns show the relative energies of the cluster with (from centre) H, CO and O ligands bound to it.	68
Figure 4-10 Relative energies of multiple CO molecules on (left) Au_6Pd_{32} and (right) Pd_6Au_{32} clusters. X denotes the number of CO molecules bound to the cluster.	69
Figure 4-11 Relative energies of multiple H atoms on (left) Au_6Pd_{32} and (right) Pd_6Au_{32} clusters. X denotes the number of H atoms on the cluster	70
Figure 4-12 Relative energies of multiple CO molecules on (left) Pd_6Pt_{32} and (right) Pt_6Pd_{32} clusters. X denotes the number of CO molecules on the cluster.	71

Figure 4-13 Relative energies of multiple H atoms bound to (left) $\text{Pd}_6\text{Pt}_{32}$ and (right) $\text{Pt}_6\text{Pd}_{32}$ clusters. X denotes the number of H atoms on the cluster.....	72
Figure 4-14 Relative energies of multiple CO molecules on (left) $\text{Cu}_6\text{Pt}_{32}$ and (right) $\text{Pt}_6\text{Cu}_{32}$ clusters. X denotes the number of CO molecules on the cluster.	73
Figure 4-15 Relative energies of multiple H ligands on (left) $\text{Cu}_6\text{Pt}_{32}$ and (right) $\text{Pt}_6\text{Cu}_{32}$ clusters. X denotes the number of atoms on the cluster.....	74
Figure 4-16 Relative energies of multiple CO ligands on (left) $\text{Rh}_6\text{Pd}_{32}$ and (right) $\text{Pd}_6\text{Rh}_{32}$ clusters. X denotes the number of ligands on the cluster.....	75
Figure 5-1 Experimental setup for studying small gas phase clusters. Based on the design in (19). A Nd:YAG laser beam atomises metal atoms from a target, which are then trapped inside a noble gas liquid deposited onto a CsI plate.	79
Figure 5-2 Initial geometries of the bare (a) three atom clusters and (b) four atom clusters. ..	82
Figure 5-3 Initial geometries of (a) dimers (b) trimers and (c) tetramers of PdAu clusters, all with CO. Colour refer to metal (Au or Pd) blue, carbon black and oxygen red.....	83
Figure 5-4 Binding energies of the 3 atom AuPd clusters. In the key, 'L' refers to the low-spin (doublet for Au_3 and Au_1Pd_2 , singlet for Pd_3 and Au_2Pd_1) clusters whereas 'M' refers to mid-spin clusters (triplet state for Au_2Pd_1 and Pd_3 , quartet state for Au_3 and Au_1Pd_2). Structural labels are lin- linear and tri- triangle.	86
Figure 5-5 Binding energies of the 4 atom AuPd clusters. In the key, 'L' refers to the low-spin clusters whereas 'M' refers to mid-spin clusters. Structural labels are: lin-linear, rom-rhombus, tetra- tetrahedral and tri- triangle with an ad-atom.....	88
Figure 5-6 The relative energies of the pure clusters, and the structure of each. Left- Au_3CO . Right- Pd_3CO	90
Figure 5-7 relative energies of the 3 atom bimetallic clusters and their structures. Left- Pd_2Au_1 . Right Au_2Pd_1	91
Figure 5-8 Low energy structures for (A) Au_4CO and (B) Pd_4CO with their relative energies (in eV). Energies shown in blue indicate a singlet state structure, whereas an energy in red indicates the structure has a doublet spin state. Atom colours are: yellow- gold, blue- palladium, cyan- carbon and red- oxygen.	92
Figure 5-9 Low energy structures for (A) $\text{Au}_1\text{Pd}_3\text{CO}$, (B) $\text{Au}_2\text{Pd}_2\text{CO}$ and (C) $\text{Au}_3\text{Pd}_1\text{CO}$ with their relative energies (in eV). The same colour scheme is used to that in figure 5-8.	93
Figure 6-1 The homotops studied for the $\text{Au}_{34}\text{Pt}_4$ clusters. Platinum atoms are shown in dark	

red, gold in yellow. These clusters are similar to those studied in Chapter 4- .	108
Figure 6-2 Excess energies (in eV) of the bare AuPt clusters for different compositions and homotops. Left- PBE functional, Right- PW91 functional.	109
Figure 6-3 Löwdin charges on each atom relative to the gas phase atom. the orientation of each cluster is given in the bottom left of each picture, with dark red atoms for platinum and yellow for gold atoms. For the top row the PBE functional was used, and the bottom row shows the charges found using the PW91 XC functional.	111
Figure 6-4 Graphs showing the bond distance R and the orbital occupations for Au ₅₅ , Pt ₅₅ , AuPt ₅₄ and PtAu ₅₄ . The FEFF8 data was taken from reference (177).	113

List of Tables

Table 3-1 The parameters for the three different potentials. The pure “Arith” and “Geomt” potentials are both from reference (115), with the bimetallic coefficients calculated using the arithmetic and geometric means, respectively. The “DFT-fit” coefficients are derived from bulk DFT calculations on FCC Rh and Pd for the monometallic potentials, and Rh ₁ Pd ₃ , Rh ₂ Pd ₂ and Rh ₃ Pd ₁ FCC bulk alloys for the Rh-Pd coefficients.....	35
Table 4-1 The number of nearest neighbour bonds for each structure, for each cluster, with a composition of A ₆ B ₃₂	62
Table 4-2 The adsorption energies (in eV) of CO, atomic H and O on the atop site of the centroid atom for each 38 atom cluster. Cu ₃₈ BSSE shows the Basis Set Superposition Error (BSSE) for O, CO and H basis sets a copper cluster.	63
Table 5-1 The vibration frequencies (cm ⁻¹), bond lengths (Å) and binding energies (in eV) of Au ₂ , Pd ₂ and Au ₁ Pd ₁ at different spin states.	85
Table 5-2 Relative energies (in eV) and vibration frequencies (in cm ⁻¹) for different stable structures of Au ₂ CO. Gold atoms are shown in yellow, carbon in cyan and oxygen in red.	95
Table 5-3 Relative energies (in eV) and vibration frequencies (in cm ⁻¹) for the different stable structures of Pd ₂ CO. Palladium atoms are shown in dark blue, carbon in cyan and oxygen in red.	95
Table 5-4 Relative energies (in eV) and vibration frequencies (in cm ⁻¹) for the different stable structures of Au ₁ Pd ₁ CO. Gold atoms are shown in yellow, palladium in dark blue, carbon in cyan and oxygen in red.	96
Table 5-5 Relative energies (in eV) and vibration frequencies (in cm ⁻¹) for the different stable structures of Au ₃ CO. Gold atoms are shown in yellow, carbon in cyan and oxygen in red.	97
Table 5-6 Relative energies (in eV) and vibration frequencies (in cm ⁻¹) for the different stable structures of Pd ₃ CO. Palladium atoms are shown in dark blue, carbon in cyan and oxygen in red.	98
Table 5-7 Relative energies (in eV) and vibration frequencies (in cm ⁻¹) for the different stable structures of Au ₁ Pd ₂ CO. Gold atoms are shown in yellow, palladium in dark blue, carbon in cyan and oxygen in red.	99
Table 5-8 Relative energies (in eV) and vibration frequencies (in cm ⁻¹) for the different stable structures of Au ₂ Pd ₁ CO. Gold atoms are shown in yellow, palladium in dark blue, carbon in	

cyan and oxygen in red.	100
Table 5-9 Relative energies (in eV) and vibration frequencies (in cm^{-1}) of the five lowest energy structures for Au_4CO . Gold atoms are shown in yellow, carbon in cyan and oxygen in red.	101
Table 5-10 Relative energies (in eV) and vibration frequencies (in cm^{-1}) of the five lowest energy structures for Pd_4CO . Palladium atoms are shown in dark blue carbon in cyan and oxygen in red.	102
Table 5-11 Relative energies (in eV) and vibration frequencies (in cm^{-1}) of the five lowest energy structures for $\text{Au}_3\text{Pd}_1\text{CO}$. Gold atoms are shown in yellow, palladium in dark blue, carbon in cyan and oxygen in red.	103
Table 5-12 Relative energies (in eV) and vibration frequencies (in cm^{-1}) of the five lowest energy structures for $\text{Au}_2\text{Pd}_2\text{CO}$. Gold atoms are shown in yellow, palladium in dark blue, carbon in cyan and oxygen in red.	103
Table 5-13 Relative energies (in eV) and vibration frequencies (in cm^{-1}) of the five lowest energy structures for $\text{Au}_3\text{Pd}_1\text{CO}$. Gold atoms are shown in yellow, palladium in dark blue, carbon in cyan and oxygen in red.	104
Table 6-1 The band gaps around the fermi level for the $\text{Pt}_4\text{Au}_{34}$ clusters. These values are calculated from the energies of the Highest Occupied Molecular Orbital (HOMO) and the Lowest Unoccupied Molecular Orbital (LUMO).	110
Table 6-2 Löwdin charges for the three different sites on the $\text{Pt}_6\text{Au}_{32}$ core-shell cluster, using different programs, basis sets and exchange correlation functionals.	112
Table 6-3 Mulliken charges for the three different sites on the $\text{Pt}_6\text{Au}_{32}$ core-shell cluster, using different programs, basis sets and exchange correlation functionals.	112

List of Publications

Paul S. West, Roy L. Johnston, Giovanni Barcaro and Alessandro Fortunelli
The Effect of CO and H Chemisorption on the Chemical Ordering of Bimetallic Clusters, *J. Phys. Chem. C* 2010, **114**, 19678-19686

Paul S. West, Roy L. Johnston, Giovanni Barcaro and Alessandro Fortunelli
Adsorption of CO and H ligands on TO₃₈ binary Nanoalloys, *J. Phys. Chem. C* 2013, *in prep.*

Chapter 1- Introduction

Nanoparticles are aggregates of atoms or molecules, made up of a few to tens of millions of atoms or molecules with sizes varying from one to a few hundred nanometres(1). Due to their small size, they often exhibit different properties from the corresponding bulk material. Clusters are similar to nanoparticles, and the terms are often used interchangeably, although clusters can be smaller than nanoparticles(1, 2). Due to their small size, there are many different shapes of nanoparticle that can be created, enabling a fine tuning of the shape of the structure depending on the properties required. Examples of different shapes include decahedra, icosahedra, and fragments of bulk crystals or combinations of the above (1, 3, 4). Nanoparticles have a high surface to volume ratio, which is particularly useful in catalysis as most reactions happen at the surface, so only a small amount of catalyst is required, decreasing the cost. However, with this ability to change shape and size searching for the correct structure to get the desired properties becomes increasingly problematic.

1.1 History

Nanoparticles have been used for thousands of years, although their exact nature and structure has only been discovered relatively recently. Metallic nanoparticles have been found in glaze on medieval pottery(5), and nanoparticles have been discovered in ancient Egyptian makeup. Nanoparticles also provided the colour in

stain glass windows throughout the middle ages, with the nanoparticles stabilised within the glass.

All these developments were used as a recipe without knowing how the colour or effect was produced. The first scientific work on nanoparticles was published by Michael Faraday in 1857(6). He looked at gold nanoparticles suspended in a colloidal solution, and found that different colours could be produced. He predicted (correctly) that the size of the gold nanoparticles in the colloidal solution affected the colour of the solution, and that the particles were too small to see through any microscope available at the time.

The next big leap was a lecture by the physicist Richard Feynman(7), who presented a lecture entitled “there is plenty of space at the bottom”. He reasoned that if the smallest building block physicist’s could use was an atom then there was a huge gap between the length scales of what was being built and what could be possible. In addition he offered a prize to anyone who could build a motor less than “1/64 inch cube” (approximately 0.25cm^3), which was achieved one year later.

The paper which started the analysis of the catalytic properties was in 1987 (8), with Haruta studying gold nanoparticles on different surface. In the bulk, gold is well known to be the most noble metal. However, as the size of the gold particle decreased, the activity for CO oxidation increased and had a higher turnover frequency than the best catalysts of that time. Haruta studied the nanoparticles on different oxide supports, including SiO_2 , TiO_2 , which also affected the activity of the catalyst.

1.2 Bimetallic Nanoparticles

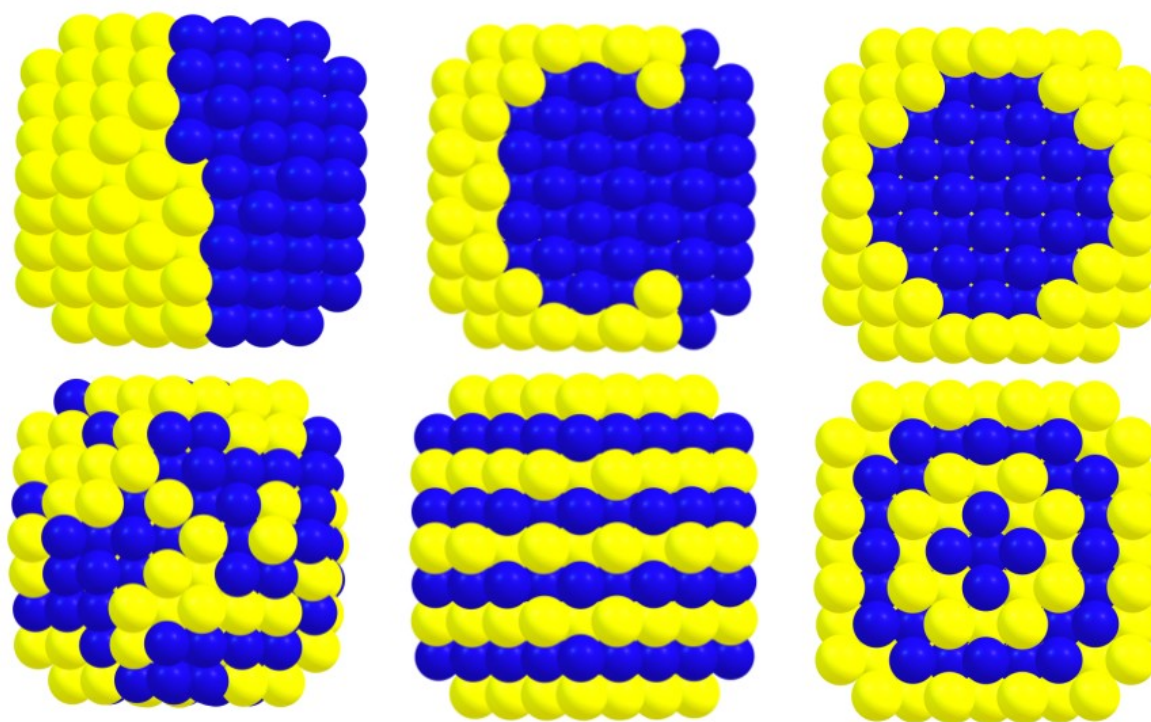


Figure 1-1 Schematic representation of some of the different mixing patterns available for bimetallic nanoparticles. Top row from left: a segregated nanoparticle, a ball and cup arrangement and a core-shell nanoparticle. Bottom row from left: a mixed nanoparticle with random ordering, known as a solid solution, a nanoparticle with ordered mixing, and a layered onion structure with alternating atomic layers from the center of the cluster. Based on figure 1 in reference (1).

Bimetallic nanoparticles and bimetallic clusters are aggregates of two different metals that bring additional benefits and disadvantages(1). Using two different metals enables them to mix in different ways, as shown in figure 1-1. These are different homotops; clusters with the same geometry and number of A and B atoms, but with different chemical ordering. There are two main types of particles: mixed and segregated. Mixed clusters can be ordered or randomly mixed in a solid solution. Segregated structures can be separated further, with sub cluster segregation being the least mixed A-B bonds. The other extreme is the core-shell arrangement, with a core of one element and a shell of another. Intermediate between the two extremes is

the ball and cup arrangement. Other systems have also been created experimentally(9), such as the onion structure of alternating layers of elements, and hollow nanoparticles. Clearly, the additional metal increases the complexity of the system. In theory, any metal can be mixed with any other metal, even in cases where the metals do not mix in the bulk (silver and copper, as an example). If we limit ourselves to the 30 transition metals, that gives 435 combinations. Searching through all of these experimentally is a challenge, and theoretical techniques can be used to assist experimentalists with finding low energy structures and useful properties.

The number of homotops increases combinatorially with the number of A and B atoms. For a binary cluster A_nB_m , the number of homotops (N_H) is given in formula 1-1 (1).

$$N_H = \frac{(n + m)!}{n! m!} \quad 1-1$$

For a binary cluster of $A_{15}B_{15}$, the number of combinations is 15,117,520 different combinations. Although some of these may be symmetry equivalent, it is impossible to complete a structural search of all possible combinations and a search algorithm must be used for all but the smallest cases (see Chapter 3- for a study on RhPd clusters).

1.3 Synthesis of Nanoparticles

Clusters (both mono and bimetallic varieties) can be studied either in the gas phase, on surfaces or in solution using various techniques which are described below

1.3.1 Molecular Beams

These types of methods were developed for studying free clusters, so adsorption effects do not change the cluster geometry. This technique was developed over 30 years(10-12) ago and enables the creation of size selected nanoparticles with a selected number of atoms(11) and a narrow composition range. For example, Knight et al. (13) studied size selected sodium clusters and were able to determine the different sizes down to the atom. More recently Qian et al.(14, 15) have studied thiol protected gold clusters containing 40 gold atoms. Finally Li et al. have studied larger size selected gold clusters with up to 309 atoms(16). The cluster generation occurs in three steps: vaporization, growth and analysis. This stage can happen in various ways, depending on the nature of the element, or elements, involved. This includes heating using a laser(17, 18) or an inert ion (for example Ar^+) beam, or by passing an electrical current through the sample. For bimetallic nanoparticles, the sample can be a mixed powder, an alloy of the two different elements or two different samples vaporized one after another(18). They can then pass through a carrier gas to cool the atoms down so they agglomerate. After this the clusters pass through a supersonic jet, increasing their velocity so no further growth is likely to occur. This gives the cluster a narrow size distribution(1). Analysis can happen within an inert gas matrix(19), or can be placed on a surface for further study using electron microscopy(20).

1.3.2 Colloidal methods

Although molecular beams can generate atomic clusters with a selected number of atoms to a high precision(21, 22), they cannot generate clusters in large quantities

required for industry. Therefore 'wet' colloidal methods can be used instead. These are created by precipitating a metal salt inside a solution containing some surfactant. The surfactant then binds to the clusters surface, limiting its growth. This method of creating nanoparticles is not new; it was the method Faraday used to create gold nanoparticles(6), although now different shapes of nanoparticle can be created, including cubes(23), flowers(9) and geometric polyhedral nanoparticle (23, 24). Bimetallic nanoparticles can be created in different ways- either precipitating two different metal salts at the same time, or creating nanoparticles from one metal first, followed by a second metal using the first as a seed to nucleate their growth(25).

1.4 Uses of Nanoparticles

Nanoparticles have been studied for many diverse applications. They have been studied for their magnetic properties (10, 26); with possible uses including data storage devices. Optical properties have also been studied (25).

Nanoparticles have been extensively studied for catalytic applications. Over 180 tons of palladium has been used in the automotive industry in 2011, along with 5 tons of rhodium for catalytic converters (27). Platinum has been extensively studied for fuel cell applications(28), although the costs are currently prohibitive for mass adoption. Alloying platinum with other metals has been studied, to reduce the overall cost of the fuel cell. In addition, alloying can reduce the effect of other gases poisoning the catalyst (29). However, alloying can also affect the stability of the catalyst, altering its structure to strengthen the binding of poisons. This has been shown to occur for CO on copper-platinum surfaces (30, 31).

Chapter 2- Density Functional Theory

2.1 Basic Quantum Mechanics

Quantum mechanics was developed early in the 20th century, as classical mechanics could no longer explain various experimental results known at that time. As an example, when light is passed through two slits with a distance similar to its wavelength, a diffraction pattern is observed(32). However, this effect not only applies to light but can also apply to electrons(33, 34) and similar experiments have even resulted in the diffraction of much larger clusters(35). Other examples include the quantisation of light to explain black body radiation(33, 36).

Erwin Schrödinger(37, 38) introduced the concept of the wavefunction, commonly denoted as Ψ , from which all observable qualities (such as energy) can be found. Classical mechanics, based around Newton's laws of motion, assumes that all quantities (energy, momentum, position etc) can be perfectly known. This is no longer the case with a quantum mechanical system, due to Heisenberg's uncertainty principle(39). This makes finding observables for a quantum system, such as the positions of electrons in a nanoparticle, problematic.

To find the energy of N electrons interacting with M nuclei without relativistic effects or external fields is given in equation 2-1(40).

$$\hat{H}\Psi_i(\vec{x}_1, \vec{x}_2 \dots \vec{x}_N, \vec{R}_1, \vec{R}_2 \dots \vec{R}_M) = E_i \Psi_i(\vec{x}_1, \vec{x}_2 \dots \vec{x}_N, \vec{R}_1, \vec{R}_2 \dots \vec{R}_M) \quad 2-1$$

x denotes the position of the electrons and R the location of each nucleus. It is worth noting that the wavefunction is not directly observable, although the wavefunction multiplied by its complex conjugate Ψ^* is the probability of finding the particles 1 through N within a small volume element(40). \hat{H} is the Hamiltonian operator upon the wavefunction to get the energy E , which is given in equation 2-2.

$$\hat{H} = -\frac{1}{2} \sum_{i=1}^N \nabla_i^2 - \sum_{A=1}^M \frac{1}{2M_A} \nabla_A^2 - \sum_{i=1}^N \sum_{A=1}^M \frac{Z_A}{r_{iA}} + \sum_{i=1}^N \sum_{j>i}^N \frac{1}{r_{ij}} + \sum_{A=1}^M \sum_{B>A}^M \frac{Z_A Z_B}{R_{AB}} \quad 2-2$$

Each term represents a different contribution towards the energy. The first and second terms represent the kinetic energy of the electrons and nuclei, respectively. The third, fourth and fifth terms represent the nuclear-electron, electron-electron and nuclear-nuclear coulombic interactions. Z is the charge of each nucleus, and M its mass. R is the distance between nuclei, r_{ij} the distance between the electron i and j , and r_{iA} the distances between the atom A and the electron i . Clearly this is an impossible equation to solve, except for the simplest systems, so approximations have to be made.

It is now worth noting that equation 2-2, and all the formulae in this chapter, uses atomic units with the rest mass of the electron, electron charge and $1/4\pi\epsilon_0$ set to unity. This is a common method to simplify the equations slightly (40).

The first approximation that is often used is the Born-Oppenheimer approximation(41). As the nuclei are over 1800 times heavier than the electron, we can assume that the nuclei are fixed with respect to the electrons and do not move, or move so slowly that the electrons react immediately to the moving nuclei. This makes the second term in equation 2-2 is effectively equal to zero, and the fifth term

becomes a constant, which is trivial to calculate. This still leaves us with the electronic Hamiltonian to calculate, given in equation 2-3.

$$\hat{H} = -\frac{1}{2} \sum_{i=1}^N \nabla_i^2 - \sum_{i=1}^N \sum_{A=1}^M \frac{Z_A}{r_{iA}} + \sum_{i=1}^N \sum_{j>i}^N \frac{1}{r_{ij}} \quad 2-3$$

$$\hat{H} = \hat{T} + \hat{V}_{Ne} + \hat{V}_{ee}$$

The wavefunction must be normalised, such that all electrons must be somewhere in space (equation 2-4).

$$\int \cdots \int |\Psi(\vec{x}_1, \vec{x}_2 \cdots \vec{x}_N)|^2 d\vec{x}_1, d\vec{x}_2 \cdots d\vec{x}_N = 1 \quad 2-4$$

Electrons are also indistinguishable fermions, with a magnetic quantum number $m_s = \pm 1/2$, which make the wavefunction anti-symmetric. If two electrons are interchanged, the sign of the wavefunction changes as shown in equation 2-5.

$$\Psi(\cdots, \vec{x}_i, \vec{x}_j, \cdots) = -\Psi(\cdots, \vec{x}_j, \vec{x}_i, \cdots) \quad 2-5$$

This is the mathematical notation of the Pauli exclusion principle(42, 43).

2.1.1 Variational principle

The variational principle is used widely in both quantum mechanics and in DFT. It can be shown that the expectation value of any observable O can be found from its wavefunction using equation 2-6.

$$\langle \hat{O} \rangle = \langle \Psi | \hat{O} | \Psi \rangle \equiv \int \cdots \int \Psi \hat{O} \Psi d\vec{x}_1, d\vec{x}_2 \cdots d\vec{x}_N \quad 2-6$$

The important part of the variation principle is that a trial wavefunction can be used, and this can then be minimised relative to the desired quantity. If we look at the energy E' of a trial wavefunction Ψ_{trial} , we end up with equation 2-7.

$$\langle \Psi_{\text{trial}} | \hat{H} | \Psi_{\text{trial}} \rangle = E' \geq E_0 = \langle \Psi_0 | \hat{H} | \Psi_0 \rangle \quad 2-7$$

The equality holds if the trial wavefunction is equal to the ground state wavefunction Ψ_0 . To get to E_0 we use equation 2-8.

$$E_0 = \min_{\Psi \rightarrow N} E(\Psi) = \min_{\Psi \rightarrow N} \langle \Psi_{\text{trial}} | \hat{H} | \Psi_{\text{trial}} \rangle \quad 2-8$$

Then we can take an external potential from the nuclei and construct \hat{H} . Then we can guess at a trial wavefunction which can give us the desired ground state wavefunction, from which the energy and any other observable can be found if the trial wavefunction is the same form as the 'real' wavefunction. If the function isn't in the correct form it will always be higher in energy than the actual systems energy.

2.1.2 Limits of 'true' quantum mechanical methods

The problem with this is the computational resources needed to calculate the wavefunction. Every electron is interacting with every other electron, giving us 4^N degrees of freedom (3 dimensions of space, plus spin). It has been noted that even great advances in computer power can't overcome the 'exponential wall' when large systems containing hundreds of electrons are treated(44). However, the electron density (which is simply the square of the wavefunction) only varies in three dimensions, so it should be possible to get observables from the density (often denoted as ρ) as well as the wavefunction.

2.2 Density Functional Theory (DFT)

2.2.1 Early Attempts- The Thomas-Fermi Model

The very earliest attempt at using the density instead of the wavefunction was published only a year after Schrödinger's work independently by Enrico Fermi(45) and Llewellyn Thomas(46). Assuming a homogenous electron gas, the kinetic energy T_{TF} of the electrons is given in equation 2-9(40).

$$T_{TF} = \frac{3}{10} (3\pi^2)^{2/3} \int \rho^{5/3}(\vec{r}) d\vec{r} \quad 2-9$$

This can be combined with nuclear-electron attraction and electron-electron repulsion to give a total energy (equation 2-10).

$$E_{TF} = T_{TF} - \sum_{A=1}^M Z_M \int \frac{\rho(\vec{r})}{r} d\vec{r} + \frac{1}{2} \iint \frac{\rho(\vec{r}_1)\rho(\vec{r}_2)}{r_{12}} d\vec{r}_1 d\vec{r}_2 \quad 2-10$$

Z_M is the charge on each nucleus M . This approach gave reasonable atomic energies, although chemical bonding was found to be an endothermic process, with the separate atoms having a lower energy than molecules, or with atoms only binding weakly to each other(47, 48). Expansions have been made to the Thomas-Fermi model, for example treating the electrons as an inhomogeneous gas by adding gradient terms, but the lack of quantum mechanical exchange and correlation effects (see below) limited the results of the theory. Despite this, it is worth noting that the wavefunction was not used to get the energy of the system, even though it had not been explicitly proven that electron energies can be found from the density alone.

2.2.2 The Hohenberg-Kohn Theorems

2.2.2.1 The First Hohenberg-Kohn Theorem

The proof that it is possible (at least in theory) to get the correct ground state energy from the density alone was achieved by Hohenberg and Kohn in 1964(49). The proof was surprisingly simple, although it was found 38 years after Schrödinger's work. It states that "the ground state energy must be a unique functional of ρ , which is a function of the wavefunction" (50) (shown in equation 2-11).

$$E_0(\rho_0) = T(\rho_0) + E_{ee}(\rho_0) + E_{Ne}(\rho_0) \quad 2-11$$

The kinetic energy T and electron-electron energy E_{ee} terms are often referred to as the Hohenberg-Kohn functional, as it is the part that is dependent on the density alone, and not any external potential (equation 2-12).

$$F_{HK}(\rho) = T(\rho) + E_{ee}(\rho) \quad 2-12$$

The nuclei- electron interaction E_{Ne} is the simplest, as it is the columbic interaction between the nuclei (with charge Z) and the electron density (equation 2-13).

$$E_{Ne}(\rho) = -Z \int \frac{\rho(\vec{r})}{r} d\vec{r} \quad 2-13$$

The Hohenberg-Kohn functional is more problematic due to quantum mechanical electron-electron interactions, so this can be split into different sections. Firstly, a classical electron kinetic energy without any electron-electron effects

included; secondly, a coulombic repulsion of the electron density with itself and thirdly all the other ‘unknown’ quantum mechanical effects, E_{ncl} .

$$\begin{aligned}
 F_{HK}(\rho) &= T'(\rho) + \frac{1}{2} \iint \frac{\rho(\vec{r}_1)\rho(\vec{r}_2)}{r_{12}} d\vec{r}_1 d\vec{r}_2 + E_{ncl} \\
 &= T'(\rho) + J(\rho) + E_{ncl}
 \end{aligned}
 \tag{2-14}$$

2.2.2.2 The Second Hohenberg-Kohn Theorem

We have already found that variation theory can be used to find the lowest energy for a wavefunction. The second Hohenberg-Kohn theory states that a variation principle can be used to find the lowest energy E from varying a trial density $\tilde{\rho}$ (equation 2-13).

$$E_0 \leq E(\tilde{\rho}) = T(\tilde{\rho}) + E_{ee}(\tilde{\rho}) + E_{Ne}(\tilde{\rho}) \tag{2-15}$$

$E(\tilde{\rho})$ is the energy of the trial density.

In principle, the Hohenberg-Kohn theorem is exact, as no approximations have been made in the approach thus far. Therefore, if the kinetic energy operator, electron-electron and nuclear electron functional were known perfectly, then DFT could be used to find the exact energy for a system. Unfortunately, we hit a roadblock; that the kinetic energy functional is not known completely and the electron–electron interaction can’t be modelled completely due to quantum mechanical effects(40, 44).

2.2.3 The Kohn-Sham Equations

The Kohn-Sham equations were published one year after Hohenberg and Kohn's work, giving details of how to apply the Kohn-Hohenberg principle to a multi-electron system(49).

The electrons are treated as a collection of spin orbitals φ_i . Doing this enables the kinetic energy to be treated as a homogenous electron gas, (similar to the Thomas-Fermi model, but only for each orbital) as shown in equation 2-16. Any changes in kinetic energy due to electron interactions can be found using E_{ncl} in equation 2-14.

$$T'(\rho) = -\frac{1}{2} \sum_{i=1}^N \langle \varphi_i | \nabla^2 | \varphi_i \rangle \quad 2-16$$

We can now define E_{xc} as everything else, and contains terms for how the other electrons moves with respect to every other electron (first part of equations 2-17), and the repulsion of each electron due to the Pauli Exclusion Principle (second term in equation 2-17). Of course the Pauli Exclusion Principle only applies to electrons which have the same spin state.

$$\begin{aligned} E_{xc} &= [T'(\rho) - T(\rho)] + [E_{ee}(\rho) - J(\rho)] \\ E_{xc} &= T_c(\rho) + E_{ncl} \end{aligned} \quad 2-17$$

From E_{xc} we can define a potential, which is how E_{xc} affects the density, as defined in equation 2-18.

$$V_{XC} = \frac{dE_{XC}}{d\vec{r}} \quad 2-18$$

The orbitals can then be treated using a single Slater determinant, Φ with the additional potential V_{XC} added to account for the exchange correlation function. This is almost identical to the Hartree-Fock scheme, but including the exchange correlation term in the additional potential. The determinant is given in equation 2-19.

$$\Phi = \frac{1}{\sqrt{N!}} \begin{vmatrix} \varphi_1(\vec{x}_1) & \cdots & \varphi_N(\vec{x}_1) \\ \vdots & & \vdots \\ \varphi_1(\vec{x}_N) & \cdots & \varphi_N(\vec{x}_N) \end{vmatrix} \quad 2-19$$

The prefactor before the determinant is the normalisation constant. The energy of each orbital is given by the Kohn-Sham operator, \hat{f}_{KS} in equation 2-20 and 2-21.

$$\Phi = \hat{f}_{KS}\varphi_i = \varepsilon_i\varphi_i \quad 2-20$$

$$\hat{f}_{KS} = -\frac{1}{2}\nabla^2 - \sum_A \frac{Z_A}{r_{1A}} + \int \frac{\rho(\vec{r}_2)}{r_{12}} d\vec{r}_2 + V_{XC}(\vec{r}) \quad 2-21$$

Clearly, the number of electrons must equal the amount of electron density, which is equal to the sum of all occupied orbitals across both spin states as given in equation 2-22.

$$\rho = \sum_{i=1}^N \sum_S |\varphi_i(\vec{r}, s)|^2 \quad 2-22$$

2.2.4 Basis Sets

There are different ways of defining the orbitals within an atom or a molecule, split into two main categories: Linear Combination of Atomic Orbitals (LCAO) methods, and plane waves.

2.2.4.1 LCAO Basis Sets

Each orbital within the LCAO method is defined in equation 2-23.

$$\varphi_i = \sum_{\mu=1}^L c_{\mu i} \eta_{\mu} \quad 2-23$$

Where c is a coefficient describing how much a function η contributes to the overall orbital, and L is the maximum number of functions and coefficients for the orbital φ_i . To model the orbital perfectly, there would be an infinite number of functions, L . This is clearly unfeasible for a computer to be able to calculate.

The first functions are Slater Type Orbitals (STOs) suggested by Slater for Hartree-Fock calculations (51), and is defined in equation 2-24.

$$\eta_{\mu} = N r^{n-1} \exp[-\zeta r] Y_{lm}(\theta, \phi) \quad 2-24$$

n is the principle quantum number, $Y_{lm}(\theta, \phi)$ denotes the angular momentum contributions and ζ is a variable coefficient. The other forms are called Gaussian Type Orbitals (GTO's) (52), and are based on Gaussian distributions (equation 2-25).

$$\eta_{\mu} = N x^l y^m z^n \exp[-\alpha r^2] \quad 2-25$$

This time x , y and z denote the angular momentum contributions; N is a normalisation constant and α is a variable exponent. Although GTO's normally require more coefficients (higher L in equation 2-23) than STO's, as they don't have exhibit the correct density at the nucleus and decay too rapidly as the distance away from the nucleus increases, integration and differentiation is computationally cheaper as the multiplication of two Gaussian functions results in another Gaussian, so all integrals can be completed analytically.

2.2.4.2 Plane Wave basis Sets

Plane waves are another method of defining the orbitals, instead of using the LCAO method. These are exponential functions as shown in equation 2-27(40).

$$\eta^{PW} = e^{i\vec{k}\vec{r}} \quad 2-27$$

\vec{k} is the wave-vector which is related to the momentum of the electron. Importantly, these functions are not based around a nucleus but are spread across space and require periodic boundary conditions, so that infinite periodic systems (like crystals or bulk solids) can be calculated cheaply. Because of this the number of functions required to acquire reasonable energies is much larger than for STO's or GTO's. Gas phase molecules or atoms can be modelled using plane waves by placing it within a large enough box to minimise the interactions between neighbours. There are various different methods and implementations(53), including projected augmented wave (PAW) functions (54) norm-conserving (NC) pseudo potentials(55) and ultrasoft pseudo potentials(56).

2.2.5 Solving the Kohn Sham Equations

Now we have defined the equations for the atomic orbitals and the different potentials we are using, it is possible to explain how DFT can be used in a computational context, and we will use the LCAO method as an example. As stated above in equation 2-23, each orbital is defined as a combination of L coefficients c connected to some function η . Merging equation 2-23 with equation 2-21 gives us the energy of the orbital φ_i (equation 2-28).

$$\hat{f}_{KS}(\vec{r}_1) \sum_{\mu=1}^L c_{\mu i} \eta_{\mu}(\vec{r}_1) = \varepsilon_i \sum_{\mu=1}^L c_{\mu i} \eta_{\mu}(\vec{r}_1) \quad 2-28$$

This is then integrated over all space, giving a set of L equations (equation 2-29).

$$\sum_{\mu=1}^L c_{\mu i} \int \eta_v(\vec{r}_1) \hat{f}_{KS}(\vec{r}_1) \eta_{\mu}(\vec{r}_1) d\vec{r} = \varepsilon_i \sum_{\mu=1}^L c_{\mu i} \int \eta_v(\vec{r}_1) \eta_{\mu}(\vec{r}_1) d\vec{r} \quad 2-29$$

The integral on the left of equation 2-28 is called the Kohn-Sham matrix \mathbf{F}_{KS} , while the equation on the right is referred to as the overlap matrix \mathbf{S} , (as it gives the level of overlap between the functions η_{μ} and η_v . Both matrices have dimensions L by L . We also end up with L by L dimensional matrices of the coefficients, \mathbf{C} , and the energies ε given in equation 2-30 and 2-31.

$$\mathbf{C} = \begin{pmatrix} c_{11} & c_{12} & \cdots & c_{1L} \\ c_{21} & c_{22} & \cdots & c_{2L} \\ \vdots & \vdots & \ddots & \vdots \\ c_{L1} & c_{L2} & \cdots & c_{LL} \end{pmatrix} \quad 2-30$$

$$\boldsymbol{\varepsilon} = \begin{pmatrix} \varepsilon_1 & \dots & 0 \\ \vdots & \ddots & \vdots \\ 0 & \dots & \varepsilon_L \end{pmatrix} \quad 2-31$$

These matrices can be summarised as equation 2-32.

$$\mathbf{F}_{\text{KS}}\mathbf{C} = \mathbf{S}\mathbf{C}\boldsymbol{\varepsilon} \quad 2-32$$

This has turned a complex non-linear wavefunction (equation 2-1) where every wavefunction depends on every other, into a much simpler linear expression that can be solved.

It is now necessary to describe the elements of the Kohn Sham matrix and the Kohn Sham operator. As the kinetic energy and nucleus electron energies depend only on one electron, these can be easily merged into a single integral, h (equation 2-33).

$$h_{\mu\nu} = \int \eta_{\mu}(\vec{r}_1) \left[-\frac{1}{2} \nabla^2 - \sum_A^M \frac{Z_A}{r_{1A}} \right] \eta_{\nu}(\vec{r}_1) d\vec{r}_1 \quad 2-33$$

The coulombic electron-electron interaction term is more problematic, as it depends on two electrons. Initially, as the function η is a constant function and the occupancies of each orbital are defined by the c coefficients, a density matrix P can be defined in equation 2-34.

$$P_{\mu\nu} = \sum_{i=1}^N c_{\mu i} c_{\nu i} \quad 2-34$$

This gives us a collection of four-centre-two-electron integrals to solve. In equation 2-35, the four centres are η_{μ} , η_{ν} , η_{λ} , and η_{σ} , and the electron density at \vec{r}_1 and \vec{r}_2 .

$$J_{\mu\nu} = \sum_{\lambda}^L \sum_{\sigma}^L P_{\lambda\sigma} \iint \eta_{\mu}(\vec{r}_1) \eta_{\nu}(\vec{r}_1) \frac{1}{r_{12}} \eta_{\lambda}(\vec{r}_2) \eta_{\sigma}(\vec{r}_2) dr_1 dr_2 \quad 2-35$$

It is worth noting that this is often the slowest step in DFT, and slows down the calculation significantly, as L^4 four centre two electron calculations must be completed. A quicker method was suggested by Baerends, Ellis and Ros in 1973 (57), and reduces the complexity of solving this by using a charge fitting basis set. This replaces the $\eta_{\lambda}(\vec{r}_2) \eta_{\sigma}(\vec{r}_2)$ term with a sum of predefined functions, giving equation 2-36.

$$\eta_{\lambda}(\vec{r}_2) \eta_{\sigma}(\vec{r}_2) dr_2 \approx \sum_{\kappa=1}^k c_{\kappa} \omega_{\kappa} \quad 2-36$$

This reduces the calculation to a two-centre-two-electron integral and a summation, reducing the computational cost of the calculation significantly (58, 59).

2.2.6 Effective Core Potentials (ECP's)

For larger atoms, such as transition metals, the core electrons are often not involved in bonding to other nuclei and very little change is observed with their energy or density distribution. It is therefore common to fit a potential to all the core electrons and treat them as a single unit, as initially suggested by Hellmann in 1935(60). In the case of gold, this can reduce a 79 electron atom to 11 electrons and a core potential of 68 electrons (with [Xe], 4f₁₄ electrons treated by the core potential, significantly reducing the complexity of the calculation(61). Smaller effective core potentials can be used to increase the accuracy of the calculations(62).

ECP's are required for plane wave calculations, as the number of plane waves needed to define the core electrons rapidly becomes prohibitively expensive(63) as a large number of pseudopotentials are required to model the core electrons accurately.

2.3 The Exchange Correlation Function

The exchange correlation (XC) function is split into two separate parts, electron exchange and electron correlation. The electron exchange is as a result of the Pauli Exclusion Principle that the wavefunction is antisymmetric. If we take a two electron system, swapping the two electron positions gives the density in equation 2-37.

$$\rho(x_1, x_2) = -\rho(x_2, x_1) \quad 2-37$$

This can only be true if and only if the probability of finding both the electrons at the same point in space is zero. It is worth noting this has nothing to do with the coulombic repulsion, and is applicable to uncharged fermions (for example, neutrons) (40). Electron correlation is the reduction in coulomb repulsion due to the electrons avoiding each other. In addition, the semi-classical coulombic term in equation 2-14 includes the unphysical quantity of the electron interacting with its own charge. This effect should be cancelled out within the XC function.

2.3.1 The LDA and LSDA

The first attempt to define the exchange correlation is the Local Density Approximation (LDA) and assumes the electron density is constant or at least slowly varying (equation 2-38).

$$E_{XC}^{LDA}(\rho) = \int \rho(\vec{r}) \varepsilon_{XC}(\rho(\vec{r})) d\vec{r} \quad 2-38$$

The term ε_{XC} is split into its corresponding exchange and correlation contributions, as in equation 2-39.

$$\varepsilon_{XC}(\rho(\vec{r})) = \varepsilon_X(\rho(\vec{r})) + \varepsilon_C(\rho(\vec{r})) \quad 2-39$$

ε_X can be derived exactly, whereas ε_C has been found by fitting to quantum Monte-Carlo simulations(40).

The LDA functional assumes that all the electrons are spin paired, with no unpaired electrons. It is however trivial to expand this, resulting in the Local Spin Density Approximation (LSDA) (equation 2-40).

$$E_{XC}^{LDA}(\rho) = \int \rho(\vec{r}) \varepsilon_{XC}(\rho_\alpha(\vec{r}), \rho_\beta(\vec{r})) d\vec{r} \quad 2-40$$

LDA and LSDA have a tendency towards over binding, as they overestimate the correction to the electron-electron repulsion(64).

2.3.2 GGAs

The next obvious step is to assume the density is slowly varying, resulting in exchange-correlation functions that contain gradient terms(65). There are many variations, all based on the Generalised Gradient Approximation (GGA) (equation 2-41). These are related to a function of the density and its gradients.

$$E_{XC}^{GGA}(\rho) = \int f(\rho_\alpha, \rho_\beta, \nabla \rho_\alpha, \nabla \rho_\beta) d\vec{r} \quad 2-41$$

As with the LDA and LSDA, these can be split into exchange and correlation terms.

The two main exchange correlation functions used in this work are the Perdew-Wang 91 (PW91) (64) and the Perdew-Becke-Ernzerhof (PBE) (65, 66) exchange correlation functional, both of which are GGA's.

2.3.3 Hybrid functionals

Hybrid functionals contain a mixture of LDA and GGA terms, with electron exchange explicitly calculated using Hartree Fock techniques. The most famous example(67) is the B3LYP functional developed by Becke, Lee, Yang and Parr(68, 69), and is given in equation 2-42

$$E_{XC}^{B3LYP}(\rho) = (1 - 0.20)E_X^{LSDA} + 0.2E_X^{HF} + 0.72E_X^{B88} + 0.81E_C^{LYP} + (1 - 0.81)E_C^{LSDA} \quad 2-42$$

Where E_X^{LSDA} and E_C^{LSDA} are the respective exchange and correlation parts of the LSDA, E_X^{B88} is the exchange functional by Becke, E_C^{LYP} the correlation functional by Lee Yang and Parr and E_X^{HF} is the exchange found using Hartree Fock. The coefficients are fitted to various experimental results, including atomisation energies and ionisation potentials. Many other hybrid functionals exist, including PBE0(70), mPW1PW91(71) and X3LYP(72).

2.4 Relativistic DFT (RDFT)

Relativity plays a large role in the electron structure of heavier atoms(73), including the late transition metals gold and platinum. Due to the large charge at the nucleus, the core electron exhibit strong nuclear-electron interaction, increasing their kinetic energy to velocities approaching the speed of light. This causes the core electron

orbitals to contract, and has been found to be the main reasons why small gold clusters are planar, and for gold's yellow colour(74). There are three major effects that occur when relativity is taken into account(74).

- As the electron reach velocities approaching the speed of light near the nucleus, their mass increases and the s and p orbitals contract.
- As the s and p orbitals contract, the d and f orbitals expand as they have larger orbital momentum so spend more time outside the core. In addition, the contraction of the s and p orbitals results in more shielding, again increasing orbital expansion
- Spin orbit coupling occurs; coupling the orbital angular momentum l with the intrinsic spin angular momentum s .

There are various levels of approximation for RDFT calculations. For lighter atoms where relativistic effects are small, perturbation theory can be used, with the relativistic effects treated as a small perturbation of the non-relativistic density. For heavier atoms, the relativistic effects are no longer negligible, so other methods must be used. The full RDFT approach uses a 4-component Dirac Hamiltonian(73). Unfortunately, this method gives no bound states with two or more electrons, and is very computationally expensive. Other methods exist, including the Zeroth Order Regular Approximation(75, 76) (ZORA) which can be used to account for relativistic effects cheaply(77). The kinetic energy functional T is replaced with equation 2-43 (78).

$$T^{ZORA} = \vec{\sigma} \cdot \vec{p} \frac{c^2}{2c^2 - V} \vec{\sigma} \cdot \vec{p} \quad 2-43$$

$\vec{\sigma}$ are the Pauli spin matrices, p the momentum, c is the speed of light and V the potential.

A further approximation can be made by neglecting the spin matrices. This was first implemented for closed shell systems but can be expanded for open systems, and is called the scalar relativistic (SR) approximation (equation 2-44). It is the SR approximation that will be used for most of this work. This approximation is valid for calculating binding energies of larger clusters, but has been shown to affect the structure of the global minima for small gold clusters. In addition, calculating excitation spectra (such as UV/vis spectra) would require ZORA, as the electron energy spacing would change due to spin orbit coupling.

$$T^{SR} = \vec{p} \frac{c^2}{2c^2 - V} \vec{p} \quad 2-44$$

2.5 DFT Programs

Many programs exist for performing DFT calculations. Including the Gaussian package(79), VASP(80-82), GPAW(83) and CASSTEP(84) each using different syntax and optimised for different problems. This work has used two different DFT codes, NWChem(85) and Quantum Espresso(53), a brief introduction is included below.

2.5.1 Quantum Espresso

Quantum Espresso(53) (opEn Source Package for Research in Electronic Structure, Simulation and Optimisation) is a modular DFT code for calculating structures and energies of quantum mechanical systems. It is exclusively a plane

wave code, although calculations of gas phase molecules can be achieved by performing the calculations using the gamma point within a large box. The ECP basis sets are available with the program or they can be created by different modules within quantum espresso. Phonon calculations can be performed, as can geometry relaxation and variable cell calculations. Quantum espresso is also extensively parallelised, using a mixture of OpenMP and the Message Parsing Interface (MPI) protocol. It contains packages for analysing charges on atoms, and Partial Density of States (PDOS).

2.5.2 NWChem

NWChem(85) is an extensive chemistry package, able to calculate properties using DFT, coupled cluster, Møller–Plesset perturbation theory and force-field methods. It can also perform Time Dependent DFT (TDDFT) calculations, and Quantum Mechanical Molecular Mechanics (QM-MM) simulations, such that a small area can be treated using QM whereas the rest can be treated using computationally cheaper methods. It has been extensively parallelised using the Global Array method(86), so that large calculations can be run on multiple processors with minimal overhead. For DFT, it utilises the Gaussian LCAO method, and charge fitting basis sets can also be used. It can be used to calculate DFT calculations using plane waves. Many properties can be calculated, including energies, geometry optimisation and vibration frequencies. The current version is version 6.0, contains over 11 million lines of C and Fortran 77 code, and is released under Open Source Educational Community Licence. It was used to compare some of our results to previous work performed using the same package, basis sets and XC functional(3, 4, 87-90).

2.6 Conclusions

The DFT approach has been used extensively for the study of metallic clusters, which traditional wavefunction based methods fail to complete within a desired timeframe. Although issues due to the exchange correlation function exist, these errors are small if a suitable functional is used. As such, most of the work in this thesis is based on DFT calculations. Where DFT becomes too expensive, such as for energy landscape searches or for very large (a few hundred atoms) metal clusters, lower level techniques can be used.

Chapter 3- The Structure of RhPd Nanoparticles

3.1 Introduction

3.1.1 Rhodium and Palladium Nanoparticles

3.1.1.1 Rhodium Nanoparticles

Rhodium has been extensively studied as a three-way catalyst in motor vehicle exhausts; for NO_x reduction; CO oxidation and of un-burnt hydrocarbons (91-94). It has also been investigated for the hydrogenation of various compounds and found to be active in the hydrogenation of arenes(95). Zhang et al.(96) synthesised different shaped Rh nanoparticles by using different rhodium salts, creating Rh cubes(97), cuboctahedra(97), tetrahedra(98) and icosahedra(98) by changing the reaction conditions. Hydrogenation of aromatic compounds has been achieved with Rh nanoparticles, using different phosphine groups to modify the surface of the cluster and change the selectivity of the nanoparticles(29).

3.1.1.2 Palladium Nanoparticles

Palladium has also been used in automotive catalysis to remove greenhouse gases. Over 150 tonnes of Pd was used in the automotive industry in 2010 (27). For this use, an 'intelligent' Pd catalyst has been developed to increase the lifetime of the catalyst, by regenerating the palladium from a perovskite to the Pd nanoparticle(99, 100). Due to the high price of platinum, Pd is often added to decrease the cost of Pt catalysts(27). It has also been investigated for NO_x adsorption(92) and

rearrangement of alkene-alcohols to carbonyl compounds(101). Pd in the bulk is able to absorb hydrogen, and this has been investigated within nanoparticles(102).

3.1.2 Rhodium-Palladium Bimetallic Nanoparticles

RhPd in the bulk has an extensive miscibility gap, and only forms an alloy at high temperature or low concentration of the impurity atoms. However, RhPd nanoparticles have been synthesised for various applications, across the entire composition range(103). These include mixed nanoparticles(103), $\text{Rh}_{\text{core}}\text{Pd}_{\text{shell}}$ nanoparticles and $\text{Pd}_{\text{shell}}\text{Rh}_{\text{core}}$ nanoparticles(104-106). The bimetallic system has been studied to improve various catalytic reactions, both using theoretical(107) and experimental methods(95, 108) compared with the bulk alloys. Hollow RhPd nano spheres have also been created(109).

3.2 Searching the Potential Energy (PES) Landscape

Searching for the lowest energy clusters and searching for the global minimum (GM) structure is a difficult task. The challenge is due to the large number of possible structures and, for bimetallic clusters, their homotops(2, 110). Performing this search through systematically searching the whole Potential Energy Surface (PES) is unfeasible except for the smallest systems(111). In this chapter, various methods are used to search the energy landscape.

3.2.1 The Gupta Potential

DFT relaxation calculations typically take a few hours using multiple processors even for a 38 atom system. As such, a full search at the DFT level is unfeasible except for the smallest clusters(112-114). Therefore, it is necessary to search at a lower level of

theory, before moving to DFT. This enables a wide search of the PES to be completed accurately, while maintaining computational speed. The Gupta potential was selected, as it contains five different parameters which can be fitted to experimental(115) or theoretical data. It is a many body additive potential, based on the second moment approximation in tight binding theory. The attractive term (V_a) and repulsive (V_r) are summed over all atoms N .

$$E_{clust} = \sum_{i=1}^N V_r(i) - V_a(i) \quad 3-1$$

$$V_r(i) = A(a, b) \sum_{i \neq j}^N \exp \left[-\rho(a, b) \left(\frac{r_{ij}}{r_0(a, b)} - 1 \right) \right] \quad 3-2$$

$$V_a(i) = \zeta(a, b) \sqrt{\sum_{i \neq j}^N \exp \left[-2q(a, b) \left(\frac{r_{ij}}{r_0(a, b)} - 1 \right) \right]} \quad 3-3$$

The four parameters $\rho(a, b)$, $q(a, b)$, $A(a, b)$ and $\zeta(a, b)$ are the fitted parameters between atoms a and b . $r_0(a, b)$ is the bond length of the bulk material. This bond length is often unavailable for the bimetallic system, so is taken as the average between the bulk values of the pure metals (3, 4, 87, 89, 116-118) in agreement with Vegards law(119).

3.2.2 Genetic Algorithm

Genetic Algorithm's (GA's) (120) are based on Darwin's principle of natural selection(121) using operators analogous to those used in nature to optimise the structures. In nature, parents that are best suited to their environment are more likely

to survive for longer and have more offspring. In addition, mutations may create beneficial attributes, and improve the individual's life expectancy and therefore its chance of producing children.

For cluster optimisation, an initial population is generated from random coordinates. These are optimised locally (similar to young growing up into adulthood). Each cluster is then assigned a fitness value based on its energy. The best clusters then undergo crossover, by merging different clusters together to make new structures. A small number of clusters also undergo mutation operations, such as swapping atoms or moving them a small distance.

We used the Birmingham Cluster Genetic Algorithm (BCGA) for this research, which has been used extensively for optimisation of metal clusters and nanoalloys (3, 110, 116, 122).

3.2.3 Basin Hopping

The BCGA described above is very good at finding structures, but sometimes has difficulties finding the correct homotop; particularly for larger clusters. Basin Hopping (BH) is a method of crossing the energy barriers between local minima involving moving or swapping an atom, followed by a local minimisation. If the new structure is of a lower energy than its predecessor, it is accepted. If it is higher it is accepted if a random number N is less than the metropolis criterion:

$$N \leq e^{-\frac{\Delta E}{k_b T}} \quad 3-4$$

Where ΔE is the energy difference between the structures, T the (fictitious) temperature variable that decides how high in energy structures will be accepted,

and k_b is the Boltzmann constant. When T is higher, higher energy homotops are accepted to enable a wider search of the energy landscape to be conducted. This is repeated for a set number of runs.

3.2.4 High Symmetry Searches

Different high symmetry homotops can also be studied to compare the relative energies of higher energy structures, while limiting the number of homotops to be studied. For example, a 38 atom Truncated Octahedral (TO) cluster has three sets of symmetry-equivalent sites: core, surface and vertex sites as shown in figure 3-1. This limits the number of different clusters to eight different compositions, of which six are bimetallic. This enables a systematic search of various compositions at the DFT level.

For 98 atom structures, it is known for a Lennard Jones cluster that the putative global minimum structure is the Leary Tetrahedron (LT) (123), and its construction is shown in figure 3-1. This structure had full T_d symmetry and is known to be a challenging structure to find on the potential energy landscape. It is made up of a 20 atom tetrahedral core, which is capped twice on the (111) faces of the tetrahedral core. Then 7 atoms are added to each face along in between the caps on the (100) sites. For full T_d symmetry, there are 9 different symmetry equivalent sites (also shown in figure 3-1) giving 512 different combinations. These structures can all be minimised and compared with low energy structures from the GA or BH calculations.

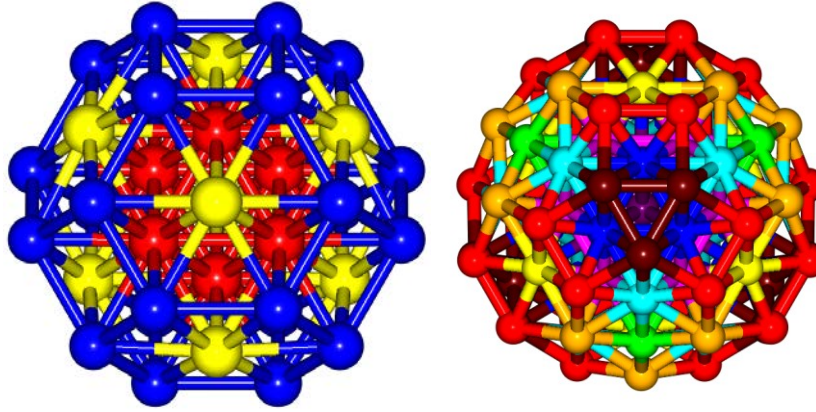


Figure 3-1 (Left) The different symmetry equivalent sites for the 38 atom TO cluster. Core sites are shown in red, and surface and vertex sites are shown in yellow and blue, respectively. The 98 atom Leary Tetrahedron, with each symmetry equivalent site shown in a different colour.

3.3 Methodology

3.3.1 Potentials

For the pure metal (Pd-Pd and Rh-Rh) interactions, two different potentials were used. Firstly, the potentials fitted by Cleri and Rosato were used(115), and were created by fitting the parameters to experimental results for lattice constants, cohesive energies and elastic constants. The second potential was fitted to DFT calculations. First, the energies of the Rh and Pd face centred cubic (FCC) solids were calculated with different lattice constants, varying from 6.4 to 9.0 bohr (3.39Å to 4.76Å). From these calculations, the lattice constant and the energy were found. The bulk modulus was found by fitting a quadratic equation to the bottom of the potential well, and the second differential was found with respect to the lattice constants x (equations 3-5 and 3-6).

$$E = ax^2 + bx + c \quad 3-5$$

$$\frac{d_2 E}{dx^2} = \pm 2a \quad 3-6$$

The values for the lattice constant, binding energy and bulk modulus were then shifted, so that they were equal to their corresponding experimental values. A basin hopping fitting program, written by Giovanni Barcaro (CNR, Pisa), was then used to fit the parameters to the energy curves.

In previous work by Pittaway et al. on AuPd (87), the bimetallic potentials were based on the average of the Cleri and Rosato values. The geometric and arithmetic potentials give similar coefficients so were rounded between the two averages. For RhPd, this is no longer the case, probably due to the larger difference between the cohesive energies of Rh and Pd compared with Pd and Au. Therefore two different bimetallic potentials were calculated using the Cleri and Rosato values. “Arith” was taken as the arithmetic mean of pure Rh and Pd, whereas “Geomt” was taken as the geometric mean.

The bimetallic DFT fitted potential was created in the same way as the pure Rh and Pd DFT potentials, but with the ordered alloys of Rh₁Pd₃, Rh₂Pd₂ and Rh₃Pd₁. The parameters for each potential are shown in Table 3-1.

Parameters	Arith	Geomt	DFT-fit
Rh-Rh A	0.0629		0.048803
Rh-Rh ζ	1.66		1.588098
Rh-Rh p	18.45		18.454169
Rh-Rh q	1.867		1.922829
Rh-Rh r_0	2.689		2.6890
Rh-Pd A	0.11875	0.1048	0.089646
Rh-Pd ζ	1.689	1.6888	1.87609
Rh-Pd p	14.6585	14.1597	14.677739
Rh-Pd q	2.8045	2.6432	2.882234
Rh-Pd r_0	2.719	2.7188	2.71875
Pd-Pd A	0.1746		0.172925
Pd-Pd ζ	1.718		1.70946
Pd-Pd p	10.867		10.867475
Pd-Pd q	3.742		3.738965
Pd-Pd r_0	2.749		2.7485

Table 3-1 The parameters for the three different potentials. The pure “Arith” and “Geomt” potentials are both from reference (115), with the bimetallic coefficients calculated using the arithmetic and geometric means, respectively. The “DFT-fit” coefficients are derived from bulk DFT calculations on FCC Rh and Pd for the monometallic potentials, and Rh₁Pd₃, Rh₂Pd₂ and Rh₃Pd₁ FCC bulk alloys for the Rh-Pd coefficients.

3.3.2 Genetic Algorithm

An initial population of 40 clusters was chosen, with the GA ceasing operation after 10 runs when the population reaches stagnation and no lower energy structures are found. Clusters have a 10% chance of undergoing mutation, where the entire cluster is replaced with a random geometry. The fitness is based on the hyperbolic tangent function. A cluster with energy E_i is compared with the highest (E_{\max}) and lowest (E_{\min}) energy structure within the population, using formulae 3-7 and 3-8.

$$\theta_i = \frac{E_{\min} - E_i}{E_{\max} - E_{\min}} \quad 3-7$$

$$f_i = \frac{1 - \tanh(2\theta_i - 1)}{2} \quad 3-8$$

The cluster is selected if the fitness f_i is greater than a random number between 0 and 1. Each composition was run for 100 runs to increase the chance of finding the lowest energy structure, with each run starting with a different random seed to ensure initial structures are different for each run.

3.3.3 Basin Hopping

Basin hopping was performed using the program written by Giovanni Barcaro(3). It performs swaps of different atoms, followed by a minimisation routine. As the purpose of the basin hopping algorithm is to finding lower energy homotops, k_bT was set to 0.02eV (3). The program was run for 500 generations.

3.3.4 DFT Calculations

DFT calculations were performed with the Quantum Espresso quantum chemistry package(53), using scalar relativistic ultrasoft pseudopotentials(124, 125) explicitly accounting for the 5s, 5p and 4d orbitals for Pd and Rh. The PBE(65) functional has been used extensively to model metal systems, and was used for these calculations. An energy cut-off of 30 Ry was used with a kinetic energy cut-off of 240 Ry. Cluster calculations were performed at the gamma point, whereas the bulk measurements to create the DFT fitted potential were completed on a large k-point grid. Smearing was applied using gaussian broadening to assist convergence, and the calculations were spin-unrestricted.

3.3.5 Energy Analysis

There are multiple ways of analysing the energy of clusters, with differences between potential and DFT methods. For a cluster Rh_xPd_y The binding energy per atom (E_b) can be found using

$$E_b^{Gupta} = \frac{E_{cluster}}{x + y} \quad 3-9$$

$$E_b^{DFT} = \frac{E_{cluster} - xE_{Rh} - yE_{Pd}}{x + y} \quad 3-10$$

E_{Rh} and E_{Pd} are the energies of the Rh and Pd atoms. The excess energy (E_x) is defined as the mixing energy, and gives the energy of a bimetallic system relative to the pure clusters.

$$E_x = E(Rh_xPd_y) - x \frac{E(Rh_{x+y})}{x + y} - y \frac{E(Pd_{x+y})}{x + y} \quad 3-11$$

It is worth noting that using this notation mixing is preferred over segregation if E_x is negative, and E_x is zero by definition for the pure clusters.

A similar method of comparing the energy is the second difference energy (E_Δ). This is similar to E_x but is set relative to the nearest neighbours in the composition range, rather than to the pure clusters.

$$E_\Delta = 2E(Rh_xPd_y) - E(Rh_{x+1}Pd_{y+1}) - E(Rh_{x-1}Pd_{y-1}) \quad 3-12$$

Both E_x and E_Δ can be used unmodified at the Gupta potential and DFT level.

3.4 Results

3.4.1 34 Atom Clusters

Rh	0	1	2	3	4	5	6	7	8	9	10	11	12	13	14	15	16	17	18	19	20	21	22	23	24	25	26	27	28	29	30	31	32	33	34
Pd	34	33	32	31	30	29	28	27	26	25	24	23	22	21	20	19	18	17	16	15	14	13	12	11	10	9	8	7	6	5	4	3	2	1	0
Arith																																			
Geomt																																			
DFT																																			

Figure 3-2 The different structures found for 34 atom RhPd clusters for each of the three potentials. Different colours denote the different structures. Yellow- decahedra, magenta- icosahedra, cyan- face centered cubic-hexagonal closed pack (FCC-HCP), green- decahedral-icosahedral mixed structure (Dh-Ih) and red- C3 tetrahedra.

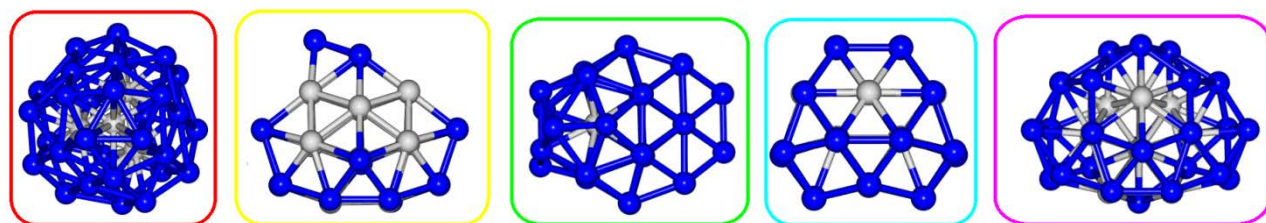


Figure 3-3 The different structures found by the BCGA for the 34 atom clusters. Borders indicate the colours in the composition diagram (figure 3-2). From left: C3 Tetrahedra, Decahedra, decahedra-icosahedra (Dh-Ih), FCC-hcp structure, icosahedra

These structures were optimised at the Gupta potential level using the BCGA, and the different structures for the three potentials are shown in figure 3-2 and figure 3-3. For the pure Rh_{34} and Pd_{34} cluster, all the potentials converge onto the same structures; an icosahedra-decahedral arrangement for Pd_{34} and a fragment of an icosahedron for Rh_{34} . The three potentials broadly agree on the energetically favoured structural families for Rh rich clusters. Icosahedral structures are preferred for a larger Rh content, before shifting to decahedral arrangements. At high to mid range Pd compositions, the three different potentials give different structural families. Doping a small number of Rh atoms into the Pd_{34} cluster does not affect the structural preference for the arithmetic or geometric potentials, whereas a single Rh atom changes the structure to decahedra for the DFT fitted potential. Interestingly,

the $\text{Rh}_4\text{Pd}_{30}$ arithmetic potential structure is based on a Rh_4 tetrahedron, surrounded by the Pd_{30} atoms in a chiral arrangement with C_3 symmetry, which is the same as the structure of the Au_{34}^- cluster(126). For low to mid range Rh compositions, the arithmetic potential shifts back to the icosahedral clusters, whereas geometric and DFT-fit potentials prefer FCC-hcp fragments. These are similar to fragments of the FCC truncated octahedral (TO) structures, with stacking faults on the incomplete side. All structures exhibit core-shell segregation, with the Rh in the core positions. At low Pd compositions, Pd atoms cap the vertex sites of the icosahedral structures.

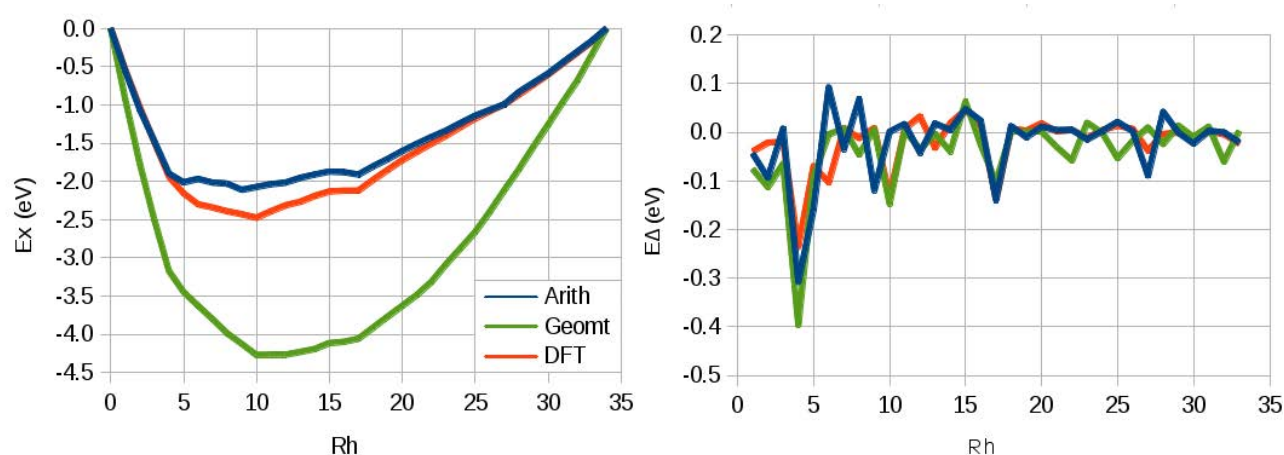


Figure 3-4 (Left) The excess energy of the three different potentials for the 34 atom structures across the composition range from pure Palladium (left) to pure Rhodium (right). (Right) the second difference energy of the three different potentials across the composition range.

Plots of the excess energy are shown in figure 3-4. The Arith and DFT-fitted potentials form similar curves, with the Geomt potential showing a more negative excess energy. The steep slope for increasing Rh content is due to placing Rh in the core positions. Rh has a higher cohesive energy than Pd (5.75 eV for Rh compared with 3.94 eV for Pd(127)). The curve remains on the negative slope until a composition of around $\text{Rh}_{10}\text{Pd}_{24}$, when most of the 'flat' surface sites are occupied with Rh.

E_{Δ} values are also shown in figure 3-4. The most obvious minimum for is at $\text{Rh}_4\text{Pd}_{30}$, with the perfect core-shell structure, whereas $\text{Rh}_5\text{Pd}_{29}$ must have Rh atoms on the surface. Another important minimum in E_{Δ} is at $\text{Rh}_{17}\text{Pd}_{17}$, probably due to the Pd atoms occupying all the vertex sites.

The arithmetic and DFT-fitted potentials exhibit similar characteristics to the palladium platinum system(117). On increasing the Pt concentration, the excess energy is relatively flat up to $\text{Pd}_{16}\text{Pt}_{18}$. At the DFT level, the energy landscape of 34 atom palladium platinum clusters was found to be complicated, with many competing low level minima(118). It also shows similarities to the copper silver system(128), with Cu occupying core sites. The CuAg system has a stronger peak at $\text{Cu}_7\text{Ag}_{27}$.

DFT calculations have been performed on the lowest lying minima of the $\text{Rh}_4\text{Pd}_{30}$ clusters for each potential. The lowest energy cluster was the C_3 tetrahedral cluster found with the arithmetic potential, with the decahedral structure from the DFT-fitted potential 0.1eV higher in energy and the geometric potentials dh-ih structure is 0.16eV higher in energy than the C_3 tetrahedron.

3.4.2 38 Atom Clusters

Rh	0	1	2	3	4	5	6	7	8	9	10	11	12	13	14	15	16	17	18	19	20	21	22	23	24	25	26	27	28	29	30	31	32	33	34	35	36	37	38	
Pd	38	37	36	35	34	33	32	31	30	29	28	27	26	25	24	23	22	21	20	19	18	17	16	15	14	13	12	11	10	9	8	7	6	5	4	3	2	1	0	
Anth																																								
Geomt																																								
DFT																																								

Figure 3-5 The different structures found for 38 atom RhPd clusters for each of the three potentials. Different colours denote the different structures. Yellow- Truncated Octahedron (TO), red- decahedral-icosahedral mixed structure (Dh-Ih), green- icosahedra and cyan- deahedra.

These structures were optimised using the same method as the 34 atom clusters. For 38 atom structures, figure 3-5 shows that the TO structure predominates for all three potentials at many compositions due to complete shell closure. Some icosahedral

and decahedral clusters are found in the composition range of $\text{Rh}_{20}\text{Pd}_{18}$ to $\text{Rh}_{31}\text{Pd}_7$ depending on the potential. In addition, for the arithmetic potential, a small number of decahedra-icosahedral structures are found between a composition range of $\text{Rh}_3\text{Pd}_{35}$ and $\text{Rh}_5\text{Pd}_{33}$. These structures have a 5 atom trigonal bipyramidal core and a pure Pd_{33} surface which may explain its stability.

The excess energies and second difference energies are shown in figure 3-6. The steepest part of the excess energy curve is between pure Pd_{38} and $\text{Rh}_6\text{Pd}_{32}$, which is the perfect $\text{Rh}_{\text{core}}\text{Pd}_{\text{shell}}$ structure. The minima for all potentials at $\text{Rh}_{14}\text{Pd}_{24}$ have Rh occupying the eight central (111) sites and the six core sites, resulting in all the Pd atoms on the vertex sites of the TO. The arithmetic and DFT fitted potentials exhibit a less negative slope between $\text{Rh}_6\text{Pd}_{32}$ and $\text{Rh}_{14}\text{Pd}_{24}$ the geometric potential, which is similar to the 34 atom clusters, although it is more pronounced for 38 atoms.

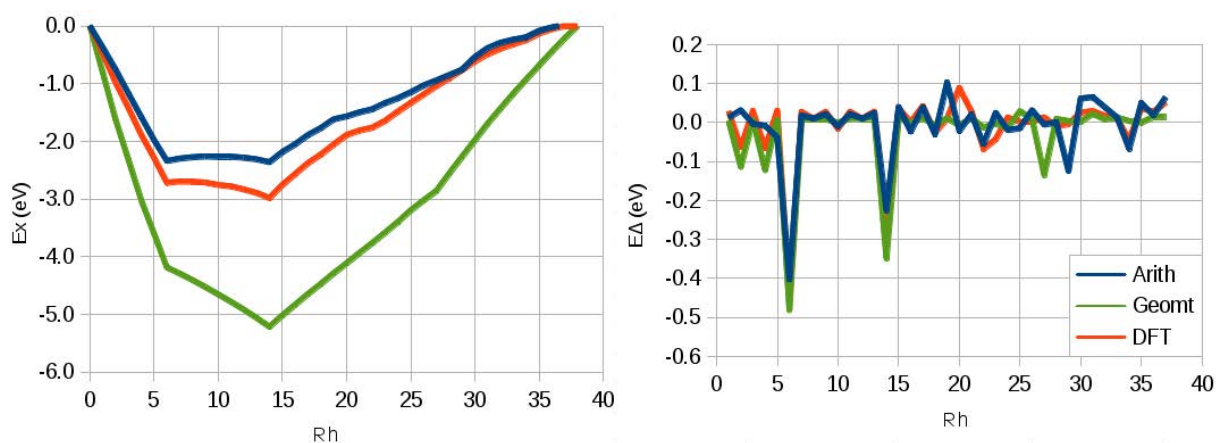


Figure 3-6 (Left) The excess energy of the three different potentials for the 38 atom structures across the composition range. (Right) the second difference energies of the three different potentials across the composition range.

The second difference energies for all three potentials exhibit strong minima for $\text{Rh}_6\text{Pd}_{32}$ and $\text{Rh}_{14}\text{Pd}_{24}$. These structures correspond to the O_h -symmetry $\text{Rh}_{\text{core}}\text{Pd}_{\text{shell}}$ and $\text{Rh}_{\text{core}}\text{Rh}_{\text{surface}}\text{Pd}_{\text{vertex}}$ TO structures.

DFT calculations were performed on all high symmetry TO structures, to compare how the energies of the different potentials compare with the higher level calculations. The difference between the binding energy of the potentials and DFT calculations were calculated using formula 3-13, and the results are shown in figure 3-7.

$$E_{Error} = E^{gupta} - E^{DFT} \quad 3-13$$

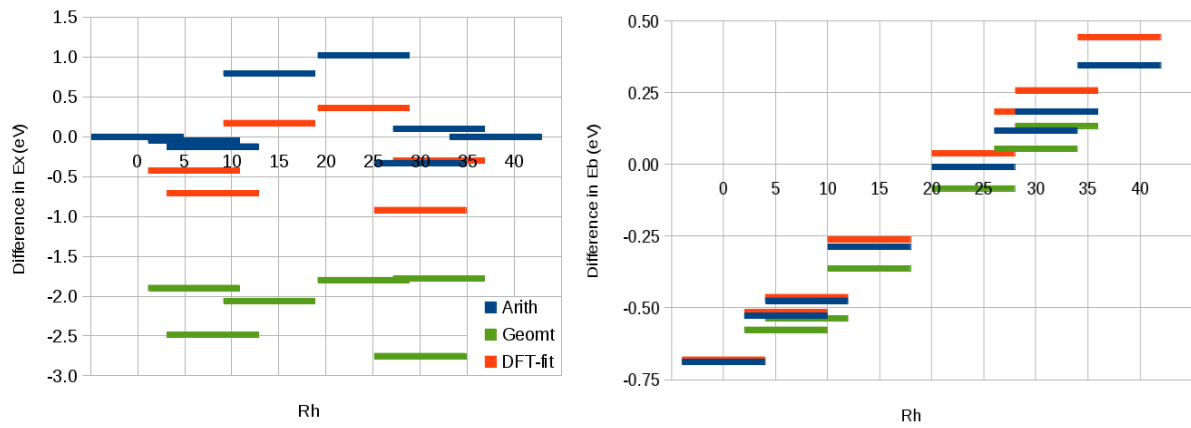


Figure 3-7 (Left) Difference between Ex for each potential and DFT calculations. (Right) Difference between Eb for each potential and the DFT calculations.

The geometric potential clearly does not give energies that are similar to the DFT calculations, having a strong tendency of overbinding. E_x shows that the DFT-fitted potential and the arithmetic potential exhibit similar errors, with the DFT-fitted potential suffering from overbinding by 0.30 eV on average and the arithmetic potential underbinding by 0.24 eV.

Comparing the binding energies to DFT calculations shows that the pure Pd_{38} cluster is over bound by 0.7 eV while the pure Rh_{38} cluster is underbound by between 0.35 eV and 0.44 eV. The pure potentials fitted by Cleri and Rosato are fitted to

experimental results, and the DFT-fitted potential was modified to fit experimental values of cohesive energy, bond lengths and bulk modulus. Therefore some of the error could be due to the difference between the PBE functional and the experimental fitting. Of course, these potentials have not been modified to account for surface energy that will have an effect.

3.4.3 55 Atom Clusters

Rh	0	1	2	3	4	5	6	7	8	9	10	11	12	13	14	15	16	17	18	19	20	21	22	23	24	25	26	27
Pd	55	54	53	52	51	50	49	48	47	46	45	44	43	42	41	40	39	38	37	36	35	34	33	32	31	30	29	28
Arith																												
Geomt																												
DFT																												

Rh	28	29	30	31	32	33	34	35	36	37	38	39	40	41	42	43	44	45	46	47	48	49	50	51	52	53	54	55
Pd	27	26	25	24	23	22	21	20	19	18	17	16	15	14	13	12	11	10	9	8	7	6	5	4	3	2	1	0
Arith																												
Geomt																												
DFT																												

Figure 3-8 Different structures across the composition range for the 55 atom clusters for each potential, with colour's referring to different structures. Green- icosahedra, red- FCC-HCP, yellow- FCC fragment (FCC), blue- decahedra, cyan- poly-decahedra, pink FCC/HCP/icosahedral mixed cluster and grey poly-icosahedra.

For Rh rich to medium compositions, the icosahedral motif dominates across all 3 potentials, due to the magic shell closure of the 55 atom icosahedron, as shown in figure 3-8. Unusually, the icosahedral structures are the only structure found for the DFT fitted potential. However, for the Pd rich clusters using the arithmetic and geometric potentials a large array of structures are found based around either FCC-hcp packing or decahedral clusters, rather than icosahedra.

The energies of the 55 atom clusters are shown in figure 3-9. The minimum of the excess energy for the arithmetic potential and the DFT fitted potential is $\text{Rh}_{13}\text{Pd}_{42}$, which corresponds to the perfect core-shell structure for icosahedral structures. This corresponds to a minimum at $\text{Rh}_{13}\text{Pd}_{42}$ in the second difference energy plots for all

potentials. The other major change in gradient for the arithmetic and DFT fitted potentials occurs at $\text{Rh}_{43}\text{Pd}_{12}$. After this point the Rh atoms have to occupy the vertex sites which greatly increase the surface energy.

The geometric potential mirrors the 34 and 38 atom excess energy plot with a more negative excess energy compared with the arithmetic or the DFT fitted potential. However the 55 atom structures also have clear minima corresponding to changes when different sites start being occupied by different atoms. The minima for the second difference energies are shown in figure 3-10. $\text{Rh}_{13}\text{Pd}_{42}$ is the perfect core-shell structure, and $\text{Rh}_{43}\text{Pd}_{12}$ has all the Pd atoms occupying the vertex sites. There is similar behaviour for the arithmetic and DFT fitted potentials. The $\text{Rh}_{23}\text{Pd}_{32}$ and $\text{Rh}_{33}\text{Pd}_{22}$ structures have interesting mixing motifs. $\text{Rh}_{23}\text{Pd}_{32}$ has all Rh surface sites surrounded by Pd atoms, whereas $\text{Rh}_{33}\text{Pd}_{22}$ has two helical chains of Pd atoms circling around the cluster. $\text{Rh}_{33}\text{Pd}_{22}$ and $\text{Rh}_{23}\text{Pd}_{32}$ have D_2 symmetry and $\text{Rh}_{13}\text{Pd}_{42}$ and $\text{Rh}_{43}\text{Pd}_{12}$ have high I_h symmetry.

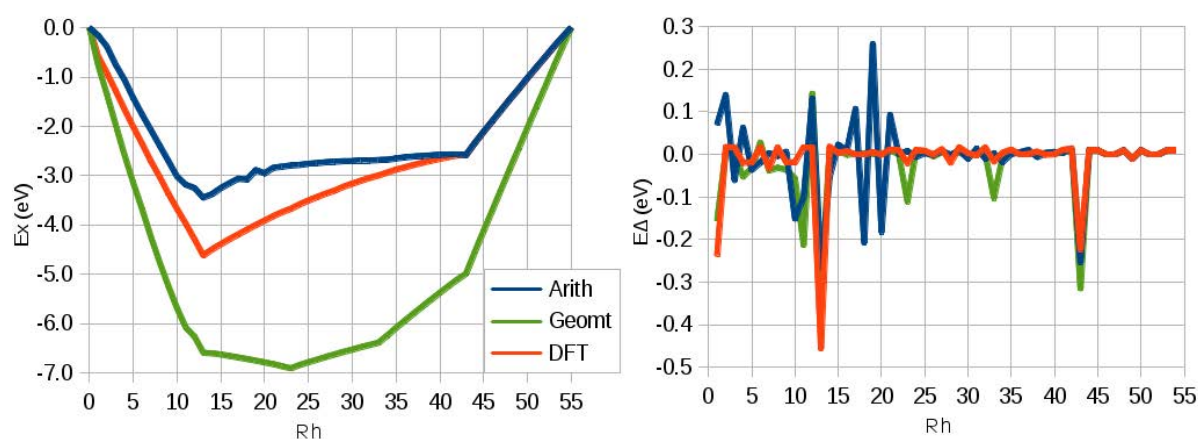


Figure 3-9 Variation in energy of the 55 atom clusters across the composition range. Left- excess energy, right- second difference energy.

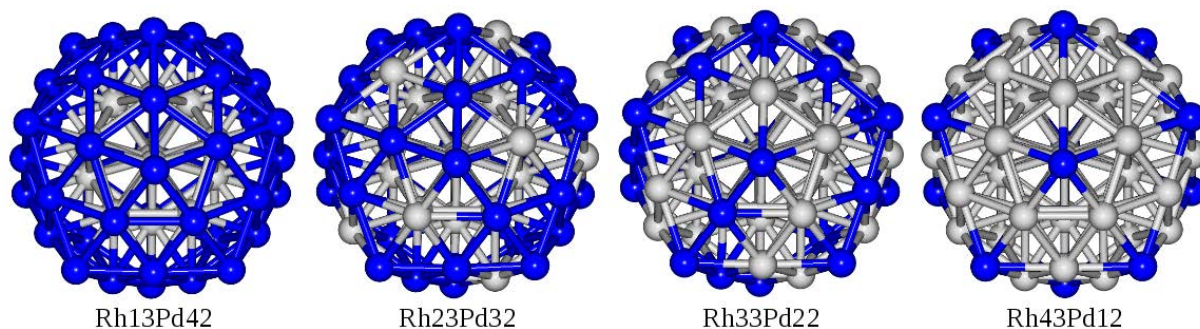


Figure 3-10 Structures corresponding to minima for the second difference energy with the geometric potential (figure 3-9).

3.4.4 98 Atom clusters

3.4.4.1 Genetic Algorithm

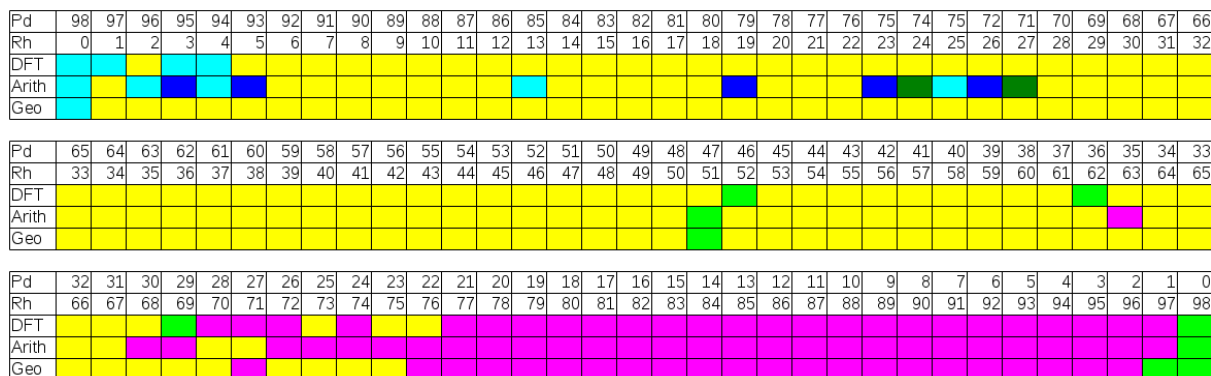


Figure 3-11 Different structures across the composition range for the 98 atom clusters for each potential, found using the Genetic Algorithm. Yellow- decahedra, magenta- icosahedra, cyan- FCC, blue- FCC-HCP, light green- Leary Tetrahedra (LT) and dark green- incomplete tetrahedral.

The 98 atom structures only exhibit shell closure for FCC and LT. Decahedral clusters have complete shell closure for 101 atoms. figure 3-11 shows that decahedral structures predominate over most of the composition range. At the rhodium rich end icosahedral clusters dominate. This mirrors what is found in the AuPd system(117). Interestingly the lowest energy structure for pure rhodium is the Leary Tetrahedron for all three potentials and as far as the author is aware this is not the case for any other metal. The lowest energy pure palladium structure was found to be a fragment of the FCC lattice. The LT structure was found to be the lowest energy structure for a few

compositions including $\text{Pd}_{46}\text{Rh}_{52}$, $\text{Pd}_{36}\text{Rh}_{62}$ and $\text{Pd}_{29}\text{Rh}_{69}$ for the DFT-fit potential, $\text{Pd}_{47}\text{Rh}_{51}$ for the arithmetic potential and $\text{Pd}_{47}\text{Rh}_{51}$ and $\text{Pd}_1\text{Rh}_{97}$ for the geometric potential. As with the previous structures, Pd preferentially occupies the surface or vertex sites.

3.4.4.2 98 Atom Symmetry Searches

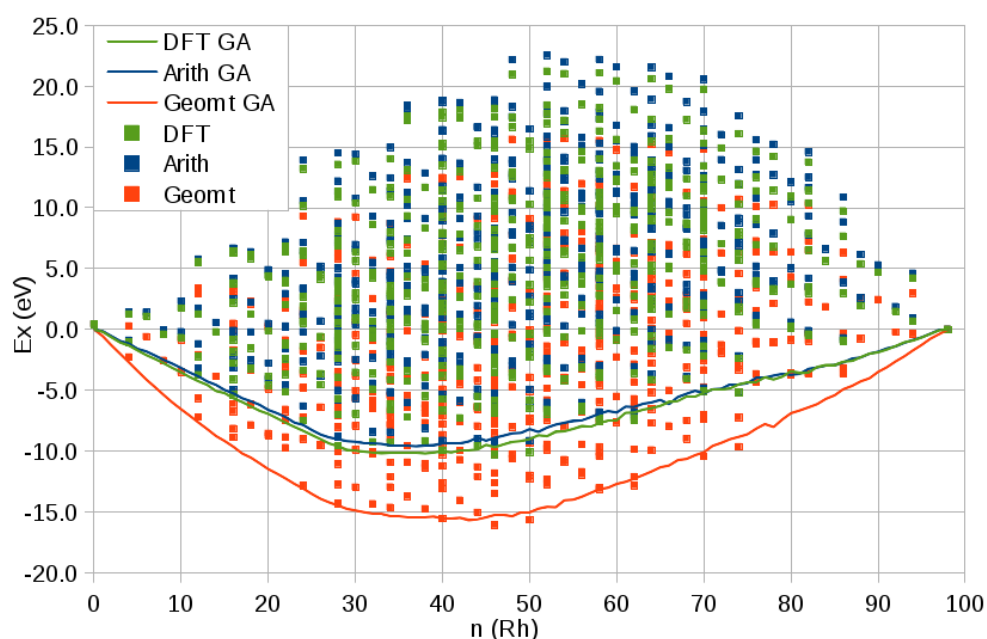


Figure 3-12 Excess energies of the structures generated with the GA (solid lines) compared with the all high symmetry LT structures. Each colour corresponds to a different potential.

The comparison between all the high symmetry LT clusters and the lowest GA energies is shown in figure 3-12. Many of these structures have positive E_x , which corresponds to $\text{Pd}_{\text{shell}}\text{Rh}_{\text{core}}$ structures, the opposite of the preferred geometry. However, some LT structures were found to be lower in energy than the previous best structures obtained by the GA.

3.4.4.3 Basin Hopping

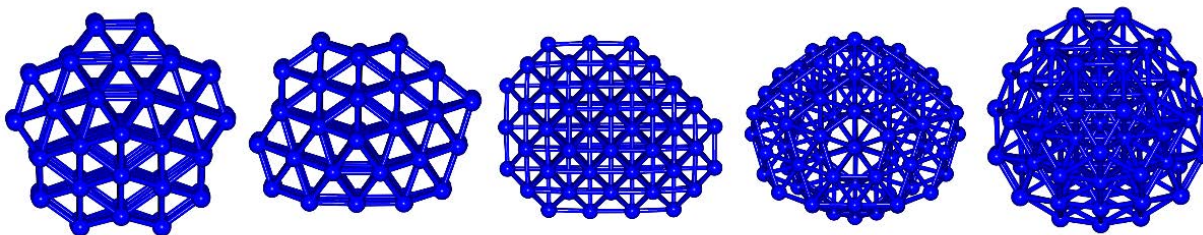


Figure 3-13 The five structures used for the BH algorithm. From left to right: Decahedra (1), Decahedra (2), FCC, icosahedra, leary tetrahedra

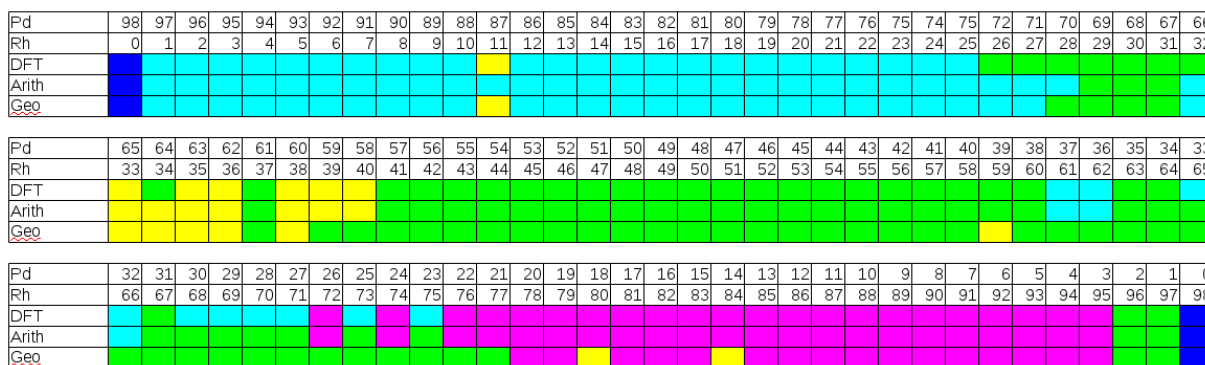


Figure 3-14 Different structures across the composition range for the 98 atom clusters for each potential, found using the basin hopping algorithm. Blue- pure clusters (FCC for Pd_{98} and LT for Rh_{98}), cyan- FCC, magenta- icosahedra, yellow- decahedra and green LT.

Using the structures from the GA, five different structures were selected for basin hopping runs across the PES. The structures selected were two different decahedral clusters, the Pd_{98} FCC cluster, the Leary Tetrahedra and an incomplete icosahedral cluster. These are shown in figure 3-13. The decahedral and icosahedral clusters were selected for further searching as they had been found across extensive parts of the composition range using the GA. The FCC and LT clusters were selected to see if lower energy structures could be found, as these structure was only rarely found by the GA. This is especially true for the LT clusters, as high symmetry searches had

found lower energy structure but keeping the symmetry limits structures to certain compositions.

The lowest energy structures found by the BH algorithm are shown in figure 3-14. As the basin hopping algorithm used in this work only involved swapping the positions of Rh for Pd atoms, the pure clusters were taken from the genetic algorithm. For the Pd rich clusters, the FCC structure is found to be lower in energy than the decahedral structure in most cases, contradicting what is found using the genetic algorithm. This could be because the FCC structure is in a narrow potential well on the PES and is therefore difficult to find using a GA. The BH algorithm here keeps the structure constant, so it only searches the bottom of the FCC well. In addition, the two structural motifs are similar in energy, separated by a few tenths of an electron volt, and increase the difficulty of the structural search. Decahedral structures are preferred from $\text{Rh}_{33}\text{Pd}_{65}$ to $\text{Rh}_{38}\text{Pd}_{60}$ - $\text{Rh}_{40}\text{Pd}_{58}$, depending on the potential. LT structures dominate the structural landscape around the decahedral structures. This again contradicts the GA results, again due to the narrow nature of the LT potential well, and it is known that the LT structure is challenging to find even using simpler potentials(123).

3.4.4.4 Combined Approach

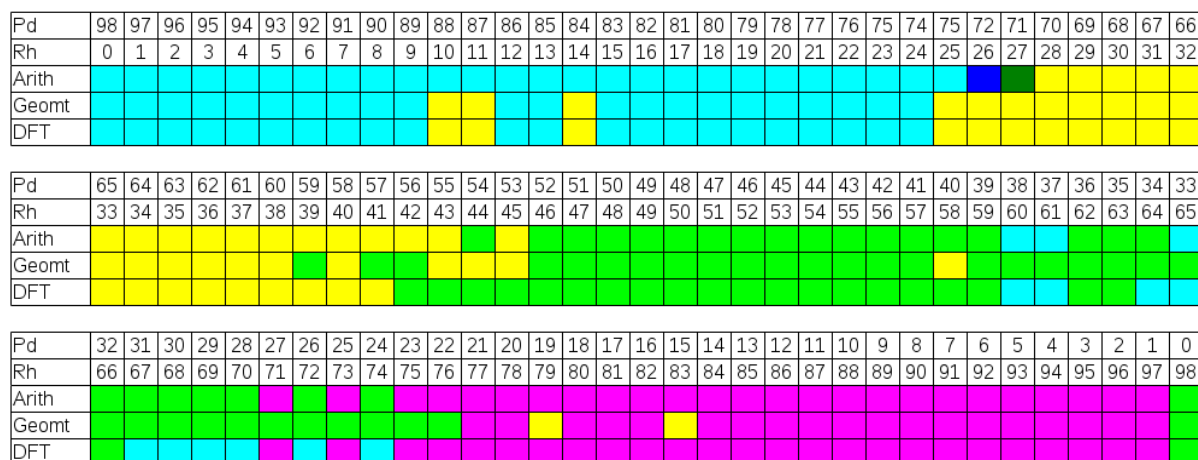


Figure 3-15 Different structures across the composition range for the 98 atom clusters for each potential, using symmetry searches, basin hopping and the genetic algorithm. Yellow- decahedra, magenta- icosahedra, cyan- FCC, blue- FCC-HCP, light green- Leary Tetrahedra (LT) and dark green- incomplete tetrahedral.

Figure 3-15 shows the lowest energy structures at each composition for the 98 atom clusters. At the Rh rich end of the composition spectrum, FCC clusters dominate up to $\text{Rh}_{24}\text{Pd}_{74}$. This shifts to a decahedral arrangement until between $\text{Rh}_{39}\text{Pd}_{59}$ to $\text{Rh}_{53}\text{Pd}_{45}$ to the LT structures. Icosahedral clusters dominate the rhodium rich part of the composition range. The GA had difficulty finding the LT structures and the FCC structures, although it also found the incomplete tetrahedral cluster and the FCC-hcp structure within the arithmetic potential ($\text{Rh}_{26}\text{Pd}_{72}$ and $\text{Rh}_{27}\text{Pd}_{71}$, respectively).

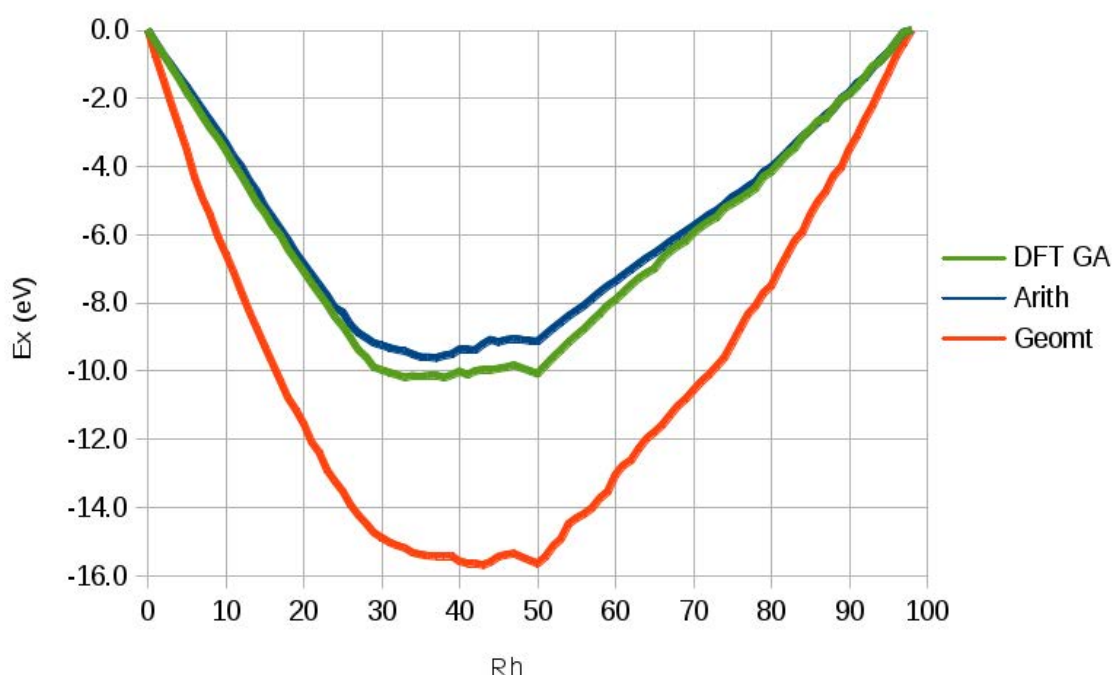


Figure 3-16 The excess energies for the lowest energy structures of the 98 atom clusters for all three potentials, using the lowest energy structure from the BCGA, BH and symmetry search methods.

Excess energies are shown in figure 3-16. The minimum at $\text{Rh}_{50}\text{Pd}_{48}$ corresponds to the LT structure with the Pd atoms on all the vertex sites. The other local minima in the curve correspond to the GM decahedral structures, which have fewer vertex sites than the LT.

3.5 Conclusions

We have studied different Gupta potentials for 34, 38, 55 and 98 atom clusters. The geometric potential exhibits poor fitting to DFT calculations, suffering from strong overbinding compared with DFT results. The arithmetic potential seems to be able to explore larger parts of the energy landscape, discovering the $\text{Rh}_4\text{Pd}_{30}$ C_3 tetrahedral cluster, the 38 atom Dh-lh structure and additional geometries that were not found with the geometric or DFT-fitted potential. This is ideal behaviour, as it gives a larger

range of clusters for further optimisation at a higher level of theory, making it more probable that the lowest energy structure will be found.

For cluster with 38 or 55 atoms, the TO structure and the icosahedra structures dominate the energy landscape across the entire composition range, due to the magic shell closure. This is not the case for 34 atoms clusters, resulting in different structural motifs across the composition range. Although the 98 atom clusters do have structural motifs that exhibit shell closure (namely the LT and FCC structures), these are difficult to find without using both GA and BH algorithms, probably due to the narrowness of the potential well for these structures and the broadness of the decahedral and icosahedral well. The GA specialises in finding different structural motifs, whereas BH is better at finding the correct homotop for a particular structure or composition. Further runs for the GA or BH may improve the global minima, but only at additional computational expense.

Due to the limitations of current computer hardware, it is not possible to study much larger clusters using the current version of the BCGA or the Basin hopping algorithm. The current iterations of these programs are serial, and parallelisation would increase the maximum size that can be studied. However, larger clusters can be generated by using symmetry equivalent shells and minimized rapidly, with cluster sizes up to 10,000 atoms (about 7Å across) achievable on current computer hardware.

Chapter 4- Chemisorption on Bimetallic Nanoparticles

4.1 Introduction

For hydrogen fuel cells, an ideal catalyst would have a thin single atom thin layer of expensive catalyst (for fuel cells this is normally platinum), with the rest of the nanoparticle made of a cheaper metal. However, recent work has shown that for many systems nanoparticles undergo structural inversion under different ambient conditions (30, 31, 105). For example, in vacuum AuPd particles adopt a $\text{Pd}_{\text{core}}\text{Au}_{\text{shell}}$ arrangement. However, when the particles are exposed to the air, the particles undergo core-shell inversion. Also, heating the particles using an electron beam resulted in mixed nanoparticles.

Chemisorption has been used to affect the surface of some bimetallic alloys. Andersson et al.(30) have shown experimentally that carbon monoxide can bring a copper under layer to the surface. Interestingly, the Cu does not bind to the CO directly, but surrounds the Pt sites of the surface. Theoretical investigations have been taken on AuPd with CO and O, and found it is more energetically favourable to have Pd on the surface with CO bound to the Pd over Au.

This behaviour becomes more pronounced in the nanoscale regime, as the number of surface atoms greatly increases. Also other effects play a part in the morphology of clusters which are not an issue in the bulk. For example, DFT

calculations have shown that the cluster morphology changes as CO or atomic H is added to the surfaces of Pd, Au and Pt 38 atom nanoparticles. Experimental results have shown that RhPd undergoes structural inversion depending on the ambient atmosphere(105). In addition, they find the process is partly reversible, which the authors suggest could be useful in so called ‘smart catalysis’. This is where the nanoparticles perform one reaction under certain conditions, and create a completely different set of products under different conditions.

We investigated the binding of carbon monoxide, atomic hydrogen and atomic oxygen on many different bimetallic clusters, to find how the homotop energy landscape is affected in the presence of ligands.

4.2 Methodology

4.2.1 Cluster Geometry

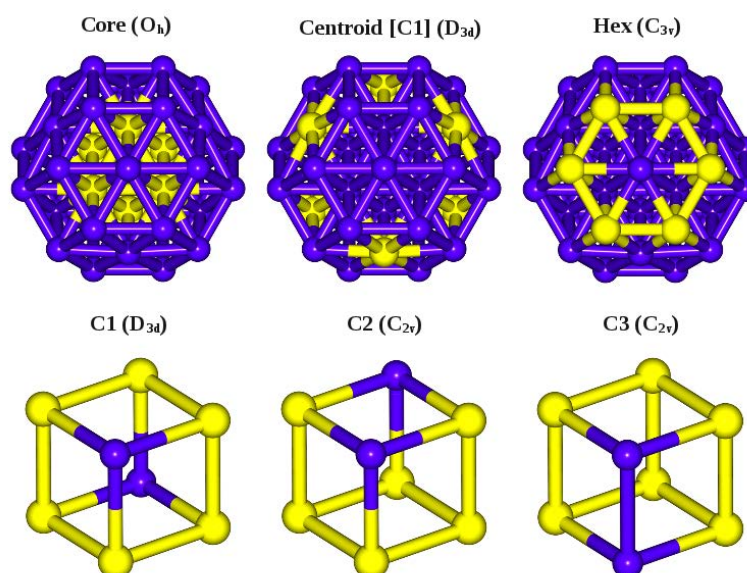


Figure 4-1 (Top) the three different structures studied. From left to right- core, centroid (cent) and hex. (Bottom) The eight centroid sites make up a cube, and the three different homotops of these structures are shown. The symmetry point group of the respective cubes are given in brackets.

A 38-atom truncated octahedron (TO), see figure 4-1, was chosen as a model for the chemisorption on bimetallic nanoparticles, due to the high symmetry of the parent TO structure (O_h). The CO, H and O were bound to all non-symmetrically equivalent (111) centroid sites in the atop position. It should be noted that this may not be the most energetically preferred site, although the energetic trends between different clusters can be compared directly, whereas the 2 fold 'bridge' sites and 3 and 4 fold hollow sites may not be stable (particularly for CO on gold clusters, see Chapter 5-). Multiple adsorption of H and CO on the TO and other 38-atom clusters of Pd, Pt, and Au have previously been reported (88, 117).

A composition of A_6B_{32} was used, along with the inverse composition (B_6A_{32}) as this corresponds to the perfect core-shell structure for the 38 atom TO structure. Four different homotops were studied:

4.2.1.1 Core

A core-shell configuration, in which the 6 A atoms form an octahedral core surrounded by a shell of 32 B atoms. This homotop has the full O_h symmetry of the parent TO.

4.2.1.2 Hex

The 6 A atoms form a hexagonal ring surrounding the centroid of one of the (111) facets, mimicking the local structure found by Andersson et al. on the (111) CuPt surface after CO adsorption. This homotop has C_{3v} symmetry.

4.2.1.3 Centroid

The 6 A atoms occupy 6 of the 8 (111) centroids. The 8 (111) centroids define a cube and there are three ways in which the 6 A and 2 B atoms can decorate a cube, as shown in figure 4-1: (a) C1, the 2 B atoms are arranged across a body-diagonal of the cube (i.e., diametrically opposed)—this homotop has D_{3d} symmetry; (b) C2, the 2 B atoms are arranged across a face-diagonal of the cube—this homotop has C_{2v} symmetry; (c) C3, the 2 B atoms are arranged along an edge of the cube—this homotop also has C_{2v} symmetry. The three centroid homotops (C1–C3) have identical distributions of A–A, A–B, and B–B bonds and are expected to have very similar energies. The C1 and C2 isomers were compared for PdPt and CuPt systems.

4.2.2 Adsorption structures

The three ligands investigated were CO and atomic H for investigating reducing conditions and atomic O for oxidizing conditions. For CO and H ligands on AuPd, CuPt and PdPt, energies for all non-symmetry equivalent atop sites for the central atom in the (111) face were found. The energies for binding to the C2 structure are not shown, due to the similarities between the C1 and C2 energies. For all O-bound structures and all RhPd homotops, all atop (111) sites were investigated excluding the hex2-4 structures. These structures, with CO as an example, are shown in figure 4-2. Relative energies were calculated relative to the lowest energy homotop.

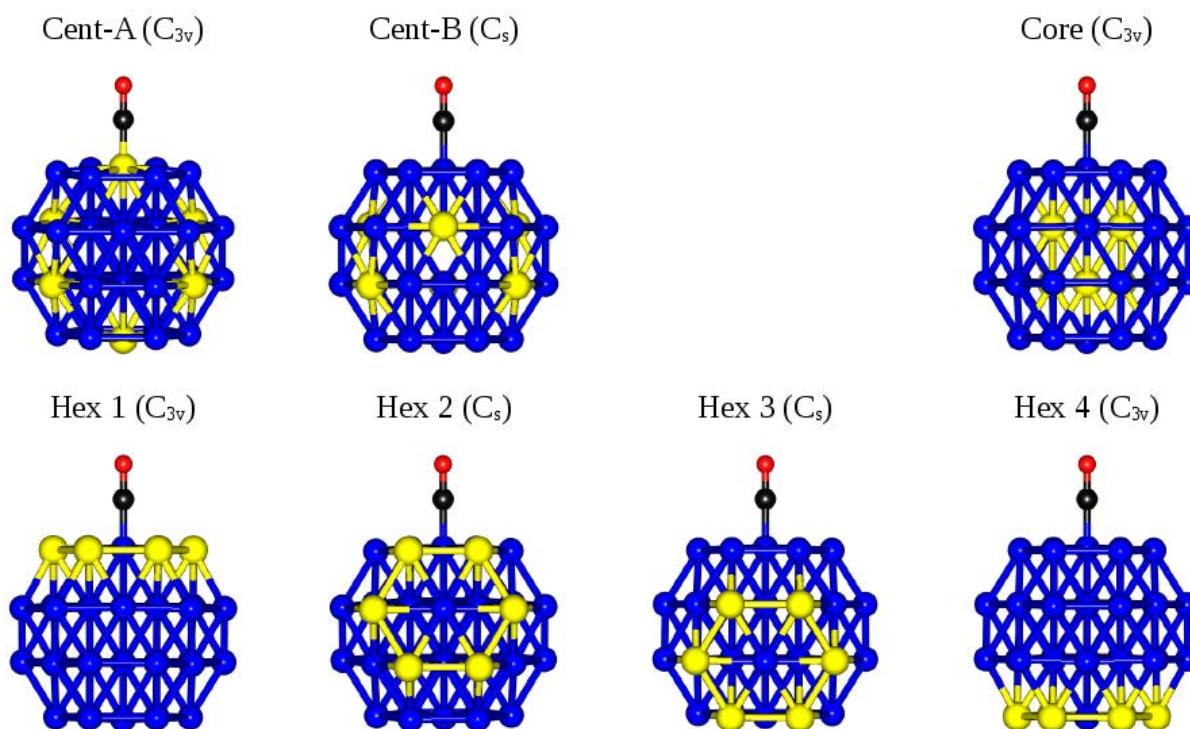


Figure 4-2 Adsorption sites studied in this work, with carbon and oxygen shown in black and red, respectively. Atomic hydrogen and oxygen are adsorbed to the same sites. The point group of each cluster is shown in brackets.

When multiple ligands were placed on the cluster, symmetry was kept as high as possible to lower the computational time so not all atop adsorption sites were considered. For the core-shell structure, one, two, four, six and eight adsorbates were considered, and for the centroid structures one, two, four and six were considered. The hex structure allows only four adsorbates to be added, with three surrounding the central hexagon of minority A atoms and one bound to the atom in the center of the hexagon. This structure has C_{3v} symmetry. The 3 adsorbate structure which also has C_{3v} symmetry was also considered. Not all the calculations were performed at the highest symmetry, as the highest point group was not detected by NWChem. These structures are shown in figure 4-3.

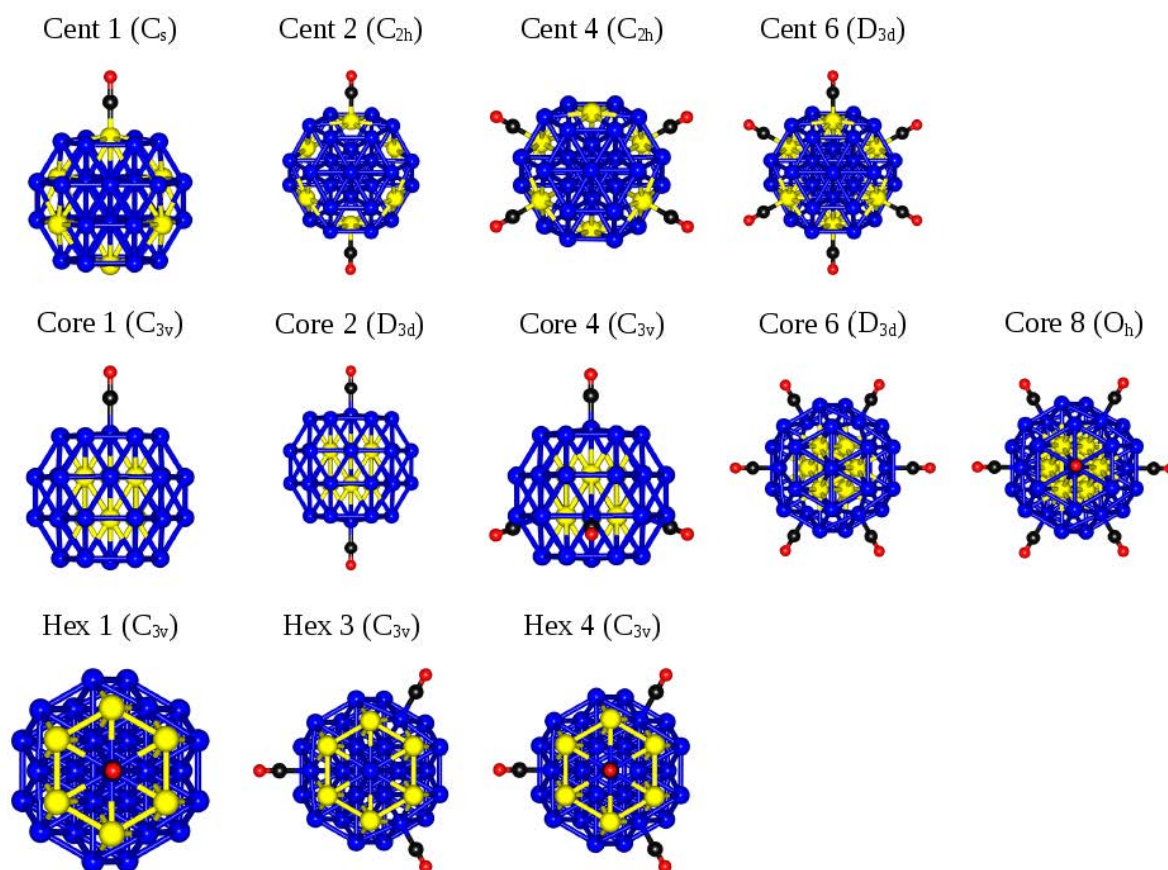


Figure 4-3 the adsorption sites studied for the multiple ligand clusters, with the point group for each structure shown in brackets.

4.2.3 DFT Calculations

Calculations were performed using the NWChem 5.1 Quantum chemistry package(85). The PW91 GGA exchange correlation function was used(64) with LCAO basis set using Gaussian type Orbitals paired with relativistic effective core potentials and coulomb fitting basis sets. A double zeta basis set was used for the geometry optimisation, followed by a single point calculation at the triple zeta level to improve accuracy. The double zeta basis sets used were: Pd (7s6p5d1f)/[5s3p3d1f], Pt (7s6p5d1f)/[6s3p3d1f], Au (7s6p5d1f)/[6s3p3d1f], Cu (8s7p6d1f)/[6s5p3d1f], Rh (7s6p5d)/[5s3p3d], H (5s1p)/[3s1p], C (11s6p1d)/[5s3p1d] and O (11s6p1d)/[5s3p1d].

A Gaussian smearing energy of 0.14eV was used in the calculations, to assist convergence. This improves convergence by partially occupying orbitals that are close in energy to the Fermi level. This is required as the molecular orbitals are close in energy, so choosing the lowest energy orbital between multiple competing orbitals is either difficult or impossible, particularly in high symmetry clusters.

It is worth noting that it is difficult to find the correct binding site for CO on Pt using DFT calculations (129), with relativistic effects (including spin-orbit coupling) playing a large role in the energy landscape(130). However, this work is focused on trends in binding energy between the different metals and these relationships should hold even when the 'incorrect' binding site is used. For example, CO prefers to occupy the 3-fold hollow site on Pd (131), whereas only atop sites have been studied in order to reduce the number of calculations.

The Basis Set Superposition Error (BSSE) was also calculated for pure copper clusters. As an adsorbate is on the surface, additional basis functions are included in the calculation. This artificially increases the binding energy. The BSSE was found by comparing the energy of the bare cluster with the energy of the same cluster with CO, H or O 'ghost' atoms on the surface. These ghost atoms contain no electrons but do have the basis function of their respective element.

4.2.4 Energy calculations

For the bare clusters and single adsorbate structures, relative energies were calculated relative to the lowest energy structure. For the multiple adsorbate clusters, the number of atoms is no longer constant, so another method is used. First, the absolute relative energies are calculated using equation 4-1

$$E_{abs}^{rel} = E(A_6B_{32}(CO)_n) - xE(CO) - \min(E(A_6B_{32}(CO)_x)) \quad 4-1$$

Where $E(A_6B_{32}(CO)_x)$ is the energy of the cluster with a number of CO molecules bound to the surface, $E(CO)$ is the energy of the CO molecule (found to be -113.3139 Hartrees) and x is the number of CO molecules adsorbed to the surface. $\min(E(A_6B_{32}(CO)_n))$ is the lowest energy isomer with the composition A_6B_{32} and any number of CO molecules bound to the surface. These energies were then shifted relative to the core-shell energies, as shown in figure 4-4. A line is fitted to the core-shell structures, and all structures were shifted relative to this line. The core-shell structures were selected as they had the largest number of points.

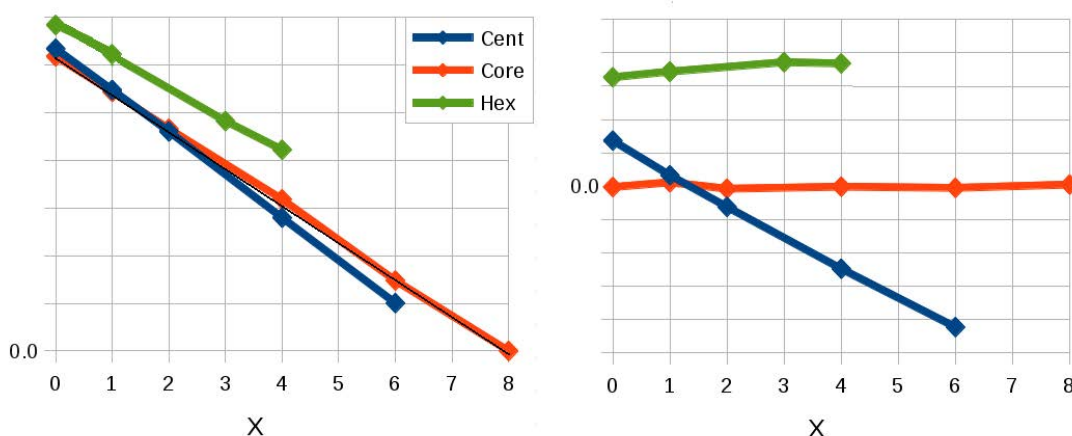


Figure 4-4 A diagram showing how the relative energies were calculated for the multiple adsorption clusters. The left hand diagram shows the relative energies, as calculated using equation 4-1, of different homotops with different numbers of ligands (x axis) on them. A straight line is fitted to the core-shell structure (thin black line fitted to the red line). All the points are then shifted relative to this line, resulting in the diagram on the right.

4.3 Results

4.3.1 Bare clusters

Before comparing clusters with ligands attached, it is necessary to analyse the energetic of the bare clusters. These are shown in figure 4-5.

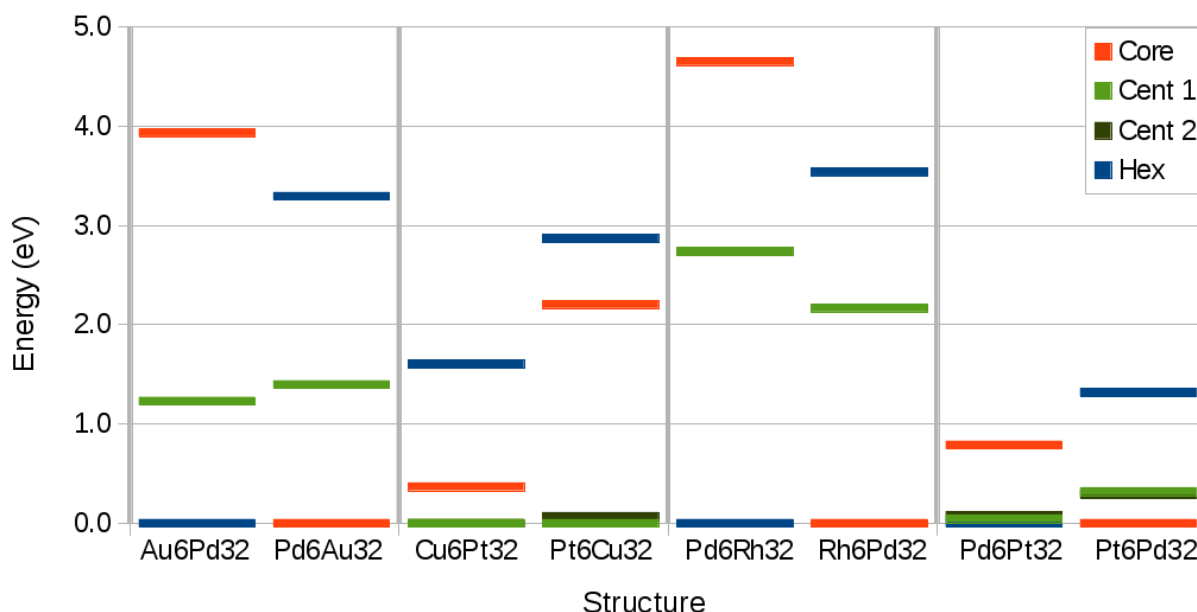


Figure 4-5 Relative energies in eV of different homotops for the bare A_6B_{32} and B_6A_{32} clusters. Gray lines separate different bimetallic compositions.

4.3.1.1 AuPd Clusters

For Au_6Pd_{32} , the energetic ordering is $E_{\text{hex}} < E_{\text{cent}} < E_{\text{core}}$, and the inverse is true for the Pd_6Au_{32} structures. Au prefers to occupy the hex sites on the truncated octahedron, followed by the centroid surface sites and the core is the highest energy structure. Au has a lower surface ($96.8 \text{ meV}\text{\AA}^{-2}$) and cohesive energy (3.81 eV) compared to Pd in the bulk ($131 \text{ meV}\text{\AA}^{-2}$ and 3.89 eV). This is particularly pronounced for Au_6Pd_{32} , where the $Au_{\text{core}}Pd_{\text{shell}}$ structure is 3.9eV higher in energy than the hex structure. Au has the larger atomic radius ($Au=2.88 \text{ \AA}$, $Pd=2.75 \text{ \AA}$) so the $Au_{\text{core}}-Pd_{\text{shell}}$ induces strain in the TO structure, which geometrically has bond lengths which are identical. Experimentally, bare AuPd alloys show an increased amount of Au on the surface relative to the bulk composition for polycrystalline films and single crystal foils.

This compares well with theoretical work by Yuan, Gong and Wu(132), who found that the corner site was the least preferred site for Pd on Au₅₅ and Au₉₈ by 0.267 eV and 0.12 eV, respectively.. They also found that Pd tends to agglomerate on the surface, although they did not investigate Pd atoms in the core.

4.3.1.2 PdPt

PdPt has similar characteristics to the AuPd system, with the same energetic ordering as AuPd with the Pt replacing Pd and Pd replacing Au. In this system, Pd has the lower surface energy (by 20 meVÅ⁻²) and Pt has the much higher cohesive energy (5.84 eV/atom for Pt). The energy range is much narrower for PdPt and this can be explained by the ratio between the bulk surface and cohesive energies. The cohesive energy difference between PdPt is larger for PdPt ($E_{\text{coh}}(\text{Pt})/E_{\text{coh}}(\text{Pd})= 1.5$, $E_{\text{coh}}(\text{Pd})/E_{\text{coh}}(\text{Au})= 1.02$). However, the surface energy's ratio is smaller ($E_{\text{surf}}(\text{Pt})/E_{\text{surf}}(\text{Pd})= 1.15$, $E_{\text{surf}}(\text{Pd})/E_{\text{surf}}(\text{Au})= 1.35$). As these are small clusters, 32 of the 38 atoms are on the surface, increasing the importance of this term. For larger PdPt TO structures, an onion like structure is adopted. In addition, due to the similarity of the atomic radii, there is minimal strain induced effects.

For the centroid structures, both the C1 and C2 isomers were studied. The difference in energy between the two structures was minimal, with an energy gap of 0.03eV for Pd₆Pt₃₂ and Pt₆Pd₃₂. The difference can probably be attributed to small differences in the convergence of the geometry or electronic states due to the different symmetry.

4.3.1.3 RhPd

RhPd is also qualitatively similar to AuPd and PdPt, although with larger energy gaps between structures than AuPd. Rh has the higher surface energy ($168 \text{ meV}\text{\AA}^{-2}$). The ratio between the surface energies is 1.32, similar to AuPd but the cohesive energy difference is much larger, ($E_{\text{coh}}(\text{Rh})/E_{\text{coh}}(\text{Pd})$ equals 1.46). Therefore Rh atoms prefer the core sites with Pd preferentially occupying the hex sites.

4.3.1.4 CuPt

CuPt differs from all the above systems, with the ordering of centroid < core < hex for both $\text{Cu}_6\text{Pt}_{32}$ and $\text{Pt}_6\text{Cu}_{32}$. This is despite Cu having the lower surface energy ($114 \text{ meV}\text{\AA}^{-2}$ for Cu and $155 \text{ meV}\text{\AA}^{-2}$ for Pt) and Pt having the larger cohesive energy (5.85 eV for Pt over 3.54 eV for Cu). This can be explained by the strength of the Cu-Pt bond. PtPd and RhPd are both immiscible in the bulk, and AuPd has a few ordered phases at Au_1Pd_3 , Au_1Pd_1 and Au_3Pd_1 compositions. The CuPt phase diagram has many ordered phases, suggesting strong bonding. In the 38 atom TO, the centroid structure has the greatest number of mixed Cu-Pt bonds, as shown in Table 4-1.

	Core	Centroid	Hex
A-A	12	0	6
A-B	48	54	24
B-B	84	90	114

Table 4-1 The number of nearest neighbour bonds for each structure, for each cluster, with a composition of A_6B_{32} .

As with the PdPt system, two different centroid structures were optimised and the energy gap between them was still small (0.001 eV for $\text{Cu}_6\text{Pt}_{32}$ and 0.07 eV for $\text{Pt}_6\text{Cu}_{32}$).

4.3.2 Clusters Bound To Single H, CO and O Ligands

4.3.2.1 Pure Clusters

The interaction energies of the atop binding sites are shown in Table 4-2. Due to the different interaction energies, binding to different elements should be favoured, which could result in changes in energetic ordering of the investigated structures. However the local structural environment may affect the interaction energies, resulting in further changes in energetic ordering. All the structures converged upon the atop geometry.

As a large TZVP basis was used for the final electronic optimisation stage of the calculation, the BSSE shows only a small gain in energy due to the additional basis functions. The hydrogen ligand has a lower BSSE energy than oxygen by 0.019eV, probably due to the short copper-hydrogen bond (1.5 Å, compared with 1.9 Å for Cu-O and 1.8 Å for Cu-CO).

	Au₃₈	BSSE	Cu₃₈	Pd₃₈	Pt₃₈	Rh₃₈
CO	-0.217	-0.038	-0.350	-1.330	-1.895	-1.672
H	-1.997	-0.034	-1.885	-2.391	-2.926	-2.296
O	-1.980	-0.013	-3.004	-2.817	-3.023	-3.352

Table 4-2 The adsorption energies (in eV) of CO, atomic H and O on the atop site of the centroid atom for each 38 atom cluster. Cu₃₈ BSSE shows the Basis Set Superposition Error (BSSE) for O, CO and H basis sets a copper cluster.

4.3.2.2 AuPd

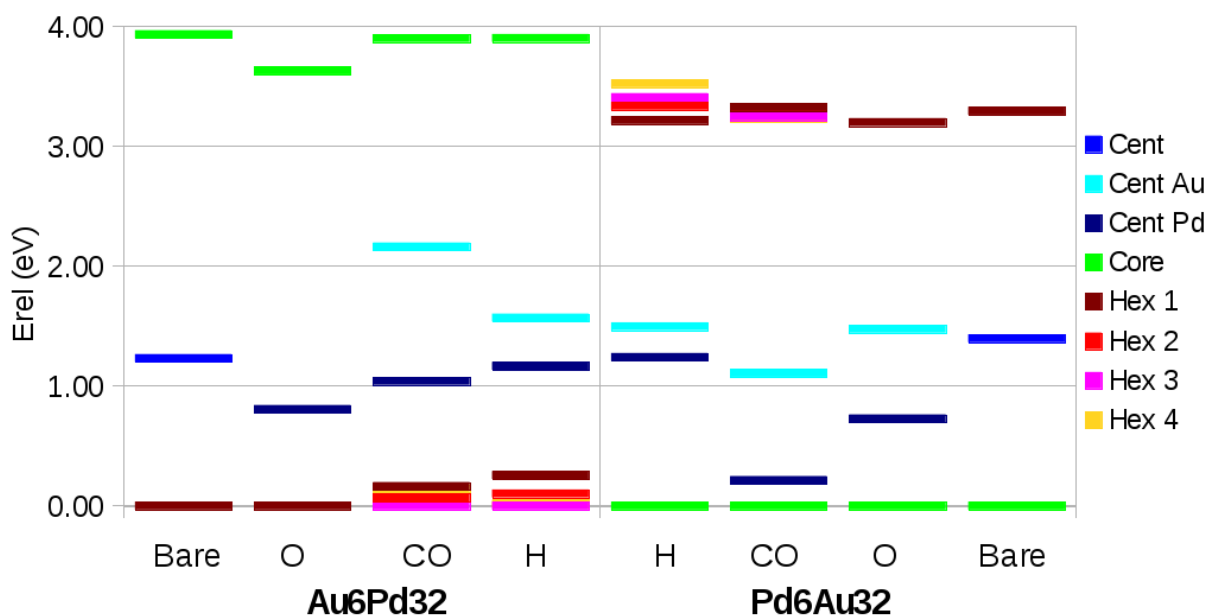


Figure 4-6 Relative energies of $\text{Au}_6\text{Pd}_{32}$ (left) and $\text{Pd}_6\text{Au}_{32}$ (right) clusters with and without ligands. The far left and right columns show the relative energies of the bare $\text{Au}_6\text{Pd}_{32}$ and $\text{Pd}_6\text{Au}_{32}$ clusters, respectively. The 6 central columns show the relative energies of the cluster with (from centre) H, CO and O ligands bound to it. The $\text{Au}_6\text{Pd}_{32}$ “Cent Au” energy is not shown, as this structure was not a local minima.

The relative energies of AuPd clusters with and without ligands are shown in figure 4-6. CO, H and O all have higher interaction energies with Pd rather than Au which results in changes to the energy landscape of the clusters. In the bulk, CO binds to the Pd (111) surface with an interaction energy of 1.47eV, whereas CO binds only weakly to the Au(111) surface(133). For the cases where the ligand is bound to the majority atom, in either $\text{Au}_6\text{Pd}_{32}$ or $\text{Pd}_6\text{Au}_{32}$, the relative energies remain qualitatively constant, implying the interaction energies of ligands to Au or Pd remain fairly constant despite changing the local environment. Small changes are seen in the hex structures, which are discussed below. However, binding to the minority atoms does affect the relative energies. This is shown clearly with the centroid structures, with Pd- bound species lower in energy. Hydrogen shows the smallest splitting of 0.33eV,

followed by oxygen (0.75eV) and CO (1.0eV), probably due to the weakness of CO binding to gold. This is important for $\text{Au}_6\text{Pd}_{32}\text{CO}$, as the energy gap between the core-shell and the centroid structure narrows from 1.4eV to 0.2eV.

Different hex structures were investigated for the CO and H bound cases. For the low energy $\text{Au}_6\text{Pd}_{32}$ hex structures, the least stable hex structure was the hex-1 structure for both H and CO binding. The can be compared with bulk calculation by

4.3.2.3 PdPt

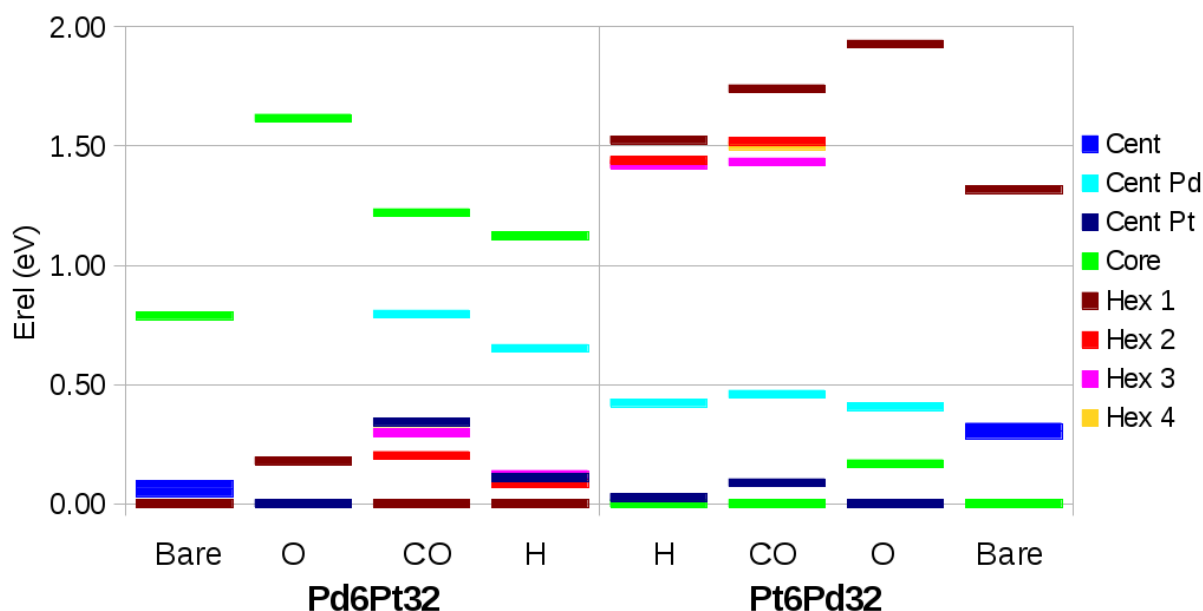


Figure 4-7 Relative energies of $\text{Pd}_6\text{Pt}_{32}$ (left) and $\text{Pt}_6\text{Pd}_{32}$ (right) clusters with and without ligands. The far left and right columns show the relative energies of the bare $\text{Pd}_6\text{Pt}_{32}$ and $\text{Pd}_6\text{Au}_{32}$ clusters, respectively. The 6 central columns show the relative energies of the cluster with (from centre) H, CO and O ligands bound to it.

It can be seen from figure 4-7 that energetic inversion is achieved between the centroid and core-shell structure for $\text{Pt}_6\text{Pd}_{32}\text{O}$, and for hex to centroid structure for $\text{Pd}_6\text{Pt}_{32}\text{O}$.

It can be seen from figure 4-7 that CO, H and O bind more strongly to Pt than for Pd, with the effect most noticeable in the oxygen adsorbed case with a centroid

splitting energy of 1.1eV for $\text{Pd}_6\text{Pt}_{32}\text{O}$ and 0.4eV for $\text{Pt}_6\text{Pd}_{32}\text{O}$. The splitting is large enough that energetic inversion is seen between the centroid and hex structure for $\text{Pd}_6\text{Pt}_{32}\text{O}$ and the core-shell structure for $\text{Pt}_6\text{Pd}_{32}\text{O}$. For the $\text{Pt}_6\text{Pt}_{32}\text{O}$ systems, the splitting energy of the centroid structures is always smaller than the Pt majority case as Pd- ligand bonding is weakened by surface Pt atoms, and Pd strengthens Pt-ligand interactions.

It is known that relativistic effects have a strong effect on the binding energy of Pd and Pt. If relativity is not taken into account, Philipsen et al. found that CO binds more strongly to Pd than to Pt by 0.19eV(78). This changes to Pt having the stronger interaction energy by 0.21eV for scalar relativity and to 0.1eV when full relativistic effects are included.

4.3.2.4 CuPt

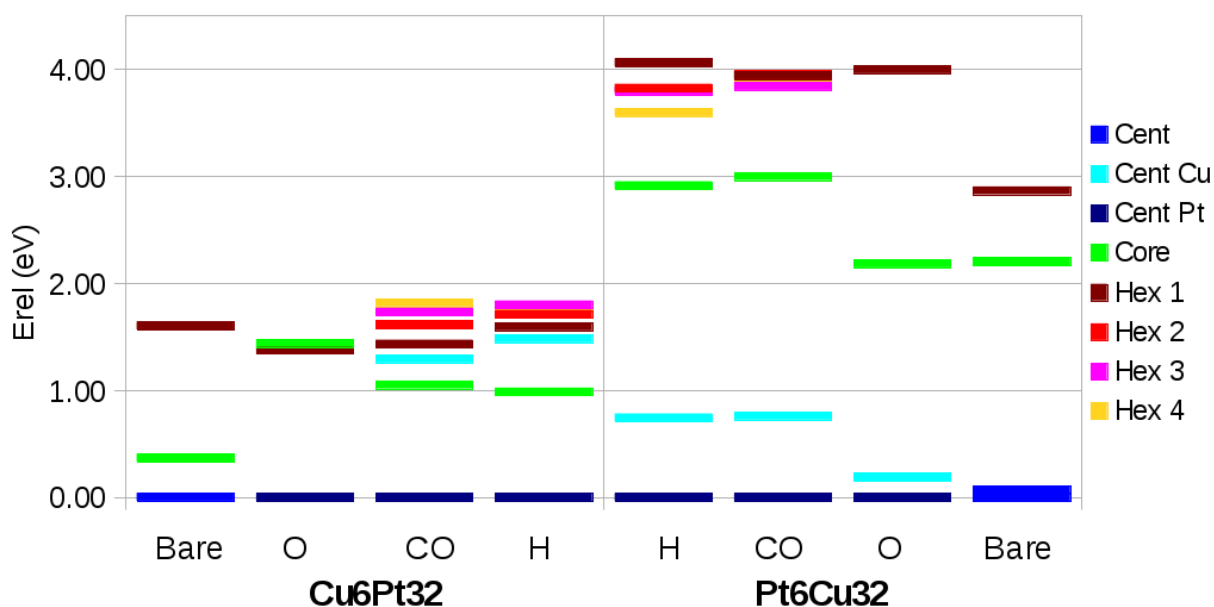


Figure 4-8 Relative energies of $\text{Cu}_6\text{Pt}_{32}$ (left) and $\text{Pt}_6\text{Cu}_{32}$ (right) clusters with and without ligands. The far left and right columns show the relative energies of the bare $\text{Cu}_6\text{Pt}_{32}$ and $\text{Pt}_6\text{Cu}_{32}$ clusters, respectively. The 6 central columns show the relative energies of the cluster with (from centre) H, CO and O ligands bound to it.

Figure 4-8 shows the relative energies for CO, O and H bound to $\text{Cu}_6\text{Pt}_{32}$ and $\text{Pt}_6\text{Cu}_{32}$. Cu binds with more weakly to all the ligands studied than Pt, and splitting of the centroid structure is observed, depending on the binding site. The splitting of the centroid homotop is 1.3 eV for CO, 1.5eV for H and 1.2eV for O. In the bulk, the atop adsorption energies for Cu(111) and Pt(111) are 0.5eV and 1.5eV respectively. In addition, all $\text{Cu}_6\text{Pt}_{32}$ structures see a destabilisation of the core-shell geometry, indicating that Cu surface atoms are preferred to having Cu in the core by between 1.0-1.4eV depending on the ligand. This is further confirmed by considering the hex structures. The hex structures have an energy span of 0.4eV for CO and an energetic ordering of $\text{hex1} < \text{hex2} < \text{hex3} < \text{hex4}$. The hex structures for the H ligands have a smaller energy range of 0.2eV, and a similar ordering to the CO structures, although the hex 4 structure is 0.028eV lower in energy than the hex3 structure, probably due to numerical error. For oxygen on $\text{Cu}_6\text{Pt}_{32}$, structural inversion occurs between the core-shell and hex structure, due to the strength of the O-Pt bond.

These results can be compared to work on PtCu (111) surface and subsurface alloys by Andersson et al. (30). Adding CO to Pt with a Cu subsurface leads to Cu atoms migrating to the surface, resulting in an ordered Cu hexagonal lattice surrounding isolated Pt atoms. The adsorption energy increases by 0.65eV after this rearrangement, with the surface segregation of Cu being endothermic by between 0.3 to 0.4 eV. In addition, Knudsen et al. also investigated CO on PtCu near surface alloys. However, they only investigated low Cu surface concentration, as they had to anneal the alloy to acquire a flat (111) surface and Cu diffused into the bulk of the material(134). Despite this, the energy of the hex is still 1.4eV higher in energy than the lowest centroid structure. This may change if further ligands are added.

4.3.2.5 RhPd

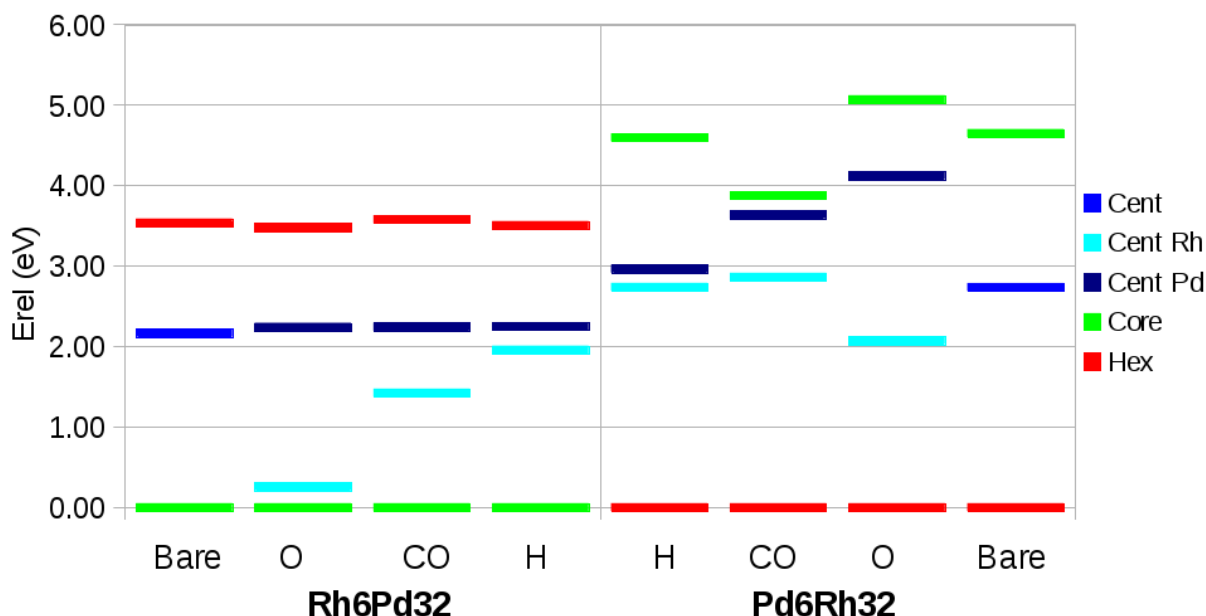


Figure 4-9 Relative energies of Rh₆Pd₃₂ (left) and Pd₆Rh₃₂ (right) clusters with and without ligands. The far left and right columns show the relative energies of the bare Rh₆Pd₃₂ and Pd₆Rh₃₂ clusters, respectively. The 6 central columns show the relative energies of the cluster with (from centre) H, CO and O ligands bound to it.

Figure 4-9 shows the relative energies of the RhPd clusters. Rh binds more strongly to all the species studied, resulting in the splitting of the centroid structures as seen in the other systems. For Rh₆Pd₃₂, the energy gap between the cent-Rh structure and the core-shell structures decreases from 2.2eV to 0.2 eV. The energy gap is larger with CO (0.5 eV) or H (0.2 eV) on the surface compared with atomic oxygen. In all cases, the ligands have a stronger binding energy to the Rh over the Pd. However, the difference in energy between Rh₃₈-X and Pd₃₈-X is only 0.04eV when X=H, 0.34eV where X=CO and 0.53eV when X=O. Additionally the surface energy will increase this energy difference as well, as the metal atom is now bond to the ligand so contributes less to the surface energy. For Rh₆Pd₃₂, the energies differences

between the core-shell, centroid-Pd and Hex structure remain constant, whereas for $\text{Pd}_6\text{Rh}_{32}$ the trend is less clear.

4.3.3 Multiple Adsorption

4.3.4 AuPd

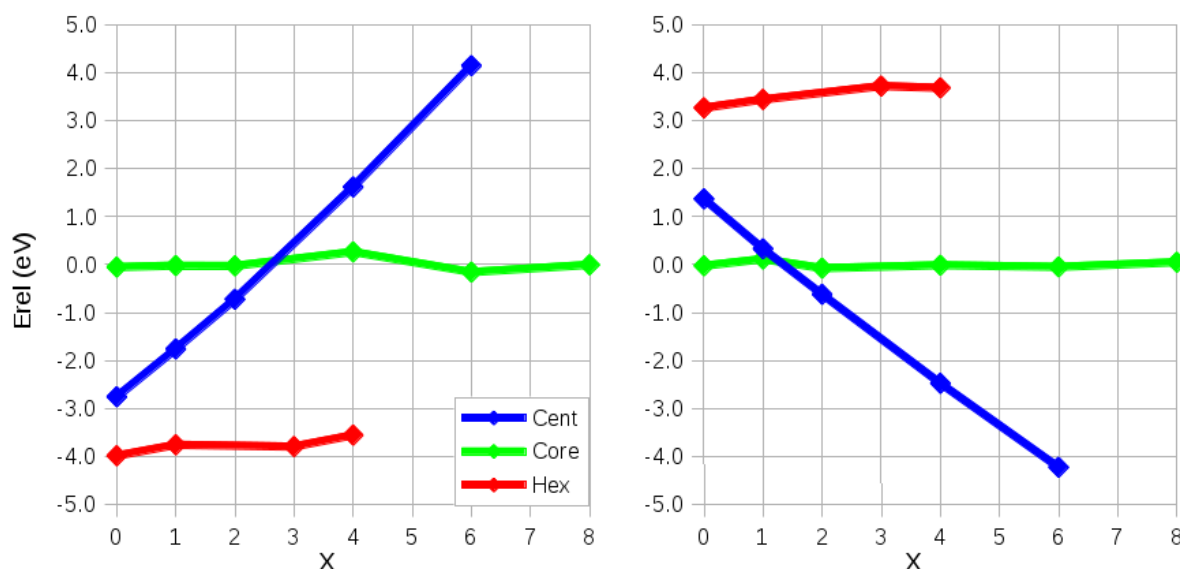


Figure 4-10 Relative energies of multiple CO molecules on (left) $\text{Au}_6\text{Pd}_{32}$ and (right) $\text{Pd}_6\text{Au}_{32}$ clusters. X denotes the number of CO molecules bound to the cluster.

Figure 4-10 shows the relative energies of multiple CO molecules on the surface of $\text{Au}_6\text{Pd}_{32}$ and $\text{Pd}_6\text{Au}_{32}$. For $\text{Au}_6\text{Pd}_{32}$, the hex structure remains the lowest energy structure, although energetic crossing occurs between the centroid and core structures after two CO molecules are added to the surface. For the $\text{Pd}_6\text{Au}_{32}$ cluster, energetic inversion between the centroid and core structures occurs as a second CO molecule is added. This is in agreement with results by Shan et al, who used DFT calculations on surfaces to show Pd segregates to the surface.

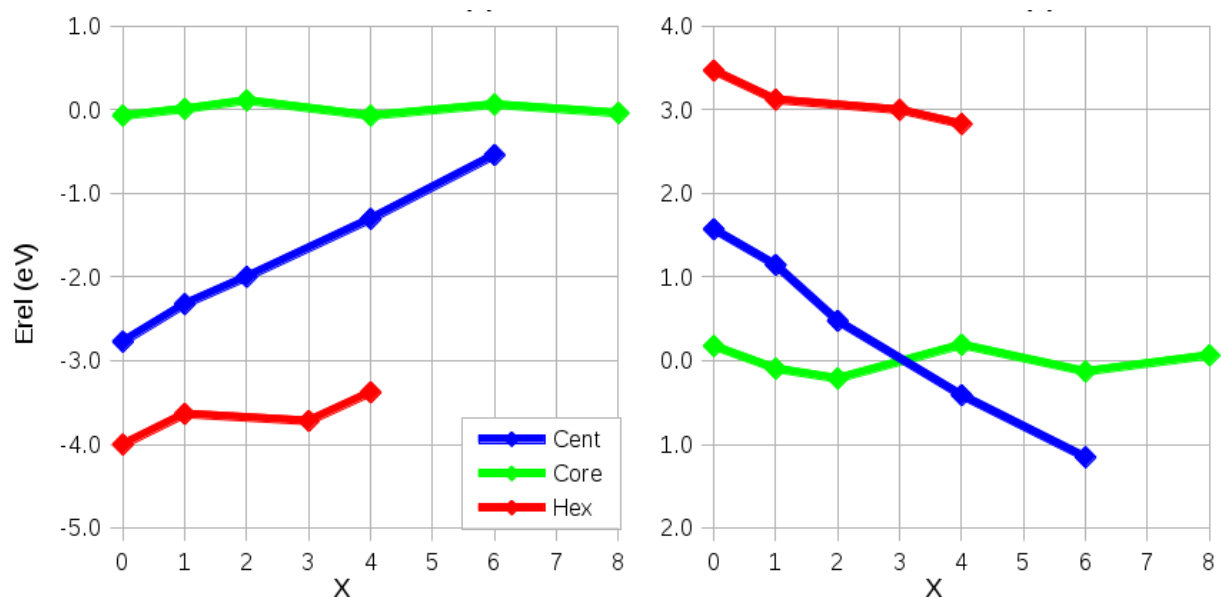


Figure 4-11 Relative energies of multiple H atoms on (left) Au₆Pd₃₂ and (right) Pd₆Au₃₂ clusters. X denotes the number of H atoms on the cluster

Due to the smaller energy gap between the interaction energies of Au-H and Pd-H compared with Au-CO and Pd-CO, (0.39 eV compared with 1.13 eV) energetic inversion does not occur with H on Au₆Pd₃₂, as shown in figure 4-11. It does occur between the centroid and core homotops for Pd₆Au₃₂, although only after four H atoms are added to the cluster.

4.3.5 PdPt

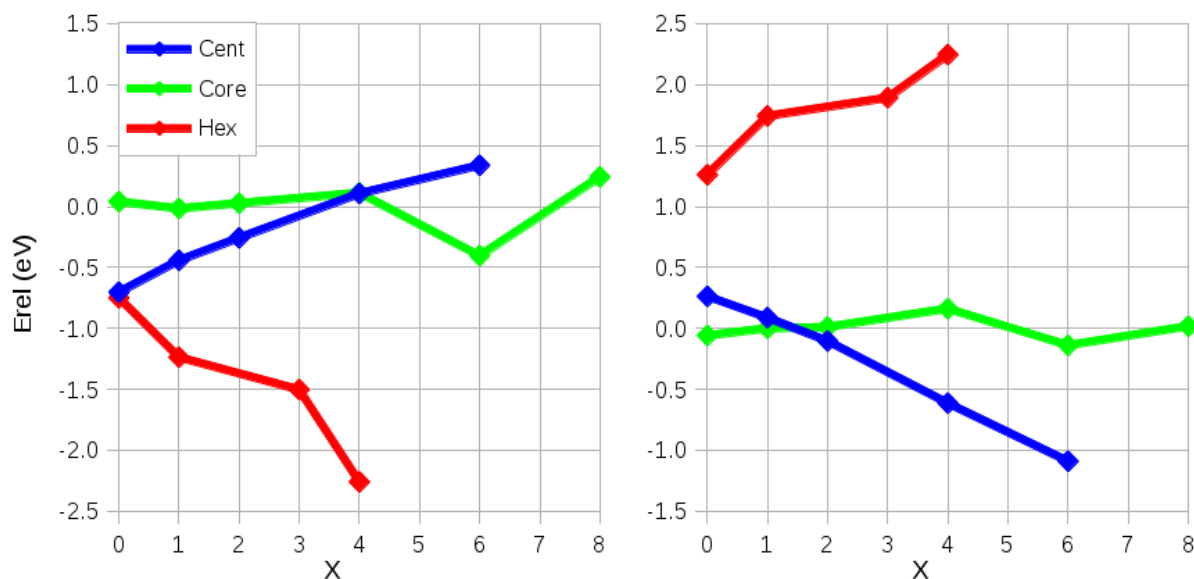


Figure 4-12 Relative energies of multiple CO molecules on (left) Pd₆Pt₃₂ and (right) Pt₆Pd₃₂ clusters. X denotes the number of CO molecules on the cluster.

As with the single adsorption studies, PdPt exhibits similar trends to the AuPd system, as shown in figure 4-12. The energy differences are much lower than for AuPd, due to the smaller difference in binding energy and surface energy. However, energy level exchange still occurs for both Pd₆Pt₃₂ and Pt₆Pd₃₂, although for Pd₆Pt₃₂ the inversion only occurs after six ligands are bound to the surface of the cluster. both the Pd₆Pt₃₂ and Pt₆Pd₃₂ hex structures are not as strongly correlated as the hex structures for AuPd. This is probably due to the differences in binding strength between the hex-1 binding site and the hex-2 binding site (see figure 4-2), which is larger for Pd₆Pt₃₂ than for Au₆Pd₃₂.

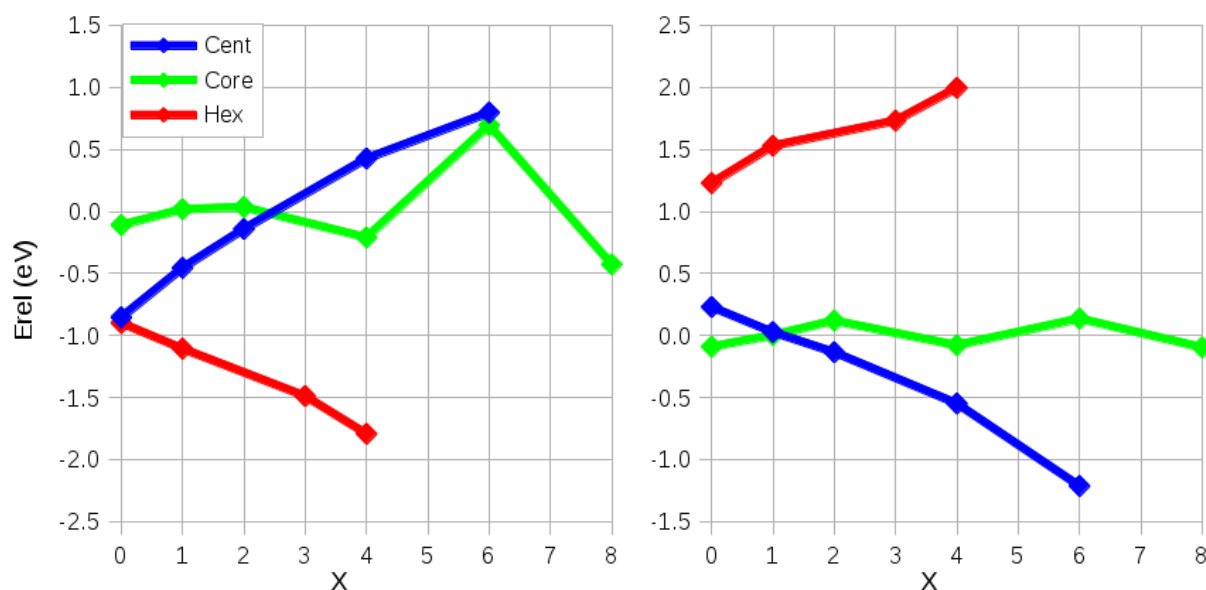


Figure 4-13 Relative energies of multiple H atoms bound to (left) Pd₆Pt₃₂ and (right) Pt₆Pd₃₂ clusters. X denotes the number of H atoms on the cluster.

Hydrogen ligands also cause the core and centroid geometries to undergo structural rearrangement, with a slightly larger energy gap between the core and centroid structures for Pt₆Pd₃₂H₆ (1.35 eV) than for Pt₆Pd₃₂(CO)₆ (0.95 eV). The core-shell Pd₆Pt₃₂(H)₆ exhibits unusual instability compared with its neighbours, and this could be due to convergence criteria or electronic effects.

4.3.6 CuPt

For Cu₆Pt₃₂(CO)_x, complete structural inversion is found, as demonstrated in figure 4-14. When the number of ligands on the surface is zero, the energy ordering is centroid < core < hex, which changed to hex < core < centroid. This is in agreement with the experimental results by Andersson et al. (30, 31). However, Anderssons work was on extended surfaces so the Cu atoms had a co-ordination of nine, whereas in this work the Cu atoms are on the disfavoured vertex sites and have a coordination number of six. In addition, the vertex sites have the lowest number of

mixed Pt-Cu bonds, so the hex arrangement should still be disfavoured. This could be due to the transfer of electron density from the CO molecule to the Pt, with the resulting charge transfer stabilising the Cu on the vertex sites.

The $\text{Pt}_6\text{Cu}_{32}$ system shows no energy reordering, although the stability of the centroid structure increases relative to the other species.

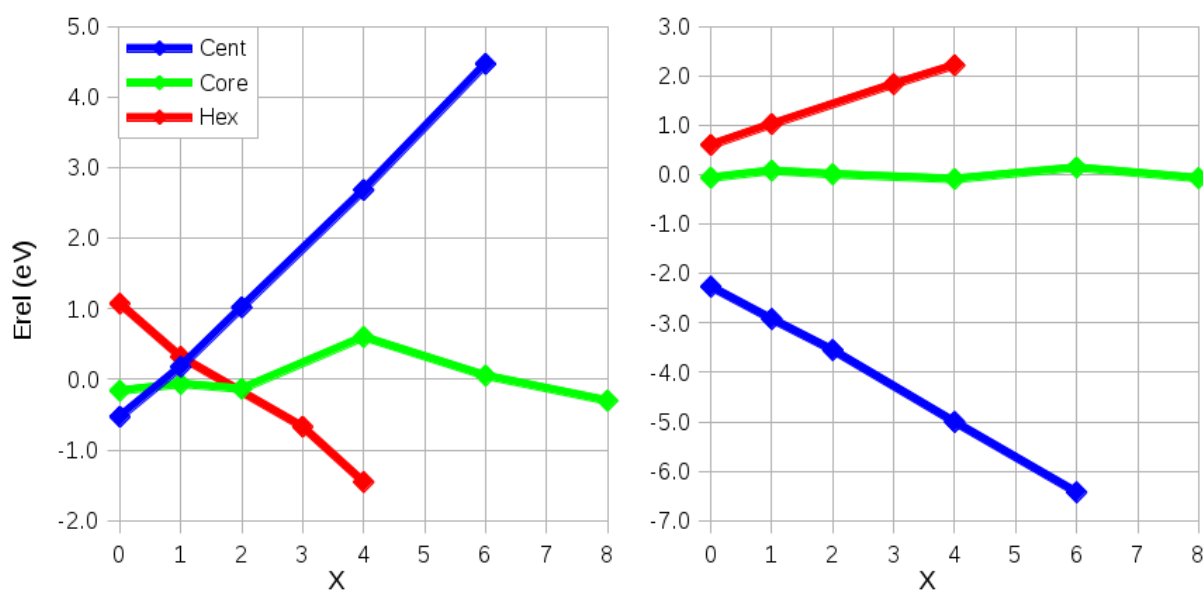


Figure 4-14 Relative energies of multiple CO molecules on (left) Cu₆Pt₃₂ and (right) Pt₆Cu₃₂ clusters. X denotes the number of CO molecules on the cluster.

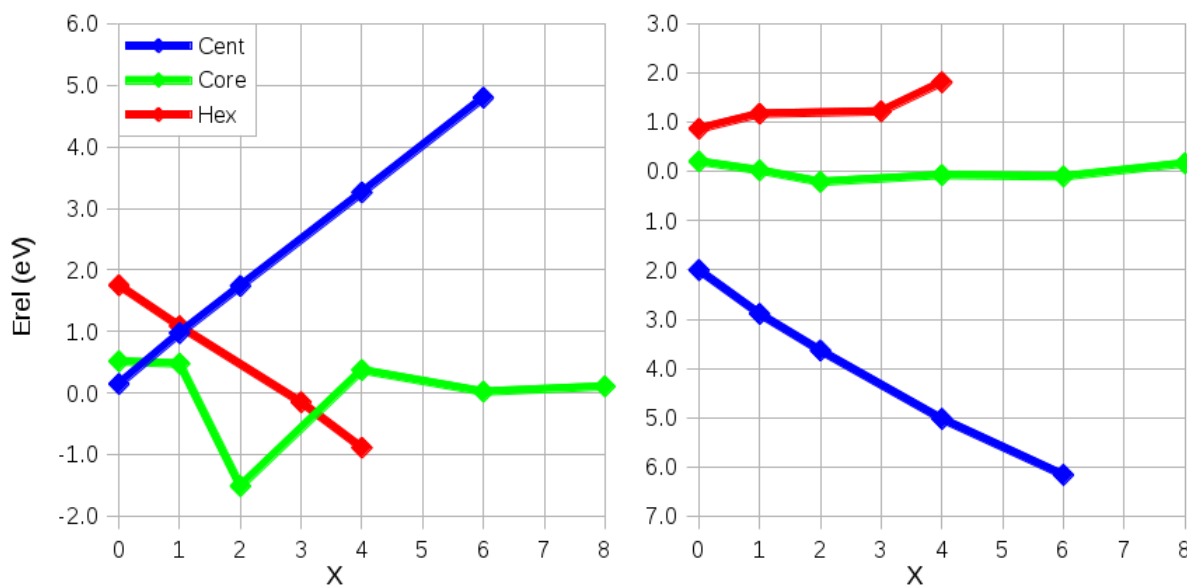


Figure 4-15 Relative energies of multiple H ligands on (left) Cu₆Pt₃₂ and (right) Pt₆Cu₃₂ clusters. X denotes the number of atoms on the cluster.

Figure 4-15 shows hydrogen on Cu₆Pt₃₂ shows a similar trend to CO, although the effect is lessened by the unusual stability of Cu₆Pt₃₂H₂, and the smaller energy differences between the hex and core-shell structures of 2.05 eV and 1.26 eV for CO and H respectively. Interestingly the energy gap between the Pt₆Cu₃₂ structures with CO or H bound to the surface is quantitatively similar, with energies between the hex and centroid structures where X=4 of 6.8 eV for H ligands and 7.21 eV for CO.

4.3.7 RhPd

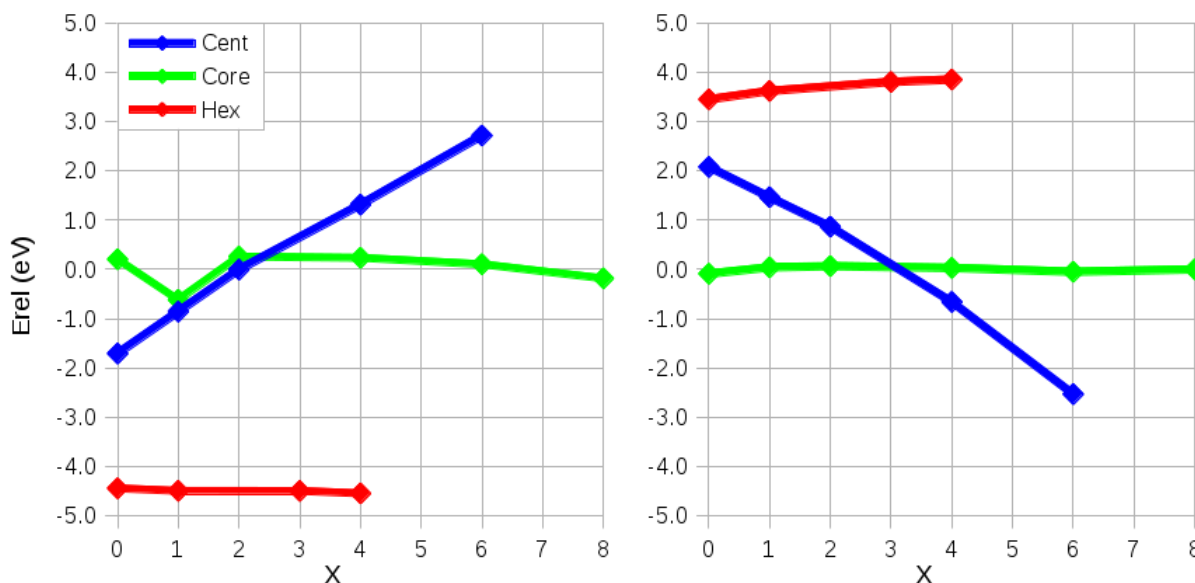


Figure 4-16 Relative energies of multiple CO ligands on (left) Rh₆Pd₃₂ and (right) Pd₆Rh₃₂ clusters. X denotes the number of ligands on the cluster.

Figure 4-16 shows RhPd shows similar character to both AuPd and PdPt clusters, with energetic inversion occurring between the core-shell and the centroid structures for both Rh₆Pd₃₂ and Pd₆Rh₃₂. In addition, the energy gap between the core and the centroid structure is larger for Rh₃₂Pd₆(CO)₆ (2.6eV) compared with Pt₆Pd₃₂(CO)₆ (0.96eV) and smaller than Pd₆Au₃₂(CO)₆. This is in agreement with the work by Tao et al. (104, 105), who found adding a mixture of CO and NO gas increased the amount of Pd in the surface layers of RhPd nanoparticles.

4.3.8 Summary- Multiple Adsorption

In general a linear trend is observed such that further adsorption on energetically unfavourable sites increases the energy of that site relative to others. This trend is most clearly observed with Pd₆Rh₃₂CO_x (figure 4-16), Pt₆Cu₃₂CO_x (Figure 4-14), Pt₆Cu₃₂H_x (Figure 4-15), and Pd₆Au₃₂CO_x (figure 4-10). There seems

to be certain structures which act as the exception to this trend. For example, $\text{Cu}_6\text{Pt}_{32}\text{H}_2$ is a particularly striking example of this and could be caused by charge and electronic effects. In addition, the method of shifting the energies relative to the core-shell structure may have amplified differences that are small when using the absolute relative energies, as shown on the left hand side of figure 4-4.

It is probable that many systems would undergo structural inversion. Either CO or H may be strong enough to bring Pd to the surface of a $\text{Pd}_{\text{core}}\text{Au}_{\text{shell}}$ nanoparticle, due to the stronger interaction energy of CO and H to Pd. This would also be the case for $\text{Pt}_{\text{core}}\text{Pd}_{\text{shell}}$ and $\text{Pd}_{\text{core}}\text{Rh}_{\text{shell}}$ nanoparticles. Due to rhodium's strong binding energy to oxygen (see Table 4-2) this explains the structural inversion found by Tao et al (105).

CuPt is slightly different to the aforementioned examples, for two reasons. Firstly, CuPt has a strong preference for bimetallic Cu-Pt bonds instead of adopting a core-shell arrangement to minimise surface energy. Inversion is seen when CO or H is bound to the surface of PtCu, but the Cu is bound to the surface because it stabilises the Pt bound to the ligand molecule. This could be due to the Cu localising the charge on the Pt atom, resulting in strong back donation of charge from the metal to the ligand. Analysing the local density of states on the Pt atom would reveal if this is the case.

4.4 Conclusions

The stabilities of different nanoparticles were investigated, with energetic reordering common where the interaction energies between different metals in the cluster is large enough. The inversion of structure appears dependent on the surface energy of

the element and the strength of the interaction energy with the ligand. This enables RhPd nanoparticles to undergo a reversible reaction, as both Rh and Pd can bind strongly to different ligands. In addition, local effects can play a role in effecting the clusters structure. Of the systems studied here, only CuPt exhibited this phenomenon, with Cu finding it energetically favourable to move to a vertex site usually disfavoured due to its high surface energy (compared with Pt) and the reduced number of preferred Pt-Cu bonds.

This work could be expanded to study more systems. TiPt would be an interesting system to study, as it has been suggested for use in fuel cells. In this case, a Ti-core Pt-shell nanoparticle would be preferred to decrease cost but keep the chemical activity, but avoid Ti coming to the surface of the cluster and poisoning the catalyst(135).

In addition, further analysis of the CuPt system will be beneficial to understanding why Cu prefers to occupy surface sites. This could be achieved by investigating charges or the density of states.

In addition, truncated octahedra were used exclusively in this work, although clusters can adopt many different geometries. For pure metals, it has been shown that adsorbates can affect the structure of a cluster(88), and extending this to bimetallic clusters may be useful. Finally, larger clusters can give a better approximation to experiments on catalysts. As an example, the work by Tao et al. was performed using clusters 15 nm \pm 2 nm across(105). Although this is clearly beyond what can be modelled using DFT, increasing the size slightly would represent a closer link to experimental systems.

Chapter 5- Structure and CO Adsorption of Small AuPd Clusters

5.1 Introduction

Small clusters made of a few atoms can be studied relatively easily using both experimental and theoretical methods. This enables us to test theoretical methods or predictions or to provide greater insight into experimental data. In addition, high levels of theory (such as coupled-cluster methods) can be used to study small systems (136-138), confirming the reliability of XC functionals (137). This means a dual approach of searching at a lower level of theory followed by a subsequent high level theory (as described in previous work (3, 87, 117, 118) and in Chapter 3-) is no longer necessary and can in fact be detrimental to searching the energy landscape. For example, using the Gupta potential for Au_4 with the BCGA only finds the tetrahedral geometry, whereas Au_4 has been found to be a planar rhombus structure at the DFT level (114, 139).

Experiments on gas phase clusters made of only a few atoms are much trickier, particularly as an ultra high vacuum is often required. In addition, uncharged clusters are often difficult to study. A common method is to use a stabilisation media, such as inert argon gas, to trap the clusters which can then be studied using infra red (IR) or Photo-Electron Spectroscopy (PES).

Typically, argon is used as a carrier gas with any other gaseous molecules added to it in low concentrations. A laser is used to ablate atoms from a surface. These condense onto a CsI salt window, from which they can be studied as shown in figure 5-1. This has been used to study various systems, including water (140), boric oxides (19) and metal clusters (141, 142).

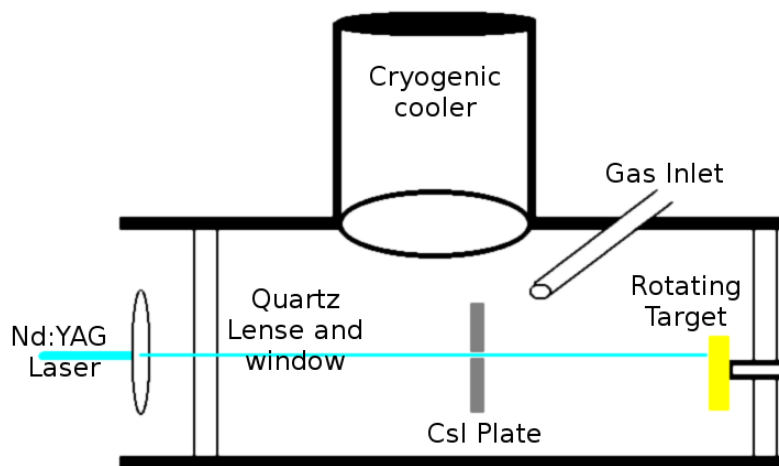


Figure 5-1 Experimental setup for studying small gas phase clusters. Based on the design in (19). A Nd:YAG laser beam atomises metal atoms from a target, which are then trapped inside a noble gas liquid deposited onto a CsI plate.

Charged clusters are also studied experimentally, and have the advantage that beams of particles can be created and directed so they can be studied using techniques like time-of-flight mass spectrometry or deposited onto a surface (143, 144).

5.1.1 Previous work on small gold, palladium and AuPd clusters

Gold has been extensively studied due to its unusual properties at the nanoscale (145-147). At the smallest sizes, gold clusters are planar, and the planar structures are the most favourable structures up to 7 atoms for cationic clusters (148) and 12-15 for neutral and anionic clusters (145, 149). The potential energy surface

using high level calculations has been found to be quite flat, which makes the global minima a challenge (136). Full relativistic calculations by Guo et al. find the triangular structure is more stable for Au_3 , with the spin-orbit coupling quenching the Jahn-Teller distortion effects (150). In the same paper, Guo et al. confirmed this structure using laser-ablation and matrix-infrared spectroscopy.

PdCO has been studied at the coupled cluster level by Filatov et al., with relativistic effects strengthening the Pd-C bond (138). The Pd_2 dimer has been found to have a bond length of 2.53\AA (131) and an energy of $1.04\text{eV} \pm 0.16\text{eV}$ (151) and a triplet ground state (152). Schultz et al. (137) have looked at the Pd_2CO system with many different XC functionals, and find the PW91 functional gives a small error of 2% for the dissociation energy of Pd_2 . The ground state of Pd_4 has been found to adopt a tetrahedral geometry in the triplet state (153), and adding CO changes the electronic state from triplet to singlet, with the CO molecule occupying the 3-fold hollow site (131).

Bimetallic systems have attracted less attention, and have tended to be studied at a lower level of theory. Jian-Jun et al. (154) studied Au_nPd_2 (where $n=1-4$) finding a triangular structure for Au_1Pd_2 and the tetrahedral geometry for Au_2Pd_2 . However, they used a small (DZ) basis set and the B3LYP functional, which gives a larger error than the PW91 function for the dissociation energy of Pd_2 (137). Wu et al. (111) studied Au_nPd clusters, also using the B3LYP functional and a DZ basis set, finding the linear Pd-Au-Au structure as the most stable, followed by the other linear homotop (Au-Pd-Au) as 0.91eV higher in energy. They also find Au_3Pd_1 adopts a tetrahedral geometry.

In this work, we investigate AuPd clusters with different geometries and spin states, and how these clusters are affected upon adsorption of CO. There are many studies on these clusters, although some of this work uses a small (DZ) basis set and the B3LYP XC functional (154). This functional is fitted to experimental results to the first 18 elements (68, 69), and sometimes gives inaccurate results for the later transition metals, failing to account for the delocalised character of the electron cloud within metals (155).

5.2 Methodology

5.2.1 Structures

5.2.1.1 Bare clusters

All sizes and compositions were investigated from dimers up to tetramers (4 atoms), including different spin states. For the dimers, an initial bond length of 2.5 Å was chosen.

For trimers, 3 different structures were chosen: linear, triangular and bent. The initial angles for the bent and triangular geometries were 170° and 60°, respectively. The bent geometry was based on work on Au₃ by de Bas et al. (114). All the different homotops for each geometry were selected. For example, the linear geometry for Au₂Pd₁ can be either Au-Au-Pd or Au-Pd-Au, and both initial geometries were selected.

For tetramers, the different initial structures were linear, rhombus, square, tetrahedral and a triangular structure which contains a single ad-atom. The initial rhombus geometry was set as two equilateral triangles, with bond angles of 60°. The

initial bond length was set to 2.5 Å in all cases. This results in 42 separate non-symmetry equivalent structures across all homotops and compositions. The starting structures are shown in figure 5-2.

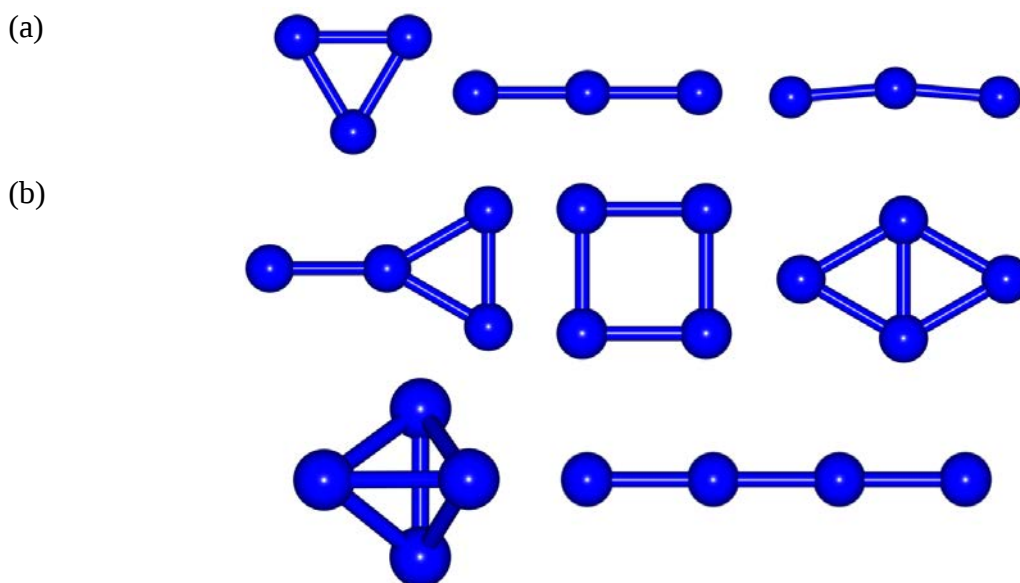


Figure 5-2 Initial geometries of the bare (a) three atom clusters and (b) four atom clusters.

5.2.1.2 CO bound clusters

As stated in Chapter 4- , nanoparticles have many different binding sites, so more calculations are required. All metal-metal bond lengths were set to 2.5 Å, metal-carbon bond lengths to 2.0 Å and carbon-oxygen to 1.5 Å. CO was added to the unminimised structure.

For dimers, 4 different geometries were considered: linear, bridge, bent around the C-M-M bond and the O-C-M bond, with a bond angle of 135°. These structures are shown in figure 5-3. For the bimetallic Au₁Pd₁ both the Au and Pd sites underwent geometry minimisation.

Triangular trimers enable the 3 fold hollow sites to be investigated. CO was bound to all other bridge and atop sites, excluding symmetry equivalent positions.

For tetramers, all atop, bridge, 3 and 4 fold hollow sites were investigated when the structure allowed it. The structures of the trimers and tetramers are shown in figure 5-3b and figure 5-3c, respectively.

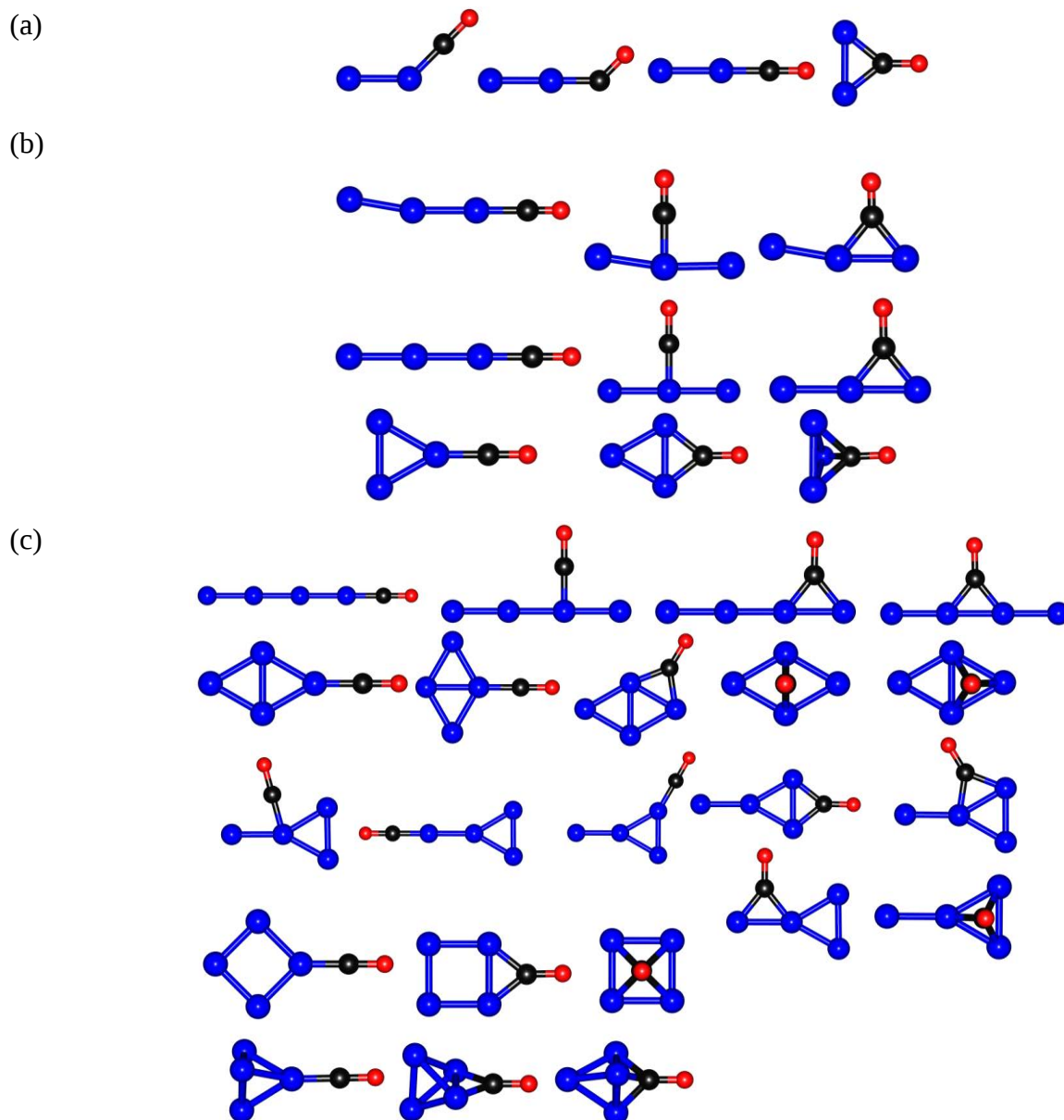


Figure 5-3 Initial geometries of (a) dimers (b) trimers and (c) tetramers of PdAu clusters, all with CO. Colour refer to metal (Au or Pd) blue, carbon black and oxygen red.

5.2.2 DFT Calculations

DFT was used for structure optimisation, using a triple zeta basis set with polarisation function (TZVP) (156). Scalar relativistic ECP's were used for Au and Pd, along with charge fitting basis sets (157). A large basis set including 19 electrons ((7s6p5d)/[6s3p3d]) for gold and 18 (7s6p5d)/[5s3p3d] electrons for palladium were used in the calculations. All electrons were calculated explicitly without core potentials for the carbon ((11s6p1d)/[5s3p1d]) or oxygen ((11s6p1d)/[5s3p1d]) atoms. Calculations performed using the NWChem quantum chemistry package version 5.1 (85). Vibrational frequencies were calculated after geometry optimisation was completed to confirm the structure was a local minima and not on a saddle point on the PES. Smearing was not used, as the small size of the clusters it should not normally be required to assist the convergence.

Different spin states were investigated. For the bare clusters, six different spin states were investigated. For clusters with an even number of electrons, singlet, triplet and quintet states were calculated and for an odd number of electrons the doublet, quartet and sextet spin states. When CO was bound to the cluster, only low spin (singlet or doublet, for even and odd numbers of electrons respectively) and mid spin (triplet or quartet) states were calculated. Symmetry was utilised during the calculations, to enable freedom for the geometry optimisation

5.2.3 Calculations

All energies in this chapter are reported in eV. Binding energies for the bare clusters were calculated using equation 5-1. $E(Au_nPd_m)$, $E(Au)$ and $E(Pd)$ are the energies for the cluster, the gold atom and the palladium atom, respectively.

$$E_b = E(Au_nPd_m) - nE(Au) - mE(Pd) \quad 5-1$$

The energies for the atoms were found to be -135.80129 Hartrees for gold and -127.90861 Hartrees for Palladium. For some structures the relative energies were used. These are calculated relative to the lowest energy structure for that composition and size.

5.3 Results

5.3.1 Bare Clusters

5.3.1.1 Dimers

Electron Multiplicity	Structure	Frequency (cm ⁻¹)	Bond length (Å)	E _b (eV)
Singlet	Au ₂	171.7	2.539	-2.270
Doublet	Au ₁ Pd ₁	187.7	2.503	-1.988
Singlet	Pd ₂	168.9	2.664	-1.067
Triplet	Au ₂	100.2	2.794	-0.464
Quartet	Au ₁ Pd ₁	153.6	2.603	0.137
Triplet	Pd ₂	208.9	2.488	-1.555
Septet	Au ₂	134.8	2.621	4.799
Sextet	Au ₁ Pd ₁	118.9	2.619	5.222
Septet	Pd ₂	188.0	2.491	0.459

Table 5-1 The vibration frequencies (cm⁻¹), bond lengths (Å) and binding energies (in eV) of Au₂, Pd₂ and Au₁Pd₁ at different spin states.

Table 5-1 shows the binding energies, bond lengths and stretching frequency of Au₂, Au₁Pd₁ and Pd₂, with different spin states. None of the clusters had imaginary frequencies, so all the structures and spin states studied are local minima.

For the quartet, sextet and septet electron multiplicities, the binding energies are positive, such that the separate atoms have a lower energy than the high spin

dimers. In agreement with previous results, the AuPd and Au₂ dimer are more stable in the lowest available spin state, whereas the triplet state in Pd₂ has a lower energy than the singlet state.

Our results for the bond length for Au₂ of 2.54 Å agree reasonably well with results from previous DFT calculations (2.48-2.49 Å) (26), and are slight overestimations compared with experimental results (2.47 Å) (158) and high level CCSD(T) calculations with a complete basis set (2.44 Å) (159).

The Pd₂ dimer has a bond length of 2.49 Å, which compares very favourably with experimental data (2.47 Å) (159) and high level CCSD(T) calculations (2.44 Å) (158).

5.3.1.2 Trimers

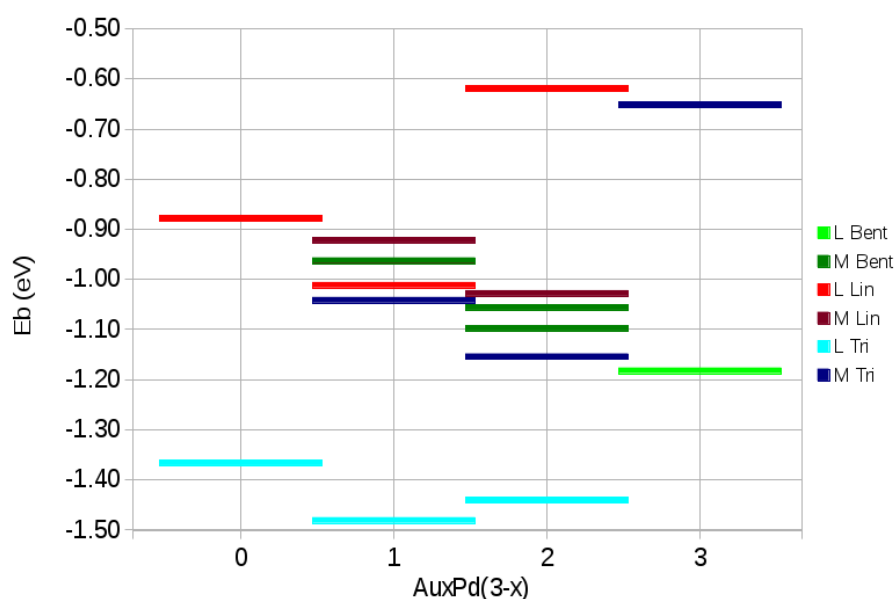


Figure 5-4 Binding energies of the 3 atom AuPd clusters. In the key, 'L' refers to the low-spin (doublet for Au₃ and Au₁Pd₂, singlet for Pd₃ and Au₂Pd₁) clusters whereas 'M' refers to mid-spin clusters (triplet state for Au₂Pd₁ and Pd₃, quartet state for Au₃ and Au₁Pd₂). Structural labels are lin- linear and tri- triangle.

The energies of the different low and mid spin structures are shown in figure 5-4. The lowest energy structure of Au_3 is the low (doublet) bent structure, with an angle of 140° , arising from Jahn-Teller distortion of the equilateral triangle. This was the only stable low spin state structure, with the linear and triangular geometries converging upon the same structure. The same occurred with the quartet (mid) spin case, where the only stable structure was the triangular structure. The bond length for the Au_3 (bent) structure was 2.58 Å, and for the triangular structure 2.66 Å, due to the weaker bonding of having electrons in the high energy states.

The bimetallic clusters exhibit more similar behaviour to the Pd_3 system, as their global minima are triangular structures. Both Au_1Pd_2 and Au_2Pd_1 have more stable higher energy structures, due to the presence of different homotops and increased complexity in the electronic landscape. The results for Au_1Pd_2 agree with Jian-Jun et al (154), with a Pd-Pd bond length of 2.53 Å compared with 2.57 Å and Au-Pd length of 2.61 Å compared with 2.67 Å. Energies also compare reasonably favourably (1.37eV compared with 1.1eV for Jian-Jun). The difference is due to the different exchange correlation functional used, and because Jian-Jun used a smaller basis set.

5.3.1.3 Tetramers

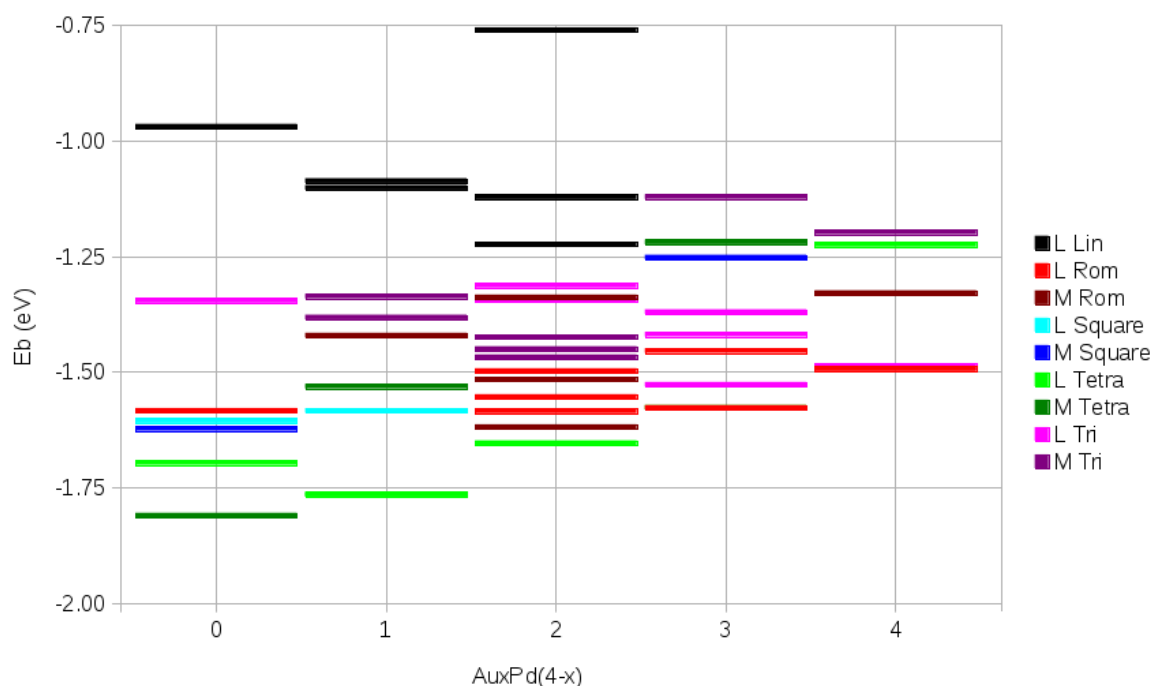


Figure 5-5 Binding energies of the 4 atom AuPd clusters. In the key, 'L' refers to the low-spin clusters whereas 'M' refers to mid-spin clusters. Structural labels are: lin-linear, rom- rhombus, tetra- tetrahedral and tri- triangle with an ad-atom.

Figure 5-5 shows the energies of the four atom clusters, indicating the energy landscape is more complicated due to the high number of different structures, in addition to different homotops for bimetallic clusters. Linear structures are high in energy, and have imaginary frequencies for Au₄ and Pd₁Au₃, indicating they are not locally stable. In addition, all high spin state linear structure were not stable, either having imaginary frequencies or converging on a different geometry. Many more structure were found for Au₂Pd₂ than reported elsewhere (154).

The tetrahedron is the most stable cluster geometry for Pd₄, Au₁Pd₃ and Au₂Pd₂ with the triplet state preferred for Pd₄, the doublet state is preferred for Au₁Pd₃ and the singlet for Au₂Pd₂. The Pd₄ geometric and electronic structure is in agreement with previous calculations (153). The second most stable geometric

structure for Pd_4 was a square geometry, in disagreement with results by Dai, who find the rhombus is lower in energy than the square geometry (153). Small Au clusters are known to be planar in the bulk, and we find the singlet rhombus slightly lower (0.01 eV) in energy than the singlet triangle. This is in agreement with other theoretical calculations (139).

5.3.2 CO bound clusters

5.3.2.1 Dimers

The low spin Au_2CO structures only converged onto two different structures: a linear geometry and a bridge geometry with the linear geometry over 1.1 eV lower in energy. For the bridge geometry the Au-C-O bond angle is 124° and Au-Au bond length is 3.29 Å. Indicating the carbon is sp^2 hybridised with negligible Au-Au bonding.

Pd_2CO exhibits the opposite character, with the bridge geometry preferred over the linear geometry by 1.5 eV. This is in agreement with previous calculations (131). The low spin state was lower in energy as the CO quenches the electron orbitals.

AuPd bimetallic clusters exhibit a larger number of stable structures. The two lowest structures were both bound atop to Pd, in either a linear or bent geometry with an energy separation of 0.06 eV. Again the CO quenched the electronic states so the doublet state is the preferred electronic configuration. It is unsurprising that the Pd site is preferred, as bulk Pd has a stronger adsorption energy than Au, where CO barely binds to the Au (111) surface (160).

The results for Au_2CO and Pd_2CO agree with results by Peng et al. (161), although they find the linear structure is preferred for the bimetallic cluster.

5.3.2.2 Trimers

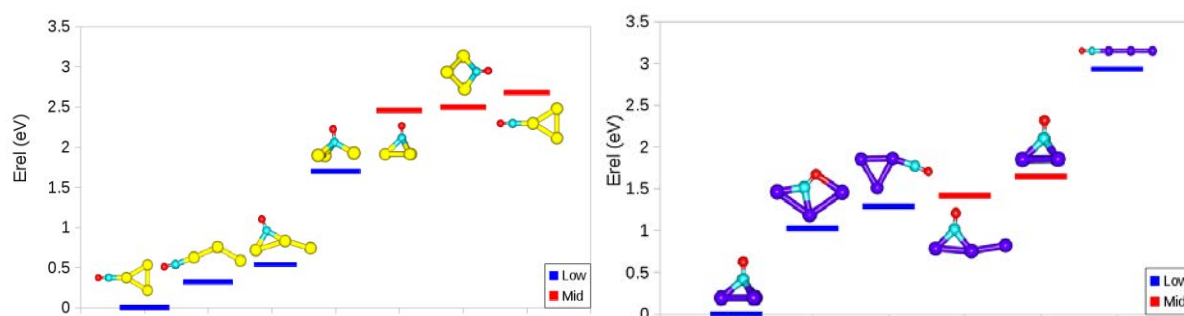


Figure 5-6 The relative energies of the pure clusters, and the structure of each. Left- Au_3CO . Right- Pd_3CO .

For the pure clusters CO binds in different locations for Pd_3 and Au_3 , continuing the trend that was found in the dimers. The most stable structure found for Pd_3CO is with the CO bound to the 3 fold hollow site of the Pd_3 triangle (as shown in figure 5-6), whereas for Au_3 the lowest energy geometry changes from the bent structure to a triangle, with the CO bound atop to a gold atom. In both cases, the spins are quenched such that the low spin state is preferred. Other local minima were found, and these are shown in figure 5-6. For gold, lots of different local minima were found, including both bridge and hollow binding sites. However, for CO bound to the 3-fold hollow site, the gold atoms were moved apart to a distance of 2.7 Å or 3.2 Å, probably to strengthen the C-Au bonds instead of the Au-Au bonding.

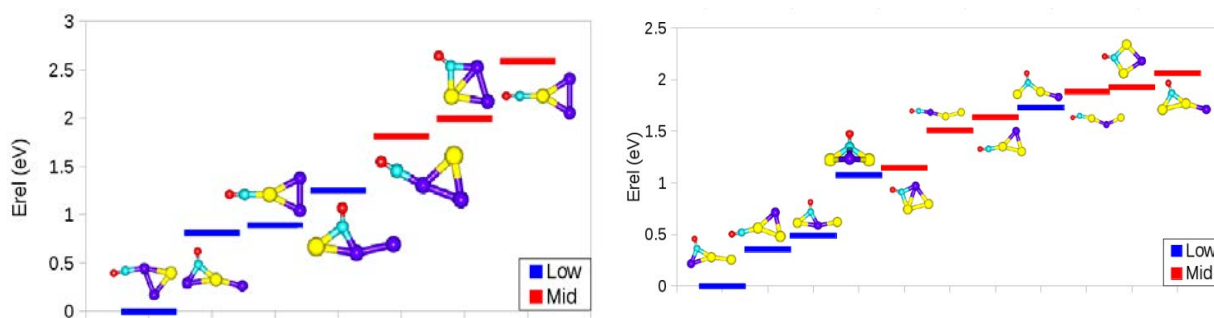


Figure 5-7 relative energies of the 3 atom bimetallic clusters and their structures. Left- Pd_2Au_1 . Right Au_2Pd_1

The different bimetallic structures are shown in figure 5-7. For both $\text{Au}_1\text{Pd}_2\text{CO}$ and $\text{Au}_2\text{Pd}_1\text{CO}$ the lowest energy structures are low spin structures, with the Au_1Pd_2 and Au_2Pd_1 adopting a triangular and bent geometry respectively. Notably absent is the CO occupying a Pd-Pd bridge site. The triangular geometry with the CO on this bridge site was found, but had imaginary frequencies indicating it occupied a saddle point on the energy landscape. Au_2Pd_1 clusters have a more complex energy landscape with more local minima found relative to Pd_3 or Pd_2Au_1 . This can be explained by Au_3 having a more complicated landscape compared with Pd_3 and additional structures as different homotops of the same geometry exist for bimetallic structures.

5.3.2.3 Tetramers

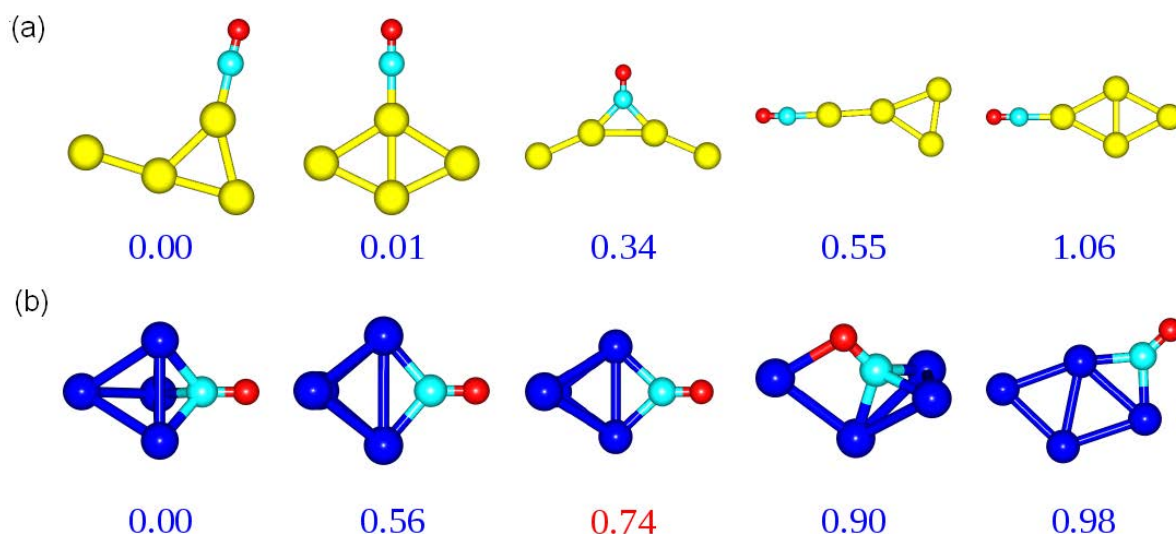


Figure 5-8 Low energy structures for (A) Au_4CO and (B) Pd_4CO with their relative energies (in eV). Energies shown in blue indicate a singlet state structure, whereas an energy in red indicates the structure has a doublet spin state. Atom colours are: yellow- gold, blue- palladium, cyan- carbon and red- oxygen.

Many different structures were found for each composition, so only the five lowest energy structures were investigated in detail. For Au_4 , Au_3Pd_1 , Au_2Pd_2 and Au_1Pd_3 the lowest five structures were in the singlet or doublet state. Pd_4 has one structure that occupies the mid-spin state. The lowest energy structures for Au_4 and Pd_4 are shown in figure 5-8, along with their relative energies. For Au_4 the two lowest lying isomers are only separated by 0.01 eV, making it difficult to confirm the triangular structure is the global minima. Most of the low energy structures are planar, which contrasts with Pd_4CO which prefers to adopt the three dimensional structure. Both of these compare favourably with previous work (131). The three lowest energy Pd_4CO structures are all tetrahedral, whereas Au_4CO has a wider range of structures over a narrower energy range. Interestingly, the linear structure has been heavily stabilised by adding CO. for the bare cluster, the linear Au_4 cluster was not even locally stable as it had multiple imaginary frequencies.

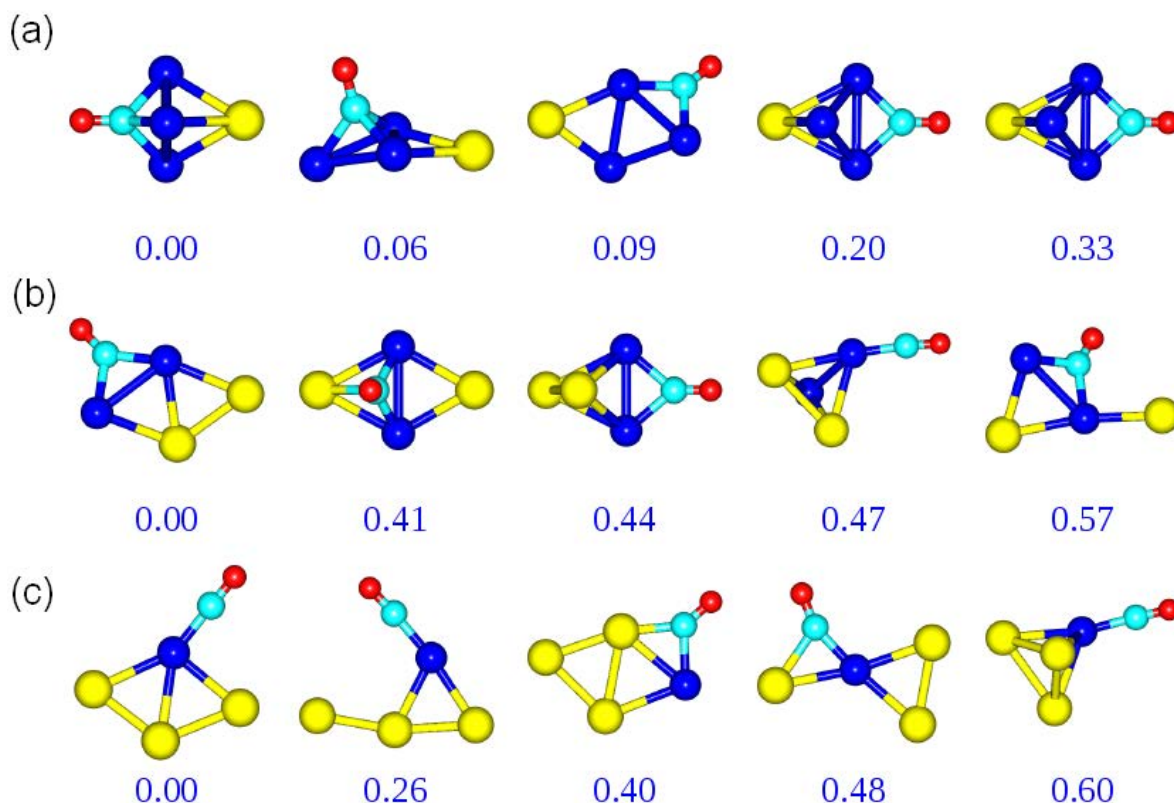


Figure 5-9 Low energy structures for (A) $\text{Au}_1\text{Pd}_3\text{CO}$, (B) $\text{Au}_2\text{Pd}_2\text{CO}$ and (C) $\text{Au}_3\text{Pd}_1\text{CO}$ with their relative energies (in eV). The same colour scheme is used to that in figure 5-8.

The bimetallic structures are shown in figure 5-9. All show a complex energy landscape with multiple minima within 0.5eV of the lowest energy structure. The global minima for $\text{Au}_1\text{Pd}_3\text{CO}$ is the analogue to the Pd_4CO global minima, and $\text{Au}_3\text{Pd}_1\text{CO}$ shows similar character to Au_4CO , although the two lowest energy structures are swapped over, and spread over an energy range of 0.26eV.

5.4 Conclusions and Future Work

We have found many of the low energy structures for small AuPd clusters up to 4 atoms in size, both with and without CO adsorbed to the surface. The IR frequencies and intensities have been calculated, such that it may be possible to compare these

results with gas phase experiments, with the CO molecule being used as a probe molecule to find the shape of the cluster.

There are numerous way in which this work could be expanded. At the time this work was started, computational resources were more limited and advances in computing have opened up the chance to expand this work to higher levels of theory, such as Coupled Cluster (CC) methods. This has the advantage that the energy found is truly variational, whereas DFT is reliant on the imperfect although useful exchange correlation functional. Also, these calculations were calculated using scalar relativistic calculations. It has been shown that spin-orbit coupling can affect the structure of small gold clusters(150).

In addition, different search methods can be used. Negreiros et al. (112) has created a Eigen Vector following approach to study oxygen binding to Ag_3 . These calculations work by calculating the hessian (the second derivative of the energy) to search for saddle points, local and global minima. An additional method that has been used is the genetic algorithm, which has recently been used to study small silver-gold clusters(113) and tin-bismuth bimetallic clusters(162, 163). This uses the same methods as shown in Chapter 3- .

5.5 Appendix- Relative Energies and Vibration Frequencies

5.5.1 Dimers

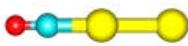
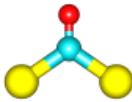
Structure	Spin	Relative Energy (eV)	CO Stretching Frequency (cm^{-1})	Other Frequencies (cm^{-1})
	Low	0.00	1840	49, 176, 341, 341, 424
	Low	1.12	2101	76, 275, 360, 422, 683

Table 5-2 Relative energies (in eV) and vibration frequencies (in cm^{-1}) for different stable structures of Au_2CO . Gold atoms are shown in yellow, carbon in cyan and oxygen in red.



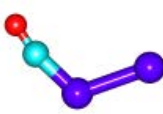

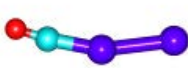
Structure	Spin	Relative Energy (eV)	CO Stretching Frequency (cm^{-1})	Other Frequencies (cm^{-1})
	Low	0.00	1864	171, 215, 363, 448, 587
	Low	1.56	2036	99, 100, 157, 428, 429, 514
	Mid	1.72	2026	40, 188, 253, 304, 453
	Mid	1.77	2030	27, 43, 169, 286, 315, 417
	Mid	1.78	2039	9, 180, 280, 312, 417

Table 5-3 Relative energies (in eV) and vibration frequencies (in cm^{-1}) for the different stable structures of Pd_2CO . Palladium atoms are shown in dark blue, carbon in cyan and oxygen in red.

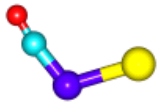

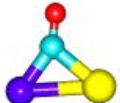

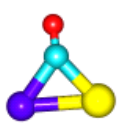
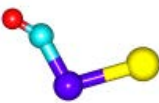
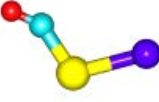
Structure	Spin	Relative Energy (eV)	CO Stretching Frequency (cm^{-1})	Other Frequencies (cm^{-1})
	Low	0.00	2102	36, 163, 269, 313, 471
	Low	0.07	2041	41, 42, 165, 333, 334, 429
	Low	0.18	1911	110, 200, 330, 332, 528
	Low	0.47	2067	35, 41, 196, 305, 306, 397
	Mid	2.62	1850	124, 153, 225, 345, 381
	Mid	2.89	1927	18, 71, 129, 272, 415
	Mid	2.95	1954	40, 68, 138, 273, 430

Table 5-4 Relative energies (in eV) and vibration frequencies (in cm^{-1}) for the different stable structures of $\text{Au}_1\text{Pd}_1\text{CO}$. Gold atoms are shown in yellow, palladium in dark blue, carbon in cyan and oxygen in red.

5.5.2 Trimers

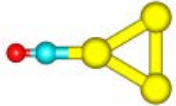

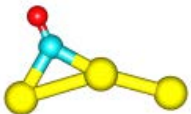
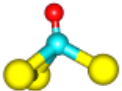
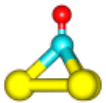
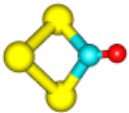
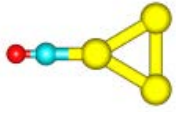
Structure	Spin	Relative Energy (eV)	CO Stretching Frequency (cm^{-1})	Other Frequencies (cm^{-1})
	Low	0.00	2079	41, 53, 93, 104, 159, 331, 339, 431
	Low	0.32	2092	19, 33, 41, 126, 171, 301, 311, 411
	Low	0.54	1907	32, 45, 69, 168, 220, 346, 366, 518
	Low	1.70	1734	19, 64, 118, 140, 250, 324, 345, 584
	Mid	2.46	1837	58, 60, 104, 112, 116, 268, 346, 350
	Mid	2.50	1869	55, 83, 115, 156, 254, 309, 414
	Mid	2.68	1919	21, 44, 81, 96, 110, 143, 248, 416

Table 5-5 Relative energies (in eV) and vibration frequencies (in cm^{-1}) for the different stable structures of Au_3CO . Gold atoms are shown in yellow, carbon in cyan and oxygen in red.

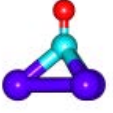
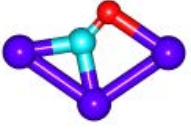
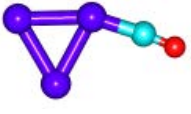
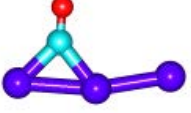

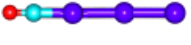
Structure	Spin	Relative Energy (eV)	CO Stretching Frequency (cm ⁻¹)	Other Frequencies (cm ⁻¹)
	Low	0.00	1736	118, 120, 183, 207, 210, 416, 494, 498
	Low	1.03	1641	50, 115, 138, 146, 306, 353, 466, 671
	Low	1.29	2044	107, 173, 176, 226, 460, 462, 483
	Mid	1.42	1781	140, 159, 203, 212, 242, , 416, 492, 542
	Mid	1.65	1874	8, 33, 126, 217, 220, 358, 435, 539
	Low	2.93	2045	82, 99, 107, 128, 233, 427, 446, 447

Table 5-6 Relative energies (in eV) and vibration frequencies (in cm⁻¹) for the different stable structures of Pd₃CO. Palladium atoms are shown in dark blue, carbon in cyan and oxygen in red.

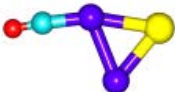
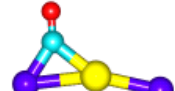
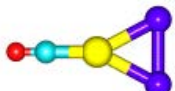
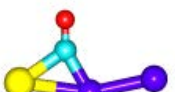
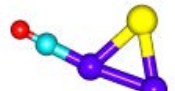
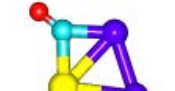
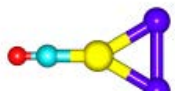
Structure	Spin	Relative Energy (eV)	CO Stretching Frequency (cm ⁻¹)	Other Frequencies (cm ⁻¹)
	Low	0.00	2045	41, 48, 122, 136, 199, 337, 347, 467
	Low	0.81	1905	36, 48, 121, 185, 210, 352, 362, 536
	Low	0.89	2056	31, 34, 97, 148, 230, 258, 293, 391
	Low	1.25	1917	35, 39, 104, 204, 213, 387, 391, 562
	Mid	1.81	2037	44, 46, 115, 131, 179, 317, 347, 422
	Mid	1.99	1878	11, 62, 109, 171, 185, 244, 306, 437
	Mid	2.59	2020	26, 45, 112, 120, 189, 262, 322, 415

Table 5-7 Relative energies (in eV) and vibration frequencies (in cm⁻¹) for the different stable structures of Au₁Pd₂CO. Gold atoms are shown in yellow, palladium in dark blue, carbon in cyan and oxygen in red.

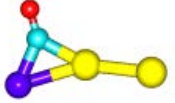
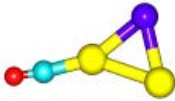
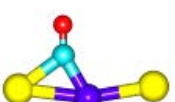
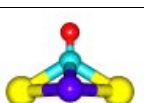
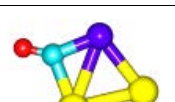
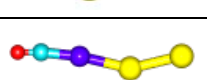
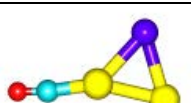
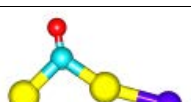
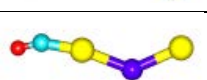
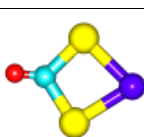
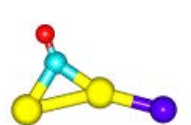
Structure	Spin	Relative Energy (eV)	CO Stretching Frequency (cm ⁻¹)	Other Frequencies (cm ⁻¹)
	Low	0.00	1920	34, 43, 119, 178, 211, 360, 377, 551
	Low	0.35	2065	41, 42, 92, 149, 198, 327, 329, 422
	Low	0.49	1939	37, 38, 98, 201, 215, 390, 395, 569
	Low	1.07	1791	33, 89, 143, 162, 206, 329, 399, 535
	Mid	1.14	1887	10, 75, 101, 151, 194, 302, 320, 490
	Mid	1.51	2054	10, 39, 44, 121, 171, 313, 318, 413
	Mid	1.64	2051	37, 46, 105, 109, 173, 310, 324, 429
	Low	1.73	1857	29, 35, 60, 186, 250, 364, 400, 605
	Mid	1.88	2047	24, 27, 47, 127, 189, 249, 282, 394
	Mid	1.93	1878	15, 61, 128, 163, 185, 193, 288, 493
	Mid	2.06	1908	36, 45, 81, 185, 205, 310, 329, 490

Table 5-8 Relative energies (in eV) and vibration frequencies (in cm⁻¹) for the different stable structures of Au₂Pd₁CO. Gold atoms are shown in yellow, palladium in dark blue, carbon in cyan and oxygen in red.

5.5.3 Tetramers

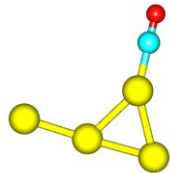
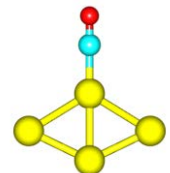
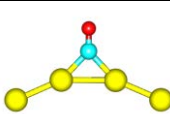
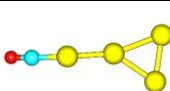
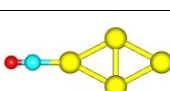
Structure	Spin	Relative Energy (eV)	CO Stretching Frequency (cm^{-1})	Other Frequencies (cm^{-1})
	Low	0.00	2096	17, 35, 37, 48, 88, 105, 143, 193, 337, 341, 433
	Low	0.01	2091	30, 32, 51, 58, 76, 92, 157, 159, 320, 335, 422
	Low	0.34	1949	20, 38, 38, 52, 79, 162, 189, 215, 374, 377, 510
	Low	0.55	2087	10, 15, 16, 31, 64, 83, 156, 180, 292, 299, 384
	Low	1.06	2090	44, 53, 61, 81, 87, 95, 138, 177, 298, 324, 339

Table 5-9 Relative energies (in eV) and vibration frequencies (in cm^{-1}) of the five lowest energy structures for Au_4CO . Gold atoms are shown in yellow, carbon in cyan and oxygen in red.

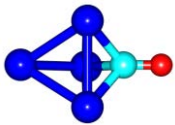
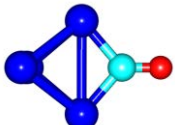
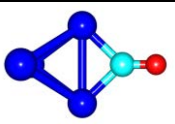

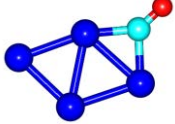
Structure	Spin	Relative Energy (eV)	CO Stretching Frequency (cm^{-1})	Other Frequencies (cm^{-1})
	Low	0.00	1677	76, 78, , 133, 144, 146, 205, 211, 212, 408, 531, 534
	Low	0.56	1801	11, 73, 98, 128, 142, 155, 209, 233, 372, 431, 659
	Mid	0.74	1863	16, 85, 89, 109, 125, 158, 163, 223, 256, 389, 453
	Low	0.90	1479	25, 94, 99, 128, 150, 177, 214, 344, 441, 548, 571
	Low	0.98	1862	65, 105, 119, 147, 171, 199, 215, 246, 431, 482, 615

Table 5-10 Relative energies (in eV) and vibration frequencies (in cm^{-1}) of the five lowest energy structures for Pd_4CO . Palladium atoms are shown in dark blue carbon in cyan and oxygen in red.

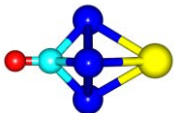
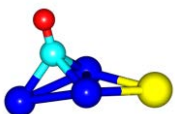
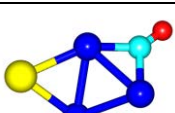
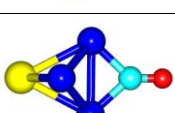
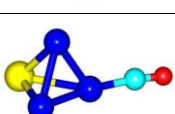
Structure	Spin	Relative Energy (eV)	CO Stretching Frequency (cm ⁻¹)	Other Frequencies (cm ⁻¹)
	Low	0.00	1746	65, 67, 116, 123, 126, 182, 190, 378, 421, 428
	Low	0.06	1749	23, 91, 98, 123, 162, 172, 198, 208, 394, 413, 499
	Low	0.09	1863	25, 40, 89, 100, 130, 171, 190, 208, 383, 417, 528
	Low	0.20	1866	24, 45, 69, 113, 120, 154, 183, 195, 306, 404, 478
	Low	0.33	2022	18, 43, 64, 96, 126, 130, 155, 211, 285, 322, 445

Table 5-11 Relative energies (in eV) and vibration frequencies (in cm⁻¹) of the five lowest energy structures for Au₃Pd₁CO. Gold atoms are shown in yellow, palladium in dark blue, carbon in cyan and oxygen in red.

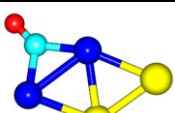
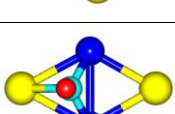
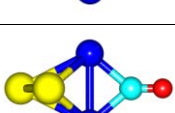
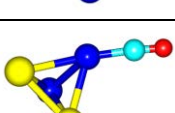
Structure	Spin	Relative Energy (eV)	CO Stretching Frequency (cm ⁻¹)	Other Frequencies (cm ⁻¹)
	Low	0.00	1869	10, 36, 74, 94, 107, 148, 180, 207, 368, 408, 530
	Low	0.41	1794	33, 60, 84, 117, 132, 156, 184, 223, 358, 468, 549
	Low	0.44	1889	15, 28, 63, 87, 88, 146, 163, 189, 253, 375, 396
	Low	0.47	2032	18, 35, 61, 83, 101, 128, 132, 187, 290, 309, 453

Table 5-12 Relative energies (in eV) and vibration frequencies (in cm⁻¹) of the five lowest energy structures for Au₂Pd₂CO. Gold atoms are shown in yellow, palladium in dark blue, carbon in cyan and oxygen in red.

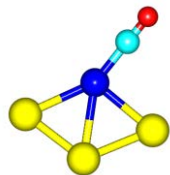
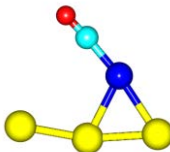
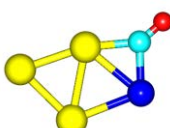
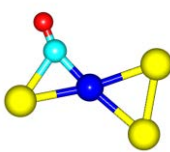
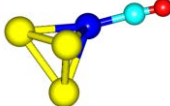
Structure	Spin	Relative Energy (eV)	CO Stretching Frequency (cm^{-1})	Other Frequencies (cm^{-1})
	Low	0.00	2045	25, 44, 48, 64, 93, 119, 153, 159, 328, 336, 455
	Low	0.26	2063	19, 32, 44, 47, 95, 125, 149, 191, 334, 344, 439
	Low	0.40	1888	21, 40, 58, 66, 98, 141, 151, 197, 338, 363, 502
	Low	0.48	1961	23, 28, 47, 81, 110, 133, 148, 210, 345, 371, 497
	Low	0.60	2047	51, 66, 71, 84, 106, 119, 122, 173, 399, 404, 452

Table 5-13 Relative energies (in eV) and vibration frequencies (in cm^{-1}) of the five lowest energy structures for $\text{Au}_3\text{Pd}_1\text{CO}$. Gold atoms are shown in yellow, palladium in dark blue, carbon in cyan and oxygen in red.

Chapter 6- The Electronic Structure of AuPt Clusters

6.1 Introduction

In this work thus far we have looked primarily at the energies of different clusters, along with surface and size effects. Further information can be acquired by studying the filling and energies of the different orbitals within the cluster. DFT calculations give us this information regarding the density of states (DOS). These electronic properties of nanoparticles can tell us about more about the chemical bonding within a system. For example, it has been shown that lowering the average energy of the d-electrons (called the d-band centre), with a more empty b-band resulting in stronger binding to small molecules. This is because more of the electron density from the adsorbate can be donated to the metal surface. The d-band centre can be calculated using equation 6-1 (135).

$$E_D = \frac{\int \rho E dE}{\int \rho dE} \quad 6-1$$

In this formula, ρ is the electron density and E is the energy. The d band center can be used to see how the electron density affects the ligand interaction energy. The traditional method of describing binding of CO (or any ligand) to a metal surface is through sigma-donation pi-backdonation. The electron orbitals of the C-O sigma bond donates some electron density into the metal d orbitals, while the d orbitals donate some electron density into the anti-bonding pi* orbital of the C-O

bond. This results in a carbon-metal bond and a weaker C-O bond. The strength of this bond has been shown to depend on how much electron density is in the d orbitals, also known as the d-band for more extended systems(135). Of course, nanoparticles exist in the intermediate regime between a true extended d-band and discrete orbitals over a few atoms. Where the d-band is full with fewer unoccupied d states, the d-band center shifts towards the fermi energy and results in weaker M-C binding, as the electrons donated from the carbon must occupy higher energy states. The opposite is also true; namely a less occupied d-band shifts the d-band center downwards, with more d-band unoccupied so there is a stronger metal-carbon bond.

Charges on each atom can also give further information to explain the chemical reactivity of a metal surface. However, dividing up the charge between different atoms is not a trivial exercise, and various methods exist to divide up the charge between different atoms including Löwdin(164), Mulliken(165) or Bader analysis(166). Löwdin and Mulliken methods are based on the contribution coefficients of the atomic orbitals to the molecular orbitals, but tend to be sensitive to the basis set used in the calculation(167). Bader analysis was discovered more recently, and is based on the charge density itself and not on the orbital coefficients. It works by assigning regions of electron density around charge maxima up to points of zero charge gradient (for example, in the minima between two atoms). As the charge tends to be a maximum around nuclei, this gives the charge on each atom. This method is independent of basis set, although the Bader calculations are often completed on a grid(167) which must be fine enough to give reasonable results.

6.1.1 Electron Shell Closure in Gold

It has been shown earlier that gold has interesting chemical and physical properties, but at the nanoscale it also exhibits interesting electronic properties. Au has a $[\text{Kr}] 4f^{14} 5d^{10} 6s^1$ electron shell structure. At the nanoscale, the 6s electrons can bond into jellium orbitals, whereby the electrons are distributed in the cluster which can be treated as a uniformly distributed positive charge. This results in electron shells with different 'magic shells' within a 'superatom' compared with atomic orbitals(168). In the same way that unusual stability occurs in atoms where the number electrons equals 2, 10, 18, 36 etc, for a superatom the stability occurs where the number of electrons equals 2, 8, 18, 34 and 58, with 20 and 40 electrons also stable under some conditions(21, 169). This has been found to alter the structure of gold clusters, with thiol ligands able to remove gold atoms from the cluster and create S-Au-S bridges(168, 170). These have been found both experimentally(171) and theoretically(172).

6.2 Methodology

Most of the results were performed using the quantum espresso package. An energy cutoff for the basis set was 30.0Ry (one Rydberg equals 13.606eV), and the charge cutoff was 150Ry. These calculations are performed using plane waves, which require tessellation of the unit cell. To avoid sampling the Brillouin zones of each unit cell, the calculations were performed using the gamma point. In addition, a unit cell size of 40 bohr radii. Two different basis sets were used: the PBE ultrasoft pseudo-potentials and the PW91 Vanderbilt ultrasoft pseudo-potentials. All structures were fully relaxed at the DFT level.

Charges were calculated using the Löwdin method implemented within Quantum Espresso. Mulliken charges were briefly investigated; however they overestimated the amount of electron density in the core of the cluster, with atomic charges of greater than minus two per atom in the core. This is clearly incorrect, so these results were not taken further.

Similar geometries to those used in Chapter 4- were used, with compositions of $\text{Au}_6\text{Pt}_{32}$, its inverse $\text{Pt}_6\text{Au}_{32}$ and $\text{Au}_{34}\text{Pt}_4$. Au_{34} has been found to be a chiral nanoparticle, and has a magic number of electrons exhibiting a closed electron shell. We looked at $\text{Au}_{34}\text{Pt}_4$ to see if the bimetallic nanoparticle shows the same electronic behaviour. The centroid, core and hex homotops, as used in chapter 3 were used, with the $\text{Au}_{34}\text{Pt}_4$ homotops shown in figure 6-1. Au_{34} have been found to have electron shell closure and exhibit a band gap around the fermi energy. Adding a small number of Pt atoms may destroy this gap.

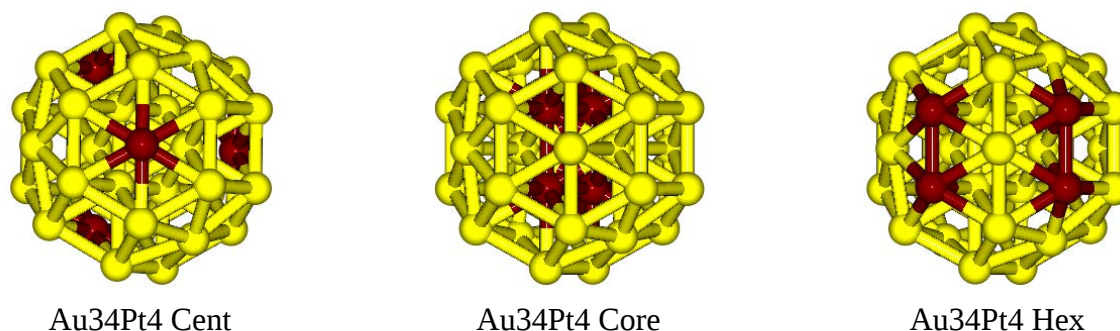


Figure 6-1 The homotops studied for the $\text{Au}_{34}\text{Pt}_4$ clusters. Platinum atoms are shown in dark red, gold in yellow. These clusters are similar to those studied in Chapter 4- .

6.3 Results

6.3.1 Bare Clusters

6.3.1.1 Energies

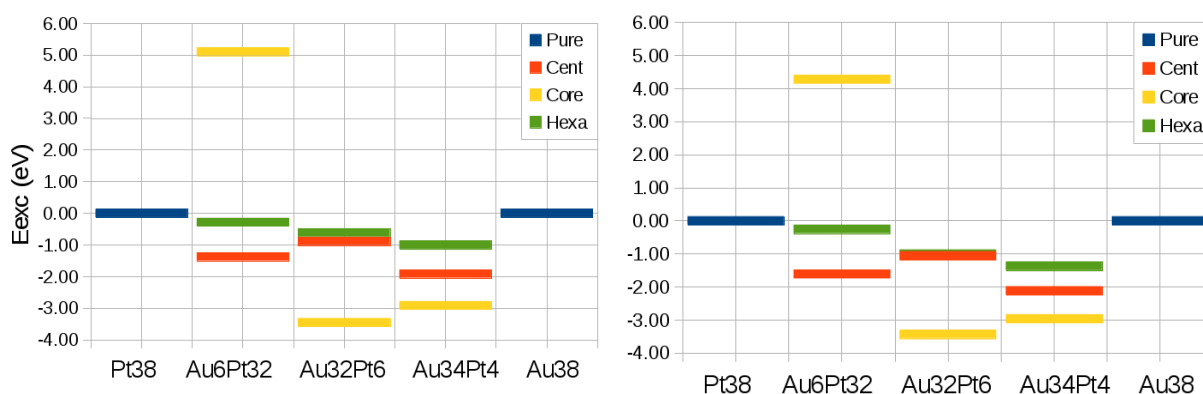


Figure 6-2 Excess energies (in eV) of the bare AuPt clusters for different compositions and homotops. Left- PBE functional, Right- PW91 functional.

The energies of the bare clusters are shown in figure 6-2. The results for the excess energies between the PBE and PW91 exchange correlation function are very similar, with identical trends and with energy changes of no larger than Pt has the higher surface energy compared with gold, so the core shell structure is preferred for both $\text{Au}_{34}\text{Pt}_4$ and $\text{Au}_{32}\text{Pt}_6$. However, unlike previous results the lowest energy structure for $\text{Au}_6\text{Pt}_{32}$ is not the hex structure but the centroid structure. Gold is larger than Pt (lattice constant for gold is 4.079 Å, compared with 3.924 Å for platinum). As a consequence; Au atoms pop out of the surface of the cluster, reducing the energy of the centroid structure so that the centroid sites are more 'vertex like'. In addition, Gold-Platinum forms well known stable alloys, stabilising the centroid structure which has the largest number of hetero-nuclear bonds for these systems studied (173).

DFT calculations of $\text{Au}_{34}\text{Pt}_4$ were completed to see if a small number of Pt atoms allowed the cluster too keep the band gap which is present in Au_{34} . All the homotops retained the band gap character, and these values are shown in Table 6-1.

Structure	PBE band gap (eV)	PW91 band gap (eV)
Cent	0.78	0.82
Core	0.83	0.81
Hex	0.60	0.64

Table 6-1 The band gaps around the fermi level for the $\text{Pt}_4\text{Au}_{34}$ clusters. These values are calculated from the energies of the Highest Occupied Molecular Orbital (HOMO) and the Lowest Unoccupied Molecular Orbital (LUMO).

The PBE and PW91 exchange correlation functional show strong agreement with each other to within 0.04eV. The hex structure has the smallest band gap which is due to the Pt atoms changing the shape of the jellium orbitals from an approximate sphere to an ellipsoid, thereby reducing the energy gap.

6.3.1.2 Charges- 38 Atom Clusters

The charges for each atom for the $\text{Au}_6\text{Pt}_{32}$ clusters are shown in figure 6-3. Atoms at the red end of the spectrum have a positive charge and have lost electron density relative to their gas phase atoms and the bluer atoms have gained electron density. Green atoms denote no gain or loss in electron density. The PBE and PW91 results disagreed with each other, with the PBE functional finding gold became negatively charged, whereas the PW91 functional found that the gold lost its electrons. Both PBE and PW91 functionals agree that the hex structure exhibits less charge transfer between the gold and the platinum compared to the centroid or the core-shell homotop. This could be because the hex structure has the few number of inhomogeneous Au-Pt bonds, results in fewer neighbours to move the charge to. In addition, the PBE functional shows stronger electron transfer.

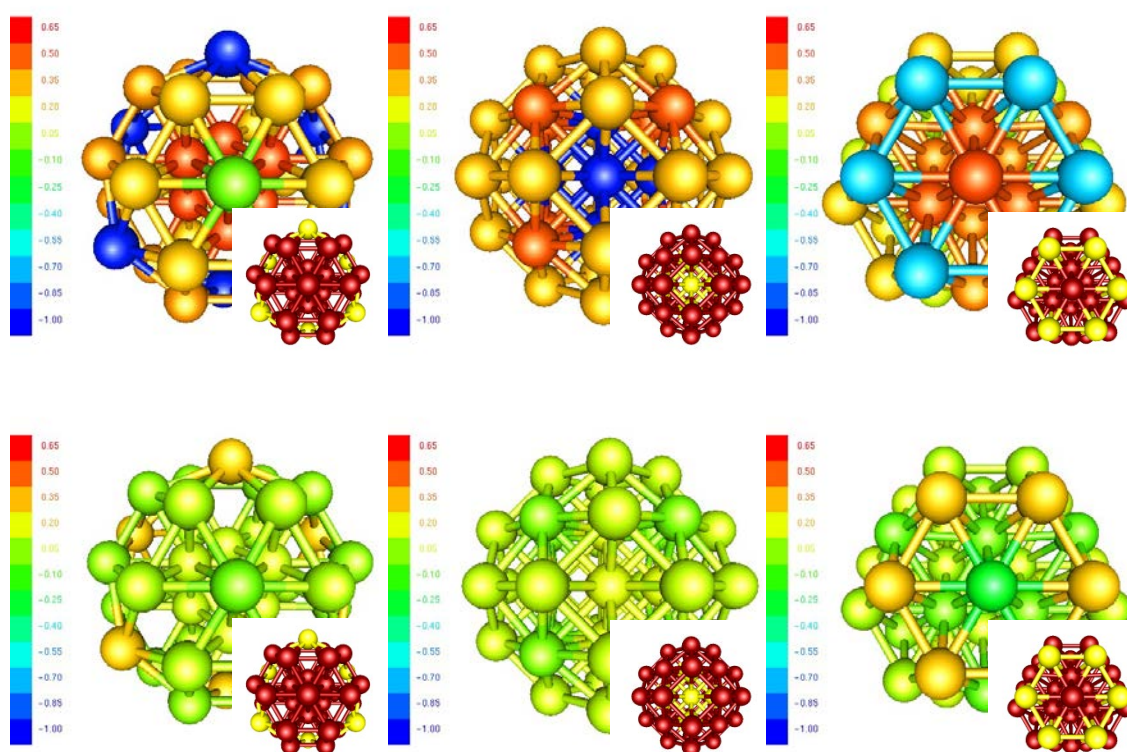


Figure 6-3 Löwdin charges on each atom relative to the gas phase atom. the orientation of each cluster is given in the bottom left of each picture, with dark red atoms for platinum and yellow for gold atoms. For the top row the PBE functional was used, and the bottom row shows the charges found using the PW91 XC functional.

This issue was investigated further, to confirm which of these conflicting results was correct. Using the $\text{Pt}_6\text{Au}_{32}$ core-shell structure as a test case, DFT calculations were completed on NWChem, using both the PBE and PW91 functional. Two different basis sets were investigated(174, 175), the def2-TZVP (def2) basis set(62), and additionally the CRENBS basis set(176). The def2 basis simulated 19 electrons for the gold and 18 for platinum, whereas the CRENBS basis set simulated 11 electrons explicitly for gold and 10 electron for platinum. In both cases the rest of the electrons were treated using an effective core potential. The results for the Löwdin charges are shown in Table 6-2 and Mulliken charges are shown in Table 6-3. In all cases, the NWChem Löwdin results agreed with the results given by the PW91 functional using Quantum Espresso.

Program	Basis set	XC	Core	Cent	Hex
NWChem	CRENBS	PBE	-0.25	0.00	0.06
NWChem	CRENBS	PW91	-0.25	0.00	0.06
NWChem	def2	PBE	-0.17	0.01	0.04
NWChem	def2	PW91	-0.17	0.01	0.04
NWChem	def2-cf	PBE	-0.37	0.01	0.09
NWChem	def2-cf	PW91	-0.37	0.02	0.09
QE	rrkjus	PBE	0.54	-0.21	-0.03
QE	van	PW91	-0.23	-0.01	0.08

Table 6-2 Löwdin charges for the three different sites on the Pt₆Au₃₂ core-shell cluster, using different programs, basis sets and exchange correlation functionals.

Program	Basis set	XC	Core	Cent	Hex
NWChem	CRENBS	PBE	0.28	0.10	-0.10
NWChem	CRENBS	PW91	0.29	0.10	-0.11
NWChem	def2	PBE	-1.43	0.16	0.30
NWChem	def2	PW91	-1.42	0.17	0.30
NWChem	def2-cf	PBE	-2.69	-0.06	0.69
NWChem	def2-cf	PW91	-2.76	-0.08	0.72

Table 6-3 Mulliken charges for the three different sites on the Pt₆Au₃₂ core-shell cluster, using different programs, basis sets and exchange correlation functionals.

With the def2 basis set, the Mulliken charges are clearly incorrect with a strong negative charge on the Pt atoms in the core. The Crenbs basis set agrees with the results from the PBE functional in NWChem.

To confirm which results are correct, these results were compared with work by Bus and van Bokhoven(177). They compared X-ray Adsorption Spectroscopy with theoretical calculations using the FEFF8 code(178) which can simulate the fine structure of X-ray absorption. They find a decreasing peak in the Pt L₃ edge from X-ray Absorption Near Edge Structure (XANES) spectra compared with pure Pt. This indicates Pt had lost electrons to the gold. This was confirmed with their results from FEFF8 calculations on 55 atom clusters. Therefore, the Quantum Espresso PBE results are incorrect, along with the CRENBS Mulliken charges. To quantify these

errors, the orbital occupations from quantum espresso were compared to orbital occupations by Bus and van Bokhoven (177).

6.3.1.3 Charges- 55 Atom Clusters

Calculations were performed using Quantum Espresso with both the PW91 and PBE functions. The clusters used were Au_{55} , Pt_{55} , Au_{54}Pt and Pt_{54}Au . The orbital occupations were then compared to Bus and van Bokhoven's work (177). The results are shown in figure 6-4.

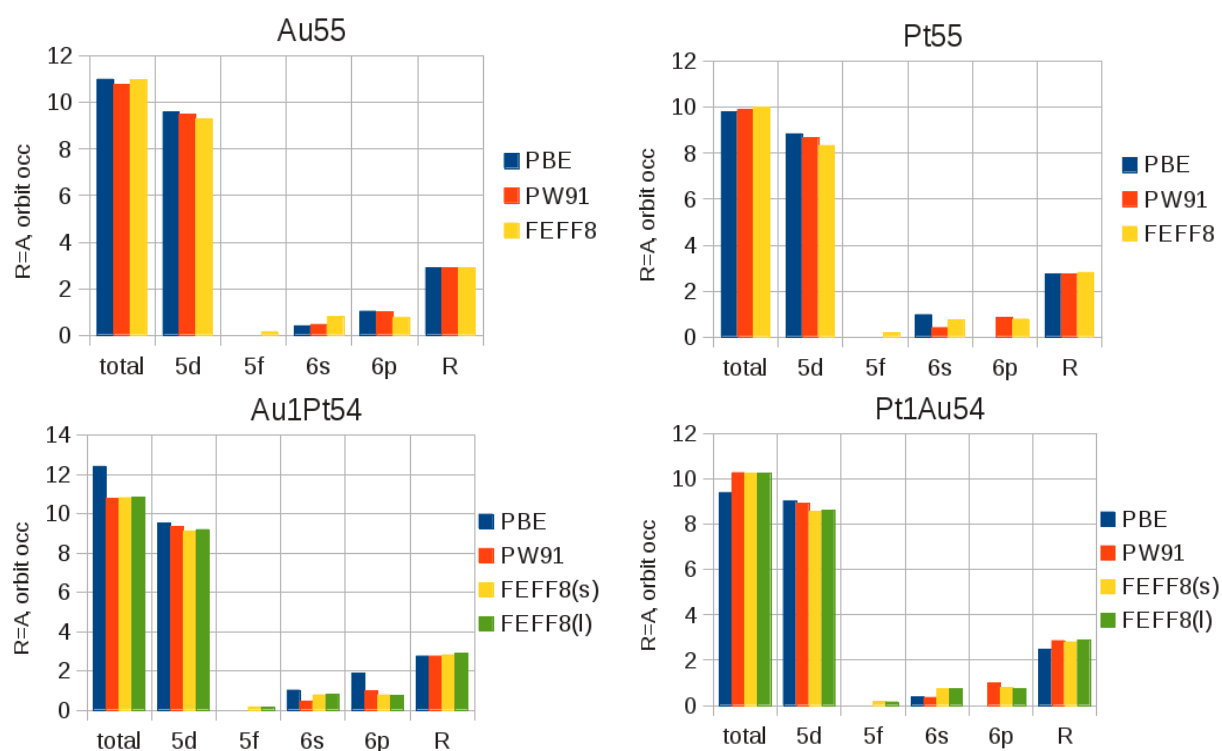


Figure 6-4 Graphs showing the bond distance R and the orbital occupations for Au_{55} , Pt_{55} , AuPt_{54} and PtAu_{54} . The FEFF8 data was taken from reference (177).

The two different FEFF8 results come from different electronic states with short (s) and long (l) bond distances; however all the bond lengths are very similar, varying only by 0.25\AA , with the exception of the PBE results which overestimates the bond length contraction for the PtAu_{54} cluster. More importantly, the PBE basis set does not model the 6p orbital for Pt, so can't accept electron density into that orbital.

The PW91 basis set does include the 6p orbital, allowing more electron density to flow to the Pd atom and hence store the negative charge. This explains the results for NWChem, as all the LCAO basis sets tested included functions for the 6p orbital. The FEF8 data also shows some electron density in the 5f orbital. This explains why the PW91 basis still has more electron density in the d orbitals, but the amount in the 5f orbitals is small (between 0.13 and 0.17 on each atom), so can safely be neglected for these calculations.

6.4 Conclusions and Future Work

The energies of bare AuPt clusters were investigated. Investigations on AuPd, RhPd and PdPt shows that normally the element with the lower binding energy prefers to occupy the vertex sites of the 38 atom TO nanoparticle. Despite this, Au centroid sites in AuPt, due to the size of the gold atoms coming out of the surface and stabilising the centroid sites.

Great care must be taken in calculating charges on AuPt systems, particularly using plane wave codes. It was found that it was necessary to include the 6p orbit to achieve the correct charge transfer of electron density from the gold to the platinum. Neglecting this resulted in the gold gaining electron density in disagreement with experimental results. This may explain some of the issues regarding the Pt(111) puzzle. If a small charge from a CO molecule can be donated into the 5f and 6p electrons in platinum, this could change the preferred bonding site for CO. The complexity of this puzzle has been found irrespective of the exchange correlation functional used. We have shown this is still the case for the bimetallic AuPt system.

In addition, it was shown that the bimetallic $\text{Au}_{34}\text{Pt}_4$ nanoparticles still form 'superatoms', with electron shell closure. This effect occurs irrespective of the homotop the cluster adopts, although the size of the band gap is affected by the position of the platinum atoms.

The electron shell closure work can be expanded in several ways. The $\text{Pt}_6\text{Au}_{32}$ clusters do not show electron shell closure, with no band gap between the HOMO and the LUMO. However, they are only two gold atoms away from achieving shell closure. Charging the cluster with two electrons should result in shell closure, and therefore enhanced stability. platinum has not been shown to exhibit the same behaviour as gold, so adding additional platinum to an Au_{34} 'subcluster', there may come a point where electron shell closure no longer occurs.

An obvious extension to this work is to see how or if the shell closure effects the binding energy of CO and other ligands to the bimetallic AuPt clusters. I predict that it would only affect the binding energy to the Pt slightly, but CO would exhibit a stronger binding energy to gold in $\text{Au}_{32}\text{Pt}_6$ than to $\text{Au}_{34}\text{Pt}_4$.

Finally, solving the Pt (111) puzzle would be very useful for future computational chemists. This could be achieved by altering the size of the core ECP by including or excluding the 4f and 5p orbitals in the core, and altering which valence orbitals are included (6p and 5f) in the calculation.

Chapter 7- Future Work

It has been shown in this thesis that calculations can help explain experimental results. In chapter three we found out how different levels of theory can complement one another, helping to validate results within a reasonable time frame. The BCGA or basin hopping alone was not sufficient to search the energy landscape thoroughly enough to find many of the low energy isomers by themselves, but using both with symmetry searches was useful to find more local minima. Further work could be done to speed up the GA, through parallelisation, to study and optimise systems closer to the sizes of nanoparticles studied experimentally. Some surprising results include the chiral $\text{Rh}_4\text{Pd}_{30}$ cluster, and the LT structure found to be the lowest energy structure for pure Rh_{98} .

Chapter 4- used a simple model to attempt to explain nanoparticle and bulk surface rearrangement, showing smaller calculations can shed light onto larger systems without spending unnecessary computer resources. It was found that energetic inversion occurred when multiple ligands were bound to the surface, and in most cases the difference in binding strength between the two metals in a bimetallic cluster was the cause. The exception was the CuPt system, where additional effects resulted in Cu coming to the surface where it would be expected to be an unfavourable site.

To expand the work on the small dimers, trimers and tetramers would be to improve validation with a higher level of theory. This could include coupled cluster

methods, or relativistic calculations with spin-orbit coupling included. In addition, mapping the energy surface, like what was achieved by Negreiros et al. (112), could be done for these clusters at a higher level of theory. Although CCSD would probably be too computationally heavy, calculating the energy surface with spin-orbit coupling is achievable with current computer hardware.

This thesis has focused on chemisorption, but the long term goal has been to model a true catalytic system(179). Ideally this would include the nanoparticle itself, interactions with the adsorbates and the surface the nanoparticle is attached to. Clearly this work is a long jump away from being able to achieve that goal, but it is a step in the correct direction. We have looked at charges on AuPt systems, finding that it is important for adequate basis sets to be used for results to have a meaningful result.

The next stage for this work is to extend toward co-adsorption of different species. If a molecule prefers binding in some form, that will prevent certain species from being formed.

Another extension would be to complete Nudged Elastic Band (NEB) calculations on nanoparticles. This can initially be achieved by finding the barriers for an adsorbate to move from one hollow site to another, before being expanded to chemical reactions.

This work has not looked at the effect of the surface upon the nanoparticle, or on how a surface affects the interaction energy between the adsorbate and the nanoparticle. It has been shown by Haruta's pioneering work the surface upon which the nanoparticle is bound to can affect the reactivity(8), so such an effect cannot be ignored indefinitely by computational chemists.

Computers are still getting more powerful, and cheaper, which will continue to allow chemists and physicist to model the world around us in more detail.

References

1. Ferrando R, Jellinek J, & Johnston RL (2008) Nanoalloys: From Theory to Applications of Alloy Clusters and Nanoparticles. *Chemical Reviews* 108(3):845–910.
2. Johnston RL (2002) *Atomic and Molecular Clusters* (Taylor & Francis) 1 Ed p 208.
3. Paz-Borbon LO, Johnston RL, Barcaro G, & Fortunelli A (2008) Structural motifs, mixing, and segregation effects in 38-atom binary clusters. *J. Chem. Phys.* 128(13):134517-134529.
4. Logsdail A, Paz B, n LO, & Johnston RL (2009) Structures and Stabilities of PlatinumGold Nanoclusters. *Journal of Computational and Theoretical Nanoscience* 6(4):857-866.
5. Pérez-Arantequi J, et al. (2001) Luster Pottery from the Thirteenth Century to the Sixteenth Century: A Nanostructured Thin Metallic Film. *Journal of the American Ceramic Society* 84(2):442-446.
6. Faraday M (1857) The Bakerian Lecture: Experimental Relations of Gold (and Other Metals) to Light. *Philosophical Transactions of the Royal Society of London* 147:145-181.
7. Feynman RP (1992) There's plenty of room at the bottom [data storage]. *Microelectromechanical Systems, Journal of* 1(1):60-66.
8. Haruta M, Kobayashi T, Sano H, & Yamada N (1987) Novel Gold Catalysts for the Oxidation of Carbon Monoxide at a Temperature far Below 0 °C. *Chemistry Letters* 16(2):405-408.
9. Lee YW, et al. (2008) Synthesis and Characterization of Flower-Shaped Porous Au–Pd Alloy Nanoparticles. *The Journal of Physical Chemistry C* 112(17):6717-6722.
10. Binns C (2001) Nanoclusters deposited on surfaces. *Surface Science Reports* 44(1–2):1-49.

11. Sattler K, Mühlbach J, & Recknagel E (1980) Generation of Metal Clusters Containing from 2 to 500 Atoms. *Physical Review Letters* 45(10):821-824.
12. Dietz TG, Duncan MA, Powers DE, & Smalley RE (1981) Laser production of supersonic metal cluster beams. *The Journal of Chemical Physics* 74(11):6511-6512.
13. Knight WD, *et al.* (1984) Electronic Shell Structure and Abundances of Sodium Clusters. *Physical Review Letters* 52(24):2141-2143.
14. Qian H, Zhu Y, & Jin R (2010) Isolation of Ubiquitous Au₄₀(SR)₂₄ Clusters from the 8 kDa Gold Clusters. *Journal of the American Chemical Society* 132(13):4583-4585.
15. Qian H, Zhu Y, & Jin R (2009) Size-Focusing Synthesis, Optical and Electrochemical Properties of Monodisperse Au₃₈(SC₂H₄Ph)₂₄ Nanoclusters. *ACS Nano* 3(11):3795-3803.
16. Li ZY, *et al.* (2008) Three-dimensional atomic-scale structure of size-selected gold nanoclusters. *Nature* 451(7174):46–48
17. Kroto HW, Heath JR, O'Brien SC, Curl RF, & Smalley RE (1985) C₆₀: Buckminsterfullerene. *Nature* 318(6042):162-163.
18. Koyasu K, Mitsui M, Nakajima A, & Kaya K (2002) Photoelectron spectroscopy of palladium-doped gold cluster anions; Au_nPd⁻ (n=1–4). *Chemical Physics Letters* 358(3–4):224-230.
19. Burkholder TR & Andrews L (1991) Reactions of boron atoms with molecular oxygen. Infrared spectra of BO, BO₂, B₂O₂, B₂O₃, and BO-2 in solid argon. *The Journal of Chemical Physics* 95(12):8697-8709.
20. Bruma A & Li ZY (2012) Three-dimensional structure of Au nanoparticles supported on amorphous silica and carbon substrates. *Journal of Physics: Conference Series* 371(1):012067.
21. de Heer WA (1993) The physics of simple metal clusters: experimental aspects and simple models. *Reviews of Modern Physics* 65(3):611-676.
22. Kurashige W, Yamaguchi M, Nobusada K, & Negishi Y (2012) Ligand-Induced Stability of Gold Nanoclusters: Thiolate versus Selenolate. *The Journal of Physical Chemistry Letters* 3(18):2649-2652.

23. Lim SI, *et al.* (2010) Synthesis of Platinum Cubes, Polypods, Cuboctahedrons, and Raspberries Assisted by Cobalt Nanocrystals. *Nano Letters* 10(3):964–973
24. Nolte P, *et al.* (2008) Shape Changes of Supported Rh Nanoparticles During Oxidation and Reduction Cycles. *Science* 321(5896):1654 –1658
25. Logsdail AJ, *et al.* (2010) Theoretical and Experimental Studies of the Optical Properties of Conjoined Gold–Palladium Nanospheres. *The Journal of Physical Chemistry C* 114(49):21247-21251.
26. Zarechnaya EY, Skorodumova NV, Simak SI, Johansson B, & Isaev EI (2008) Theoretical study of linear monoatomic nanowires, dimer and bulk of Cu, Ag, Au, Ni, Pd and Pt. *Computational Materials Science* 43(3):522-530.
27. Johnson-Matthey (2011) *Platinum 2011* (Hertfordshire) p 64.
28. de Bruijn F (2005) The current status of fuel cell technology for mobile and stationary applications. *Green Chemistry* 7(3):132-150.
29. Snelders DJM, Yan N, Gan W, Laurenczy G, & Dyson PJ (2011) Tuning the Chemoselectivity of Rh Nanoparticle Catalysts by Site-Selective Poisoning with Phosphine Ligands: The Hydrogenation of Functionalized Aromatic Compounds. *ACS Catalysis*:201-207.
30. Andersson KJ, Calle-Vallejo F, Rossmeisl J, & Chorkendorff I (2009) Adsorption-Driven Surface Segregation of the Less Reactive Alloy Component. *Journal of the American Chemical Society* 131(6):2404–2407.
31. Andersson KJ & Chorkendorff I (2010) On the stability of the CO adsorption-induced and self-organized CuPt surface alloy. *Surface Science* 604(19-20):1733-1736.
32. Young T (1804) The Bakerian Lecture: Experiments and Calculations Relative to Physical Optics. *Philosophical Transactions of the Royal Society of London* 94:1-16.
33. Phillips AC (2003) *Introduction to Quantum Mechanics* (Wiley, Manchester) 3 Ed p 266.
34. Davisson C & Germer LH (1927) Diffraction of Electrons by a Crystal of Nickel. *Physical Review* 30(6):705-740.
35. Arndt M, *et al.* (1999) Wave-particle duality of C60 molecules. *Nature* 401(6754):680-682.

36. Planck MKEL (1918) The Genesis and Present State of Development of the Quantum Theory. *Nobel Lectures, Physics* 1.
37. Schrödinger E (1933) The Fundamental Idea of Wave Mechanics. *Nobel Lectures, Physics* 1922-1941.
38. Schrödinger E (1926) Quantisierung als Eigenwertproblem. *Annalen der Physik* 386(18):109-139.
39. Heisenberg W (1927) Über den anschaulichen Inhalt der quantentheoretischen Kinematik und Mechanik. *Zeitschrift für Physik A Hadrons and Nuclei* 43(3-4):172-198.
40. Koch W, Baerends EJ, & Holthausen MC (2001) *A Chemist's Guide to Density Functional Theory* (FVA-Frankfurter Verlagsanstalt GmbH) p 300.
41. Born M & Oppenheimer R (1927) Zur Quantentheorie der Molekeln. *Annalen der Physik* 389(20):457-484.
42. Pauli W (1925) Über den Zusammenhang des Abschlusses der Elektronengruppen im Atom mit der Komplexstruktur der Spektren. *Zeitschrift für Physik A Hadrons and Nuclei* 31(1):765-783.
43. Pauli W (1947) *Exclusion principle and quantum mechanics* (Griffon, Neuchatel).
44. Kohn W (1999) Nobel Lecture: Electronic structure of matter—wave functions and density functionals. *Reviews of Modern Physics* 71(5):1253-1266.
45. Fermi E (1928) Eine statistische Methode zur Bestimmung einiger Eigenschaften des Atoms und ihre Anwendung auf die Theorie des periodischen Systems der Elemente. *Zeitschrift für Physik A Hadrons and Nuclei* 48(1):73-79.
46. Thomas LH (1927) The calculation of atomic fields. *Mathematical Proceedings of the Cambridge Philosophical Society* 23(05):542-548.
47. Teller E (1962) On the Stability of Molecules in the Thomas-Fermi Theory. *Reviews of Modern Physics* 34(4):627-631.
48. Sheldon JW (1955) Use of the Statistical Field Approximation in Molecular Physics. *Physical Review* 99(4):1291-1301.
49. Kohn W & Sham LJ (1965) Self-Consistent Equations Including Exchange and Correlation Effects. *Physical Review* 140(4A):A1133-A1138.

50. Hohenberg P & Kohn W (1964) Inhomogeneous Electron Gas. *Physical Review* 136(3B):B864-B871.
51. Slater JC (1930) Atomic Shielding Constants. *Physical Review* 36(1):57-64.
52. Boys SF (1950) Electronic Wave Functions. I. A General Method of Calculation for the Stationary States of Any Molecular System. *Proceedings of the Royal Society of London. Series A, Mathematical and Physical Sciences* 200(1063):542-554.
53. Paolo G, *et al.* (2009) QUANTUM ESPRESSO: a modular and open-source software project for quantum simulations of materials. *Journal of Physics: Condensed Matter* 21(39):395502.
54. Blöchl PE (1994) Projector augmented-wave method. *Physical Review B* 50(24):17953-17979.
55. Hamann DR, Schlüter M, & Chiang C (1979) Norm-Conserving Pseudopotentials. *Physical Review Letters* 43(20):1494-1497.
56. Vanderbilt D (1990) Soft self-consistent pseudopotentials in a generalized eigenvalue formalism. *Physical Review B* 41(11):7892-7895.
57. Baerends EJ, Ellis DE, & Ros P (1973) Self-consistent molecular Hartree—Fock—Slater calculations I. The computational procedure. *Chemical Physics* 2(1):41-51.
58. Eichkorn K, Weigend F, Treutler O, & Ahlrichs R (1997) Auxiliary basis sets for main row atoms and transition metals and their use to approximate Coulomb potentials. *Theoretical Chemistry Accounts: Theory, Computation, and Modeling (Theoretica Chimica Acta)* 97(1):119-124.
59. Eichkorn K, Treutler O, Öhm H, Häser M, & Ahlrichs R (1995) Auxiliary basis sets to approximate Coulomb potentials. *Chemical Physics Letters* 240(4):283-290.
60. Hellmann H (1935) A New Approximation Method in the Problem of Many Electrons. *The Journal of Chemical Physics* 3(1):61-61.
61. Hay PJ & Wadt WR (1985) Ab initio effective core potentials for molecular calculations. Potentials for the transition metal atoms Sc to Hg. *The Journal of Chemical Physics* 82(1):270-283.
62. Weigend F & Ahlrichs R (2005) Balanced basis sets of split valence, triple zeta valence and quadruple zeta valence quality for H to Rn: Design and

- assessment of accuracy. *Physical Chemistry Chemical Physics* 7(18):3297-3305.
63. Pickett WE (1989) Pseudopotential methods in condensed matter applications. *Computer Physics Reports* 9(3):115-197.
 64. Perdew JP, *et al.* (1992) Atoms, Molecules, Solids, and Surfaces: Applications of the Generalized Gradient Approximation for Exchange and Correlation. *Phys. Rev. B* 46:6671.
 65. Perdew JP, Burke K, & Ernzerhof M (1996) Generalized Gradient Approximation Made Simple. *Physical Review Letters* 77(18):3865-3868.
 66. Perdew JP, Burke K, & Ernzerhof M (1997) Erratum: Generalized Gradient Approximation Made Simple. *Phys. Rev. Lett.* 78:1396.
 67. Cohen AJ, Mori-Sánchez P, & Yang W (2011) Challenges for Density Functional Theory. *Chemical Reviews* 112(1):289-320.
 68. Becke AD (1993) Density-functional thermochemistry. III. The role of exact exchange. *The Journal of Chemical Physics* 98(7):5648-5652.
 69. Lee C, Yang W, & Parr RG (1988) Development of the Colle-Salvetti correlation-energy formula into a functional of the electron density. *Physical Review B* 37(2):785-789.
 70. Adamo C & Barone V (1999) Toward reliable density functional methods without adjustable parameters: The PBE0 model. *The Journal of Chemical Physics* 110(13):6158-6170.
 71. Adamo C & Barone V (1998) Exchange functionals with improved long-range behavior and adiabatic connection methods without adjustable parameters: The mPW and mPW1PW models. *The Journal of Chemical Physics* 108(2):664-675.
 72. Xu X & Goddard WA (2004) The X3LYP extended density functional for accurate descriptions of nonbond interactions, spin states, and thermochemical properties. *Proceedings of the National Academy of Sciences of the United States of America* 101(9):2673-2677.
 73. Cramer CJ & Truhlar DG (2009) Density functional theory for transition metals and transition metal chemistry. *Physical Chemistry Chemical Physics* 11(46):10757.

74. Pyykko P & Desclaux JP (1979) Relativity and the periodic system of elements. *Accounts of Chemical Research* 12(8):276-281.
75. van Lenthe E, Baerends EJ, & Snijders JG (1993) Relativistic regular two-component Hamiltonians. *The Journal of Chemical Physics* 99(6):4597-4610.
76. Ch C, Pelissier M, & Ph D (1986) Regular Two-Component Pauli-Like Effective Hamiltonians in Dirac Theory. *Physica Scripta* 34(5):394.
77. van Lenthe E, Baerends EJ, & Snijders JG (1994) Relativistic total energy using regular approximations. *The Journal of Chemical Physics* 101(11):9783-9792.
78. Philipsen PHT, van Lenthe E, Snijders JG, & Baerends EJ (1997) Relativistic calculations on the adsorption of CO on the (111) surfaces of Ni, Pd, and Pt within the zeroth-order regular approximation. *Physical Review B* 56(20):13556-13562.
79. Frisch MJ, *et al.* (2009) Gaussian 09 (Wallingford, CT), 09, Revision A.1.
80. Kresse G & Hafner J (1993) Ab initio molecular dynamics for liquid metals. *Phys. Rev. B* 47:558.
81. Kresse G & Hafner J (1994) Ab initio molecular-dynamics simulation of the liquid-metal-amorphous-semiconductor transition in germanium. *Phys. Rev. B* 49:14251.
82. Kresse G & Furthmüller J (1996) Efficient iterative schemes for ab initio total-energy calculations using a plane-wave basis set. *Phys. Rev. B* 54:11169.
83. Mortensen JJ, Hansen LB, & Jacobsen KW (2005) Real-space grid implementation of the projector augmented wave method. *Physical Review B* 71(3):035109.
84. Clark SJ, *et al.* (2005) First principles methods using CASTEP. *Zeitschrift für Kristallographie* 220(5-6-2005):567-570.
85. Valiev M, *et al.* (2010) NWChem: A comprehensive and scalable open-source solution for large scale molecular simulations. *Computer Physics Communications* 181(9):1477-1489.
86. Nieplocha J, *et al.* (2006) Advances, Applications and Performance of the Global Arrays Shared Memory Programming Toolkit. *International Journal of High Performance Computing Applications* 20(2):203-231.

87. Pittaway F, *et al.* (2009) Theoretical Studies of Palladium-Gold Nanoclusters: Pd-Au Clusters with up to 50 Atoms. *The Journal of Physical Chemistry C* 113(21):9141–9152.
88. Paz-Borbon LO, Johnston RL, Barcaro G, & Fortunelli A (2009) Chemisorption of CO and H on Pd, Pt and Au nanoclusters: a DFT approach. *The European Physical Journal D* 52(1-3):4.
89. Paz-Borbon LO, Gupta A, & Johnston RL (2008) Dependence of the structures and chemical ordering of Pd-Pt nanoalloys on potential parameters. *Journal of Materials Chemistry* 18(35):4154-4164.
90. Barcaro G, Fortunelli A, Polak M, & Rubinovich L (2011) Patchy Multishell Segregation in Pd-Pt Alloy Nanoparticles. *Nano Letters* 11(4):1766–1769.
91. Vermisoglou EC, Romanos GE, Karanikolos GN, & Kanellopoulos NK (2011) Catalytic NO_x removal by single-wall carbon nanotube-supported Rh nanoparticles. *Journal of Hazardous Materials* 194(0):144-155.
92. Endou A, Yamauchi R, Kubo M, Stirling A, & Miyamoto A (1997) Adsorption of NO on rhodium and palladium clusters: a density functional study. *Applied Surface Science* 119(3–4):318-320.
93. Mainardi DS & Balbuena PB (2003) Hydrogen and Oxygen Adsorption on Rh_n (n = 1–6) Clusters. *The Journal of Physical Chemistry A* 107(48):10370-10380.
94. Quek X-Y, Guan Y, & Hensen EJM (2012) Structure sensitivity in the hydrogenation of unsaturated hydrocarbons over Rh nanoparticles. *Catalysis Today* 183(1):72-78.
95. Yoon B & Wai CM (2005) Microemulsion-Templated Synthesis of Carbon Nanotube-Supported Pd and Rh Nanoparticles for Catalytic Applications. *Journal of the American Chemical Society* 127(49):17174-17175.
96. Zhang Y, Grass ME, Huang W, & Somorjai GA (2010) Seedless Polyol Synthesis and CO Oxidation Activity of Monodisperse (111)- and (100)-Oriented Rhodium Nanocrystals in Sub-10 nm Sizes†. *Langmuir* 26(21):16463-16468.
97. Hoefelmeyer JD, Niesz K, Somorjai GA, & Tilley TD (2005) Radial Anisotropic Growth of Rhodium Nanoparticles. *Nano Letters* 5(3):435-438.

98. Zhang Y, *et al.* (2007) One-step Polyol Synthesis and Langmuir–Blodgett Monolayer Formation of Size-tunable Monodisperse Rhodium Nanocrystals with Catalytically Active (111) Surface Structures. *The Journal of Physical Chemistry C* 111(33):12243-12253.
99. Tanaka H, *et al.* (2004) Design of the intelligent catalyst for Japan ULEV standard. *Topics in Catalysis* 30-31(1):389-396.
100. Tanaka H, *et al.* (2006) The intelligent catalyst having the self-regenerative function of Pd, Rh and Pt for automotive emissions control. *Catalysis Today* 117(1–3):321-328.
101. Sadeghmoghaddam E, Gaïeb K, & Shon Y-S (2011) Catalytic isomerization of allyl alcohols to carbonyl compounds using poisoned Pd nanoparticles. *Applied Catalysis A: General* 405(1–2):137-141.
102. Adams BD, Ostrom CK, Chen S, & Chen A (2010) High-Performance Pd-Based Hydrogen Spillover Catalysts for Hydrogen Storage. *The Journal of Physical Chemistry C* 114(46):19875-19882.
103. Renzas JR, *et al.* (2011) Rh₁-xPd_x nanoparticle composition dependence in CO oxidation by oxygen: catalytic activity enhancement in bimetallic systems. *Physical Chemistry Chemical Physics* 13(7):2556-2562.
104. Tao F, *et al.* (2010) Evolution of Structure and Chemistry of Bimetallic Nanoparticle Catalysts under Reaction Conditions. *Journal of the American Chemical Society* 132(25):8697-8703.
105. Tao F, *et al.* (2008) Reaction-Driven Restructuring of Rh-Pd and Pt-Pd Core-Shell Nanoparticles. *Science* 322(5903):932 –934.
106. Grass ME, *et al.* (2010) Effect of O₂, CO, and NO on Surface Segregation in a Rh_{0.5}Pd_{0.5} Bulk Crystal and Comparison to Rh_{0.5}Pd_{0.5} Nanoparticles. *Langmuir* 26(21):16362–16367.
107. Soldano G, Schulz EN, Salinas DR, Santos E, & Schmickler W (2011) Hydrogen electrocatalysis on overlayers of rhodium over gold and palladium substrates-more active than platinum? *Physical Chemistry Chemical Physics* 13(36):16437-16443.
108. Chung Y-M & Rhee H-K (2003) Partial hydrogenation of 1,3-cyclooctadiene using dendrimer-encapsulated Pd–Rh bimetallic nanoparticles. *Journal of Molecular Catalysis A: Chemical* 206(1–2):291-298.

109. Bai Z, *et al.* (2010) Solvothermal synthesis and characterization of Pd–Rh alloy hollow nanosphere catalysts for formic acid oxidation. *Catalysis Communications* 11(10):919-922.
110. Wales DJ & Scheraga HA (1999) Global Optimization of Clusters, Crystals, and Biomolecules. *Science* 285(5432):1368-1372.
111. Wu ZJ, Zhou SH, Shi JS, & Zhang SY (2003) Geometries and electronic properties of AunPdm ($n=1-4$, $m=-1, 0, 1$) clusters. *Chemical Physics Letters* 368(1-2):153-161.
112. Negreiros FR, *et al.* (2012) A first-principles theoretical approach to heterogeneous nanocatalysis. *Nanoscale*.
113. Heiles S, Logsdail AJ, Schafer R, & Johnston RL (2012) Dopant-induced 2D-3D transition in small Au-containing clusters: DFT-global optimisation of 8-atom Au-Ag nanoalloys. *Nanoscale*.
114. de Bas BS, Ford MJ, & Cortie MB (2004) Low energy structures of gold nanoclusters in the size range 3–38 atoms. *Journal of Molecular Structure: THEOCHEM* 686(1-3):193-205.
115. Cleri F & Rosato V (1993) Tight-binding potentials for transition metals and alloys. *Physical Review B* 48(1):22-33.
116. Ismail R & Johnston RL (2010) Investigation of the structures and chemical ordering of small Pd-Au clusters as a function of composition and potential parameterisation. *Physical Chemistry Chemical Physics* 12(30):8607-8619.
117. Paz-Borbón LO (2009) Computational Studies of Transition Metal Nanoalloys. Doctor of Philosophy (University of Birmingham, Birmingham).
118. Paz-Borbón LO, Johnston RL, Barcaro G, & Fortunelli A (2007) A Mixed Structural Motif in 34-Atom Pd–Pt Clusters. *The Journal of Physical Chemistry C* 111(7):2936-2941.
119. Denton AR & Ashcroft NW (1991) Vegard's law. *Physical Review A* 43(6):3161-3164.
120. Johnston RL (2003) Evolving better nanoparticles: Genetic algorithms for optimising cluster geometries. *Dalton Transactions* (22):4193-4207.
121. Darwin C (1859) *On the Origin of Species by Means of Natural Selection, or the Preservation of Favoured Races in the Struggle for Life* (John Murray) p 502.

122. Oakley MT, Wales DJ, & Johnston RL (2011) Energy Landscape and Global Optimization for a Frustrated Model Protein. *The Journal of Physical Chemistry B* 115(39):11525-11529.
123. Leary RH & Doye JPK (1999) Tetrahedral global minimum for the 98-atom Lennard-Jones cluster. *Physical Review E* 60(6):R6320-R6322.
124. Rappe AM, Rabe KM, Kaxiras E, & Joannopoulos JD (1990) Optimized pseudopotentials. *Physical Review B* 41(2):1227-1230.
125. Rappe AM, Rabe KM, Kaxiras E, & Joannopoulos JD (1991) Erratum: Optimized pseudopotentials. *Physical Review B* 44(23):13175-13176.
126. Lechtken A, *et al.* (2007) Au₃₄–: A Chiral Gold Cluster? *Angewandte Chemie International Edition* 46(16):2944-2948.
127. Kittel C (1966) *Introduction to solid state physics* (Wiley, New York).
128. Núñez S & Johnston RL (2010) Structures and Chemical Ordering of Small Cu–Ag Clusters. *The Journal of Physical Chemistry C* 114(31):13255-13266.
129. Feibelman PJ, *et al.* (2000) The CO/Pt(111) Puzzle†. *The Journal of Physical Chemistry B* 105(18):4018-4025.
130. Olsen RA, Philipson PHT, & Baerends EJ (2003) CO on Pt(111): A puzzle revisited. *The Journal of Chemical Physics* 119(8):4522-4528.
131. Bertin V, Agacino E, López-Rendon R, & Poulain E (2006) The CO chemisorption on some active sites of Pd clusters: A DFT study. *Journal of Molecular Structure: THEOCHEM* 769(1–3):243-248.
132. Yuan D, Gong X, & Wu R (2008) Peculiar distribution of Pd on Au nanoclusters: First-principles studies. *Physical Review B* 78(3):035441.
133. Wei T, Wang J, & Goodman DW (2007) Characterization and Chemical Properties of Pd–Au Alloy Surfaces. *The Journal of Physical Chemistry C* 111(25):8781-8788.
134. Knudsen J, *et al.* (2007) A Cu/Pt Near-Surface Alloy for Water-Gas Shift Catalysis. *Journal of the American Chemical Society* 129(20):6485–6490
135. Jennings PC, Pollet BG, & Johnston RL (2012) Electronic Properties of Pt–Ti Nanoalloys and the Effect on Reactivity for Use in PEMFCs. *The Journal of Physical Chemistry C* 116(29):15241-15250.

136. Wesendrup R, Hunt T, & Schwerdtfeger P (2000) Relativistic coupled cluster calculations for neutral and singly charged Au[sub 3] clusters. *The Journal of Chemical Physics* 112(21):9356-9362.
137. Schultz NE, Gherman BF, Cramer CJ, & Truhlar DG (2006) PdnCO (n = 1,2): Accurate Ab Initio Bond Energies, Geometries, and Dipole Moments and the Applicability of Density Functional Theory for Fuel Cell Modeling. *The Journal of Physical Chemistry B* 110(47):24030–24046.
138. Filatov M (2003) On the binding of carbonyl to a single palladium atom. *Chemical Physics Letters* 373(1–2):131-135.
139. Häkkinen H & Landman U (2000) Gold clusters (AuN, 2<N<10) and their anions. *Physical Review B* 62(4):R2287-R2290.
140. Suzer S & Andrews L (1988) Matrix isolation study of electron impact on H₂O. Infrared spectrum of OH⁻ in solid argon. *The Journal of Chemical Physics* 88(2):916-921.
141. Jiang L & Xu Q (2005) Reactions of Gold Atoms and Small Clusters with CO: Infrared Spectroscopic and Theoretical Characterization of AunCO (n = 1–5) and Aun(CO)₂ (n = 1, 2) in Solid Argon. *The Journal of Physical Chemistry A* 109(6):1026-1032.
142. Gao F, Wang Y, & Goodman DW (2009) CO Oxidation over AuPd(100) from Ultrahigh Vacuum to Near-Atmospheric Pressures: CO Adsorption-Induced Surface Segregation and Reaction Kinetics. *The Journal of Physical Chemistry C* 113(33):14993–15000
143. Turra M, Waldschmidt B, Kaiser B, & Schafer R (2008) An improved time-of-flight method for cluster deposition and ion-scattering experiments. *Review of Scientific Instruments* 79(1):013905.
144. Issendorff Bv & Palmer RE (1999) A new high transmission infinite range mass selector for cluster and nanoparticle beams. *Review of Scientific Instruments* 70(12):4497-4501.
145. Pyykkö P (2008) Theoretical chemistry of gold. III. *Chemical Society Reviews* 37(9):1967.
146. Pyykkö P (2005) Theoretical chemistry of gold. II. *Inorganica Chimica Acta* 358(14):4113-4130.

147. Pyykkö P (2004) Theoretical Chemistry of Gold. *Angewandte Chemie International Edition* 43(34):4412-4456.
148. Olson RM & Gordon MS (2007) Isomers of Au₈. *The Journal of Chemical Physics* 126(21):214310.
149. Fa W, Luo C, & Dong J (2005) Bulk fragment and tubelike structures of Au_N (N=2-26). *Physical Review B* 72(20):205428.
150. Guo R, Balasubramanian K, Wang X, & Andrews L (2002) Infrared vibronic absorption spectrum and spin-orbit calculations of the upper spin-orbit component of the Au₃ ground state. *The Journal of Chemical Physics* 117(4):1614-1620.
151. Shim I & Gingerich KA (1984) Electronic structure and bonding in the Pd₂ molecule by all electron ab initio HF-Cl calculations and mass spectrometric measurements. *The Journal of Chemical Physics* 80(10):5107-5119.
152. Ho J, Ervin KM, Polak ML, Gilles MK, & Lineberger WC (1991) A study of the electronic structures of Pd₂ and Pd₂ by photoelectron spectroscopy. *The Journal of Chemical Physics* 95(7):4845-4853.
153. Dai D & Balasubramanian K (1995) Electronic structures of Pd₄ and Pt₄. *The Journal of Chemical Physics* 103(2):648-655.
154. Jian-Jun G, Ji-Xian Y, & Dong D (2005) Ab initio study of small Au_nPd₂ (n) clusters. *Physica B: Condensed Matter* 367(1-4):158-164.
155. Paier J, Marsman M, & Kresse G (2007) Why does the B3LYP hybrid functional fail for metals? *The Journal of Chemical Physics* 127(2):024103-024110.
156. Schafer A, Huber C, & Ahlrichs R (1994) Fully optimized contracted Gaussian basis sets of triple zeta valence quality for atoms Li to Kr. *The Journal of Chemical Physics* 100(8):5829-5835.
157. Weigend F, Häser M, Patzelt H, & Ahlrichs R (1998) RI-MP2: optimized auxiliary basis sets and demonstration of efficiency. *Chemical Physics Letters* 294(1-3):143-152.
158. Jules JL & Lombardi JR (2003) Transition Metal Dimer Internuclear Distances from Measured Force Constants. *The Journal of Physical Chemistry A* 107(9):1268-1273.

159. Figgen D, Peterson KA, & Stoll H (2008) Energy-consistent relativistic pseudopotentials for the 4d elements: Atomic and molecular applications. *The Journal of Chemical Physics* 128(3):034110.
160. Falsig H, *et al.* (2008) Inside Cover: Trends in the Catalytic CO Oxidation Activity of Nanoparticles (Angew. Chem. Int. Ed. 26/2008). *Angewandte Chemie International Edition* 47(26):4762-4762.
161. Peng S-L, Gan L-Y, Tian R-Y, & Zhao Y-J (2011) Theoretical study of CO adsorption and oxidation on the gold–palladium bimetal clusters. *Computational and Theoretical Chemistry* 977(1–3):62-68.
162. Heiles S, Hofmann K, Johnston RL, & Schäfer R (2012) Nine-Atom Tin-Bismuth Clusters: Mimicking Excess Electrons by Element Substitution. *ChemPlusChem* 77(7):532-535.
163. Heiles S, Johnston RL, & Schäfer R (2012) Bismuth-Doped Tin Clusters: Experimental and Theoretical Studies of Neutral Zintl Analogues. *The Journal of Physical Chemistry A* 116(29):7756-7764.
164. Lowdin P-O (1950) On the Non-Orthogonality Problem Connected with the Use of Atomic Wave Functions in the Theory of Molecules and Crystals. *The Journal of Chemical Physics* 18(3):365-375.
165. Mulliken RS (1955) Electronic Population Analysis on LCAO[Single Bond]MO Molecular Wave Functions. I. *The Journal of Chemical Physics* 23(10):1833-1840.
166. Bader RFW (1994) *Atoms in Molecules: A Quantum Theory* (Oxford University Press, USA) p 458.
167. Henkelman G, Arnaldsson A, & Jónsson H (2006) A fast and robust algorithm for Bader decomposition of charge density. *Computational Materials Science* 36(3):354-360.
168. Walter M, *et al.* (2008) A unified view of ligand-protected gold clusters as superatom complexes. *Proceedings of the National Academy of Sciences* 105(27):9157-9162.
169. Hakkinen H (2008) Atomic and electronic structure of gold clusters: understanding flakes, cages and superatoms from simple concepts. *Chemical Society Reviews* 37(9):1847-1859.

170. Häkkinen H, Walter M, & Grönbeck H (2006) Divide and Protect: Capping Gold Nanoclusters with Molecular Gold–Thiolate Rings. *The Journal of Physical Chemistry B* 110(20):9927-9931.
171. Heaven MW, Dass A, White PS, Holt KM, & Murray RW (2008) Crystal Structure of the Gold Nanoparticle $[N(C_8H_{17})_4][Au_{25}(SCH_2CH_2Ph)_{18}]$. *Journal of the American Chemical Society* 130(12):3754-3755.
172. Akola J, Walter M, Whetten RL, Häkkinen H, & Grönbeck H (2008) On the Structure of Thiolate-Protected Au_{25} . *Journal of the American Chemical Society* 130(12):3756-3757.
173. Grolier V & Schmid-Fetzer R (2008) Experimental Study of Au-Pt-Sn Phase Equilibria and Thermodynamic Assessment of the Au-Pt and Au-Pt-Sn Systems. *Journal of Electronic Materials* 37(3):264-278.
174. Feller D (1996) The role of databases in support of computational chemistry calculations. *Journal of Computational Chemistry* 17(13):1571-1586.
175. Schuchardt KL, *et al.* (2007) Basis Set Exchange: A Community Database for Computational Sciences. *Journal of Chemical Information and Modeling* 47(3):1045-1052.
176. Ross RB, *et al.* (1990) Ab initio relativistic effective potentials with spin--orbit operators. IV. Cs through Rn. *The Journal of Chemical Physics* 93(9):6654-6670.
177. Bus E & van Bokhoven JA (2007) Hydrogen chemisorption on supported platinum, gold, and platinum?gold-alloy catalysts. *Physical Chemistry Chemical Physics* 9(22):2894.
178. Zabinsky SI, Rehr JJ, Ankudinov A, Albers RC, & Eller MJ (1995) Multiple-scattering calculations of x-ray-absorption spectra. *Physical Review B* 52(4):2995-3009.
179. Paz-Borbón LO (2011) *Computational Studies of Transition Metal Nanoalloys* (Springer).